TREATMENT OF CONVECTION IN SEQUENTIAL SOLVERS FOR NAVIER–STOKES EQUATIONS

By

SIDDHARTH SINGH THAKUR

A DISSERTATION PRESENTED TO THE GRADUATE SCHOOL
OF THE UNIVERSITY OF FLORIDA IN PARTIAL FULFILLMENT
OF THE REQUIREMENTS FOR THE DEGREE OF
DOCTOR OF PHILOSOPHY

UNIVERSITY OF FLORIDA

1993

ACKNOWLEDGEMENTS

I can only begin to express my sincere gratitude towards Professor Wei Shyy for his constant support, enthusiastic guidance and help, both academically and personally. The lofty standards he has set, both at the professional and personal levels, have always inspired me. I will never forget his gracious tolerance of my ignorance and patient discourse of knowledge, without any sense of encumbrance; I will forever remain indebted for his contribution in shaping of my overall academic career. The genuine consideration and understanding that he shows towards students in general and international students in particular have often been a source of comfort to me during times of despair. I also thank him for the financial support that he has been responsible for during my graduate studies.

Mere words cannot express my appreciation for my wife, Jyoti, who has provided love and support in more ways than she will ever know; her mere presence took the rigor and the monotony out of my work and helped me stay focussed on my objectives, in both my academic pursuits and life in general. I am deeply indebted to my family, especially my mother, Swarajya Thakur, my father, Vijendra Singh Thakur, and my sister, Nikita, for their unwavering love and encouragement and selfless support throughout my life. I have also been fortunate to have had Jeff Wright (Ramu) and H.S. Udaykumar (Dadhi) as great friends and office mates to share the good and the bad times.

I would like to express my gratitude towards my committee members– –Professors Richard Fearn, Chen–Chi Hsu, David Mikolaitis and William Hager, especially Dr. Fearn with whom I started my research career. Thanks are also due to Dr. Renwei Mei for several helpful discussions and Madhukar Rao for his advice related to computer matters. Finally, I must acknowledge the financial support received from the Department of Aerospace Engineering, Mechanics and Engineering Science at the University of Florida and NASA grant NAG8–177,

TABLE OF CONTENTS

page

ACKNOWLEDGEMENTS ii

ABSTRACT vi

CHAPTERS

I INTRODUCTION 1

II UNIFIED FORMULATION OF SOME CONVENTIONAL SCHEMES 9

2.1 Background 9
2.2 Formulation of the Convection Schemes 12
2.2.1 First–Order Upwind Scheme 14
2.2.2 Central Difference Scheme 16
2.2.3 Second–Order Upwind Scheme 17
2.2.3.1 Non–conservative formulation: Scheme A 17
2.2.3.2 Conservative formulation: Scheme B 19
2.2.4 QUICK Scheme 24
2.3 Boundary Treatments: u–control volumes 28
2.3.1 Left Border Control Volumes 29
2.3.2 Bottom Border Control Volumes 34
2.3.3 Summary of the Boundary Treatments 38
2.4 Results of the Test Case 39
2.4.1 Overall Accuracy 40
2.4.1.1 Assessment of central difference scheme and the two second–order upwind schemes 40
2.4.1.2 Comparison of various schemes on the 21x21 grid 49
2.4.2 Stability and Convergence 52

2.4.3 Effects of Various Boundary Treatments 54
2.5 Concluding Remarks 57

III CONCEPTS OF TVD SCHEMES AND EXTENSION TO SEQUENTIAL SOLVERS 60

3.1 Background 60
3.2 Basic Theory of TVD schemes 64
3.2.1 Harten's TVD Scheme for Scalar Conservation Laws 66
3.2.2 Artificial Compression 69
3.2.3 Application of the TVD Scheme to Systems of Conservation Laws 71
3.3 Application to Euler Equations for the Shock Tube Problem 73
3.3.1 Euler Equations as a Simultaneous System 75
3.3.2 Euler Equations as a Sequential System 80
Approach A: naive extension of the TVD scheme for scalar conservation laws 80
Approach B: coordinated characteristics 83
Approach C: coordinated characteristics with special source term treatment 86
3.3.3 Effect of Numerical Dissipation on the Shock Tube Problem 98
3.4 Unsteady Flow in a Shock Tube with Reflecting Boundaries 102
3.5 The Resonant Pipe Problem 107
3.6 Concluding Remarks 111

IV TREATMENT OF SOURCE TERMS: A LONGITUDINAL COMBUSTION INSTABILITY PROBLEM 114

4.1 Background 114
4.2 Basic Equations for the Combustion Instability Problem 117
4.3 Numerical Scheme and the Treatment of Source Terms 118
4.4 Application of Active Control 119
4.5 Results 120
4.5.1 Simulation of Combustion Instability 120
4.5.2 Active Control of Combustion Instability 129
4.6 Concluding Remarks 135

V A CONTROLLED VARIATION SCHEME FOR MULIT–DIMENSIONAL RECIRCULATING FLOWS 136

5.1 Background 136
5.2 Harten's Implicit Second–Order TVD Scheme 139
5.3 Linearized Versions of the Implicit TVD Scheme 141
5.3.1 Linearized Non–Conservative Implicit (LNI) Form 142
5.3.2 Linearized Conservative Implicit (LCI) Form 143
5.4 Model Problem I: Linear Convection–Diffusion Equation 144
5.4.1 Implementation of the CVS for the Model Problem 146
5.4.2 Results for Model Problem I 149
5.4.3 Effective Cell Peclet Number 153
5.5 Model Problem II: Linear Burgers' Equation with Source 156
5.6 Incompressible, Laminar Navier–Stokes Equations 161
5.6.1 Linearized Form of the CVS for the SIMPLE Algorithm 163
5.6.2 Effective Cell Peclet Number 164
5.6.3 Boundary Treatment 165
5.7 Results of Two–Dimensional Incompressible Flows 167
5.7.1 Driven Cavity Flow 168
5.7.2 Flow Over a Backward–Facing Step 176
5.8 Concluding Remarks 181

VI TURBULENT FLOW COMPUTATIONS 183

6.1 Background 183
6.2 Basic Equations 185
6.2.1 Equations of Mean Flow 185
6.2.2 k–ε Equations 187
6.2.3 Boundary Conditions and Wall Treatment 188
6.3 Computation of Turbulent Flow Over a Backward–Facing Step 193
6.4 Concluding Remarks 201

VII SUMMARY AND SUGGESTIONS FOR FUTURE WORK 204

REFERENCES 207

BIOGRAPHICAL SKETCH 217

Abstract of Dissertation Presented to the Graduate School
of the University of Florida in Partial Fulfillment of the
Requirements for the Degree of Doctor of Philosophy

TREATMENT OF CONVECTION IN SEQUENTIAL SOLVERS FOR
NAVIER–STOKES EQUATIONS

By

Siddharth Singh Thakur

August 1993

Chairperson : Wei Shyy
Major Department : Aerospace Engineering, Mechanics and Engineering Science

Several key issues regarding the numerical treatments of convection and source terms occurring in the Navier–Stokes equations, within the framework of pressure–based sequential solution algorithms, are explored. As for the convection terms, two approaches are investigated. The first involves the estimation of fluxes at the control volume interfaces using different geometric shape functions, whereas the second approach involves the introduction of an appropriate amount of nonlinear dissipation into the central difference scheme. The former approach is employed to study the convection schemes such as the first–order upwind, the central difference, the second–order upwind and the Quadratic Upstream Interpolation for Convective Kinematics (QUICK) schemes; conservative, consistent and stable formulations of these schemes are devised in a unified framework. It is demonstrated that conservative formulations of the higher–order upwind schemes are necessary, along with consistent boundary treatments, in order to achieve accuracy and to employ them as effective substitutes for the more conventional first–order upwind and central difference schemes. The second approach utilizes the formalism of the Total Variation Diminishing (TVD) schemes; it is shown that with an appropriate framework, the

TVD schemes (hitherto implemented only in simultaneous solvers) can be extended to sequential solvers to yield high resolution of sharp gradients in the flowfield. One–dimensional test cases such as the system of Euler equations for flows in a shock tube and the so–called resonant pipe as well as the linear Burgers' equation with and without a source term are investigated. A controlled variation scheme (CVS) based on the above notion is developed for a multidimensional pressure–based sequential algorithm and its efficacy demonstrated for laminar and turbulent recirculating flows. Recirculating flows in a driven cavity and past a backward–facing step are used as two–dimensional test cases. It is demonstrated how the CVS operates by reducing the magnitude of effective cell Peclet numbers compared to the central central difference scheme in regions of sharp flow gradients.

As for the treatment of source terms in Navier–Stokes equations, it is shown that sequential solvers with special techniques for treating source terms, such as MacCormack's predictor–corrector and Strang's operator–splitting methods, can yield satisfactory performance in the presence of stiff source terms; this is demonstrated by investigating a one–dimensional longitudinal combustion instability problem which possesses strong heat release source terms.

CHAPTER 1
INTRODUCTION

Over the past few decades, computational fluid dynamics (CFD) has developed into an effective tool for application to a wide variety of fluid dynamics problems, hitherto deemed unfathomable except via experimentation. Though the field of CFD is still evolving, big strides have already been made in diverse areas ranging from accurate and robust numerical approximations to the Navier–Stokes equations and efficient solution techniques to the ability of computing flows in complex geometries. With the tremendous progress made in both software and hardware aspects, computer technologies are now becoming integrated into the design process in a truly useful way. Computational fluid dynamics is increasingly becoming a part of many designers' toolkits. It has made a qualitative impact on both cost and performance in the design of many aerospace products, most notably in the airframe industry, but also progressively in the propulsion industry. There are several advantages to an accurate and efficient numerical simulation of a complex practical fluid flow problem that does not lend itself to any analytical treatment. For example, one can save time and the expenditure invested in experimentation, either by totally relying on a CFD simulation of the problem under study, or by conducting experiments for only a few selected parameters based on information obtained numerically. It is much easier to study the effects of variation of flow parameters (such as Mach number), geometry of the domain, boundary conditions, etc., on the fluid flow in a numerical simulation than in an experiment (where it may be impractical or even impossible to vary certain parameters or conditions).

The multitude of researchers in the field of CFD have employed a wide variety of numerical techniques which can be broadly categorized as finite difference, finite volume,

finite element, boundary element and spectral methods– –each possessing its own relative merits over the others. In the present work, we adopt the finite volume method for solving the full Navier–Stokes equations. In this category, two major computational approaches have found wide use in the CFD community, namely, pressure–based methods and density–based methods. For these methods, the velocity field is normally specified using the momentum equations. The density–based methods use the continuity equation to specify the density and extract pressure information using the equation of state. The system of equations is usually solved in a simultaneous manner. These methods can be extended with some modification to low Mach number regimes where the flows are incompressible and hence density has no role to play in determining the pressure field (Merkle & Choi 1987, Hirsch 1990, Withington *et al.* 1991). The pressure–based methods obtain the pressure field via a pressure or a pressure correction equation which is formulated by manipulating the continuity and momentum equations (Patankar 1980, Issa 1986, Shyy 1993). The solution procedure is conventionally sequential in nature and hence can more easily accommodate a varying number of governing equations depending on the physics of the problem involved, without the necessity of reformulating the entire algorithm. Pressure–based methods can be extended to compressible flows by taking the dependence of density on pressure into account, via the equation of state (Rhie 1986, Shyy & Braaten 1988, Shyy *et al.* 1992b).

While the density–based methodology has been widely used for many compressible aerodynamic computations (MacCormack & Baldwin 1975, Jameson *et al.* 1981, Thomas *et al.* 1985, Kamath 1989, Davis 1992), the pressure–based methodology has been a popular one for gas–turbine combustors (Patankar 1980, Shyy *et al.* 1986, Priddin & Coupland 1986, Sturgess 1986, Shyy *et al.* 1989). The pressure–based methods have proven to be quite robust and effective in handling complex fluid physics including turbulence–chemistry interactions; however, they have not been widely applied to high Mach number flows until recently. Works by Rhie (1986), Shyy & Braaten (1988), Chen (1989), and Shyy *et al.* (1992b) have, however, demonstrated the capability of the pressure–based approach in

handling high speed flows including those in the hypersonic regime; in parallel, effort has also been devoted towards advancing the density–based method for treating the wide variation of flow speeds as well as strong source terms created by the interaction between turbulence and combustion (Shuen *et al.* 1992).

For any computational algorithm, the accuracy of the numerical prediction and the stability of the computational procedure are two of the most critical issues. These issues stem from the numerical modelling of the various terms in the governing partial differential equations, such as the unsteady, the diffusion, the convection and the source terms. In the present thesis, we focus our attention for the most part on numerical simulation of steady flows and hence we do not address the issue of the interaction of the unsteady terms with the the other terms (this issue is by no means trivial and deserves attention in its own right). In terms of computational difficulty, the diffusion terms in the Navier–Stokes equations are quite docile due to their linear nature, their physically diffusive property and the fact that the standard second–order central difference operator for the second derivative is numerically quite stable. On the other hand, from the point of view of the accuracy of the numerical prediction of a Navier–Stokes algorithm, the convection terms are the most critical. The second–order central difference operator for the first–derivative convection terms, though quite accurate for low cell Peclet numbers, gives rise to wiggles when the local cell Peclet number is greater than some critical value (Gresho & Lee 1981, Shyy 1985a); for the one–dimensional linear Burgers equation, the critical value is 2. To overcome this problem, the first–order upwind scheme has been widely used, but the excessive numerical dissipation inherent to this scheme has necessitated the search for more accurate schemes (Leonard 1979). The so–called hybrid scheme uses the central difference operator for regions in the flowfield with cell Peclet numbers less than 2 and the first–order upwind operator without physical diffusion otherwise. But, for convection–dominated flows, this again leads to the use of the first–order upwind scheme for a majority of the flowfield, leading to an excessive smearing of the solution profiles, especially the sharp gradients in the flowfield. To achieve

better accuracy, higher–order upwind schemes such as the second–order upwind scheme (Warming & Beam 1976, Vanka 1987) and the Quadratic Upwind Interpolation for Convective Kinematics (QUICK) scheme (Leonard 1979, 1988) have been proposed. However, the findings for these schemes listed in literature are quite disparate both in terms of accuracy and stability. Several issues such as the effect of conservative and consistent formulations of these schemes on the accuracy and stability of the overall algorithm are not adequately resolved. From the point of view of controlling spurious oscillations in solution profiles near sharp gradients and discontinuities such as shocks while achieving high accuracy throughout the flowfield, several higher–order accurate shock capturing schemes, most notably the Total Variation Diminishing (TVD) schemes have been designed (Harten 1983, 1984, Yee 1985). These schemes– –though extensively used in density–based simultaneous solvers to simulate shocks with high resolution– –have not yet been extended to pressure–based sequential solvers to obtain accurate simulations of flows, especially for high cell Peclet number flows and flows involving sharp solution gradients.

Another issue that deals with the accuracy and robustness of numerical flow simulations is the modelling of source terms. Fluid flows with complex physicochemical mechanisms such as turbulence, combustion and chemical reactions involve source terms which can be stiff enough to render any attempt at obtaining a numerical solution by conventional algorithms meaningless due either to a generation of spurious oscillations in the solution or to numerical instability (LeVeque & Yee 1990). Thus, special source term treatments such as the MacCormack's predictor–corrector method or Strang's operator–spitting method (Strang 1968) have been proposed (Chang 1990, LeVeque & Yee 1990) to ensure both numerical stability and the physical realizability of the solution. The issue of accurately treating stiff source terms in the presence of complex fluid phenomena is largely unresolved and is a subject of much ongoing research.

In view of the merits of pressure–based sequential algorithms, most notably their ability to handle flows with a wide range of Mach numbers and the relative ease of extension

to a varying number of governing equations, the well known SIMPLE (*Semi Implicit Method for Pressure Linked Equations*) algorithm– –popularized by Patankar (1980), Shyy (1993), etc.– –is adopted in the present thesis. Within the framework of this algorithm, an attempt is made to develop robust numerical schemes with an intent to resolve some of the important issues discussed above that relate to accuracy and stability of numerical predictions of fluid flows. However, all the issues addressed in the present thesis are equally applicable to any generic pressure–based sequential algorithm. The focus of the present thesis is on an investigation and development of some approaches for modelling convection and source terms in the Navier–Stokes equations and a study of their interaction with complex fluid phenomena such as recirculation and turbulence accompanied by sharp gradients in the flowfield.

Specifically, for the convection terms, two approaches are explored here. One approach is based on a geometric interpretation of the fluxes at control volume interfaces. For example, the flux at a control volume interface for the first–order upwind scheme is obtained by a constant (flat) extrapolation from the upwind neighbor, whereas for the second–order upwind scheme it is obtained by a linear extrapolation of two upwind neighbors. In Chapter II of the present thesis, higher–order upwind schemes– –the second–order upwind and the QUICK schemes– –are formulated in a unified framework with the first–order upwind scheme as the basis. Their performance is compared with conventional convection schemes, such as central difference and first–order upwind schemes, within the framework of the pressure–based SIMPLE algorithm. The issue of conservative formulation of a convection scheme is also investigated by devising conservative and non–conservative formulations of the second–order upwind scheme. Another important issue studied in this context is the consistency of boundary treatments for these high–order upwind schemes which have a stencil spanning more than two grid points. In Chapter II we also present a brief overview of the SIMPLE algorithm employed in the present study.

The second approach for modelling convection terms in the present work involves the introduction of an appropriate amount of nonlinear numerical dissipation into the central difference scheme; this approach forms the basis of the modern shock capturing schemes. The modern high resolution shock capturing schemes, notably TVD schemes, have so far been implemented effectively and reliably only in density–based simultaneous solvers (Yee *et al.* 1985, Colella 1990). In Chapter III an attempt is made to understand the issues concerning the application and implementation of these high resolution shock capturing schemes in the context of the pressure–based sequential algorithm to solve Navier–Stokes equations, thus extending the capability of pressure–based algorithms to resolve sharp flow gradients, caused by high Reynolds number or Mach number, and/or source terms. To better understand the implementation issues for these schemes applied to two–dimensional Navier–Stokes equations in the context of simultaneous and sequential solvers, the system of one–dimensional inviscid gas dynamics (Euler) equations is chosen for study in this chapter. The unsteady shock tube problem with and without the interaction of the various discontinuities (shock wave, contact discontinuity and expansion fan) with the boundaries of the shock tube and the resonant pipe problem are used as test cases.

Before going on to extend the framework developed in Chapter III from one–dimensional Euler equations to multi–dimensional Navier–Stokes equations, the issue of treatment of source terms is addressed next, in Chapter IV. The one–dimensional sequential solver developed in Chapter III is utilized for this purpose along with special techniques for effectively handling source terms. Specifically, MacCormack's predictor–corrector method and Strang's operator–spitting method are investigated. A one–dimensional longitudinal combustion instability problem which has a strong heat release source term is chosen for study. The combustion instability phenomenon is important from the point of view of practical applications and is a complex physical problem. It is not the intention of the present thesis to get involved with the complex physics associated with combustion instabilities. Instead, the idea here is to utilize the strong interaction of the heat

release source term with the other terms in the governing equations to illustrate the numerical difficulties caused by stiff source terms and to show how special source term treatments can resolve these difficulties, yielding a satisfactory numerical solution. Thus, for the purpose of the present thesis, a simplified model combustion instability problem is used as a means to demonstrate the efficacy of the numerical algorithm developed to handle source terms.

Next, based on the understanding– –gained from Chapter III– –of the key issues regarding the extension of TVD schemes to sequential solvers, a controlled variation scheme (CVS) in the framework of the multi–dimensional pressure–based sequential solver has been developed in Chapter V for obtaining high accuracy in complex recirculating flows with sharp flow gradients. Among the test cases investigated is the one–dimensional linear convection–diffusion equation with and without a source term and two–dimensional incompressible flows in a lid–driven cavity and over a backward–facing step. The interaction of the nonlinear dissipation employed by the CVS with the sharp gradients in the flowfield is investigated by examining the effective cell Peclet numbers.

At this point, a justification for investigating simple model problems in detail is in order. For the Navier–Stokes equations containing the nonlinear convection terms and stiff source terms (for some applications) the analysis of complex multi–dimensional fluid flow problems using advanced numerical schemes is very difficult. The understanding of the mechanism by which the numerical scheme operates is lost while studying complex multi–dimensional flows. The only way to understand the operation of a numerical scheme and to analyze the interactions among the various physical and numerical mechanisms that lead to the final flowfield is to apply the numerical scheme to a simplified model problem. This serves to delineate the various elements of a numerical scheme and, in the author's opinion, is absolutely critical in attaining a better insight into the overall algorithm. In the present thesis, the emphasis is on understanding the key issues associated with the various numerical schemes via relatively simple test cases which is expected to lay a firm foundation for future work involving practical flow problems exhibiting complex physics.

Having addressed some key issues in the numerical approximations of convection and source terms for laminar flows, the performance of the CVS for two–dimensional incompressible turbulent flows is assessed in Chapter VI. The true utility of the the CVS is not for laminar recirculating flows in general for which the central difference scheme performs quite satisfactorily (at least for the cases presented in the present thesis). It is for problems such as turbulent, recirculating flows which use closure models and possess strong source terms, that the central difference scheme often breaks down. For such flows, the CVS becomes truly useful and this is demonstrated in Chapter VI. The well known k–ε model is used to compute turbulent viscosity in the flowfield. The interaction of the CVS with the turbulence model is investigated.

Finally, some general conclusions based on all the issues investigated in the present study are presented in Chapter VII along with some recommendations for future investigation.

CHAPTER II
UNIFIED FORMULATION OF SOME CONVENTIONAL SCHEMES

2.1. Background

This chapter deals with the formulation and performance of four convection schemes, namely, first–order upwind, central difference, and second–order upwind schemes and a scheme based on quadratic upwind interpolation, called the Quadratic Upstream Interpolation for Convective Kinematics (QUICK) scheme (Leonard 1979). The second–order central difference operator for the first derivative convection terms, though quite accurate for low cell Peclet numbers, gives rise to wiggles when the local cell Peclet number is greater than some critical value (Gresho & Lee 1981, Shyy 1985a); for the one–dimensional linear Burgers equation, the critical value is 2. To overcome this problem, the first–order upwind scheme has been widely used but the excessive numerical dissipation inherent to this scheme has necessitated the search for more accurate schemes. The so–called hybrid scheme uses the central difference operator for regions in the flowfield with cell Peclet numbers less than 2 and the first–order upwind operator otherwise. But, for convection–dominated flows, this again leads to the use of the first–order upwind scheme for a majority of the flowfield, leading to excessive smearing of the solution profiles, especially the sharp gradients in the flowfield.

To take advantage of the concept of upwinding, while achieving higher accuracy, higher–order upwind schemes, such as the second–order upwind scheme (Warming & Beam 1976, Shyy 1985a, Vanka 1987, Jiang *et al.* 1990) and the QUICK scheme (Leonard 1979, 1988a, 1988b) have been proposed. The second–order upwind scheme has received mixed reviews in the literature– –some researchers have criticized its accuracy and convergence

characteristics (Vanka 1987) while others have found it satisfactory (Jiang *et al.* 1990). Shyy (1985a) demonstrated that, based on both linear analysis and model problem testing, the second–order upwind scheme, although not free from difficulties and inaccuracies, is generally more satisfactory than several other alternatives proposed in the literature. The same observation is also made in the context of three–dimensional turbulent flow computations (Vu & Shyy 1990). Vanka (1987), on the other hand, found that the second–order upwind scheme does not yield satisfactory performance, both in terms of numerical accuracy and computational stability, for solving the two–dimensional driven cavity flow for several Reynolds numbers and finite difference grids. It is shown here that the key to this discrepancy lies in the fact that within a control volume formulation, a conservative and consistent formulation of second–order upwinding at the control volume interfaces is required to produce an accurate and well behaved scheme. The QUICK scheme too has received mixed reviews (Leonard 1979, 1988a, 1988b, Huang *et al.* 1985, Hayase *et al.* 1992), but more in terms of convergence rates. It seems that the differences in the actual implementation of the same basic conservative form of the scheme may be responsible for these inconsistent findings.

The design philosophy adopted for the convection schemes presented in this chapter is based on a geometric interpretation of the fluxes at control volume interfaces. Based on the geometric shape function employed to interpolate or extrapolate the values of the dependent variable at neighboring grid points in order to estimate the flux at a control volume interface, four schemes are derived in this chapter, namely, the first–order upwind, the central difference, the second–order upwind and the QUICK scheme. Schemes obtained in the manner described above are strictly conservative and consistent. An attempt is also made to compare the accuracy of conservative and non–conservative implementations of higher–order upwind schemes by devising a conservative and a non–conservative formulation of the second–order upwind scheme. Both formulations have the same order of accuracy according to the formal Taylor series analysis but substantial differences in solution accuracy exist between the two. An interpretation is presented from the viewpoint of finite

volume/finite difference procedures, and the preferable implementation is suggested. As for the central difference scheme, it is found that although simple model problem analysis (Shyy 1985a, Fletcher 1988) indicates that the second–order central difference scheme is prone to oscillations beyond a cell Reynolds number of 2, it exhibits very robust performance for the driven cavity flow with no signs of numerical oscillation. Some interesting features are observed for the schemes and will be discussed in the context of cell Reynolds number distribution.

With regard to stability and convergence of these convection schemes, two versions (both conservative and consistent) of the second–order upwind and the QUICK schemes are tested. In the first version, the first–order upwind scheme is used as the "basis" and thus the coefficient matrix obtained for the second–order upwind and QUICK schemes is the same as that for the first–order upwind scheme; the balance of the terms are placed in the source term. The coefficient matrix thus maintains diagonal dominance. In the second version, the coefficient matrix is constructed by using all the coefficients of the four immediate neighbors (east, west, north and south), without regard to diagonal dominance. Both versions, obviously, yield identical results. However, it is observed that the former version is robust in terms of stability of the overall computation with respect to the number of grid points and the relaxation factors employed.

Another issue of interest in the present chapter is the boundary treatment associated with the various convection schemes. Due to the staggered nature of the grids employed for control volumes associated with u– and v–velocities and scalar variables such as pressure, different boundary treatments are required for control volumes adjacent to different boundaries of the physical domain. Also, different types of boundary variable specifications, such as for inflow and outflow boundaries, necessitate different formulations. Moreover, the issue of treating the fluxes in the control volumes adjacent to the physical boundaries, using staggered grids, in a conservative and consistent manner, has not been adequately addressed in the literature. It is desirable to identify the consistency of the various boundary treatment options across the interfaces of boundary control volumes as well as the local order of

accuracy of these options, and to correlate them to the overall solution accuracy. This chapter attempts to clarify these issues by analyzing the various options that arise from the conflicting requirements of maintaining consistency across the control volume interfaces and local accuracy. A detailed presentation is made of the formulations resulting from the various boundary treatments, in order to clearly delineate the variations of numerical implementation, of the higher–order upwind schemes, that are required near the domain boundaries. The driven cavity flow problem is used as the test case.

2.2. Formulation of the Convection Schemes

Typical control volumes employed for the u–velocity components in the staggered grid arrangement are shown in Fig. 2.1. The SIMPLE algorithm (Patankar 1980) employed here solves the governing equations in a sequential manner. The velocity components are computed from the respective momentum equations. The velocity and the pressure fields are corrected using a pressure correction equation which is derived by manipulating the continuity and momentum equations. The correction procedure leads to a continuity satisfying velocity field. The whole process is repeated until the desired convergence level is reached.

In this section, we briefly outline the derivation of second–order central difference, first– and second–order upwind and QUICK schemes. The momentum equations for steady, incompressible fluid flow can be written as follows:

$$\frac{\partial}{\partial x}\left(\varrho u\phi - \mu\frac{\partial\phi}{\partial x}\right) + \frac{\partial}{\partial y}\left(\varrho v\phi - \mu\frac{\partial\phi}{\partial y}\right) = -\left(\frac{\partial p}{\partial x} \text{ or } \frac{\partial p}{\partial y}\right) \tag{2.1a}$$

where $\phi = u$ or v, and the continuity equation can be written as

$$\frac{\partial}{\partial x}(\varrho u) + \frac{\partial}{\partial y}(\varrho v) = 0 \tag{2.1b}$$

Integrating these equations over the control volume shown in Fig. 2.1, we get for the momentum equation:

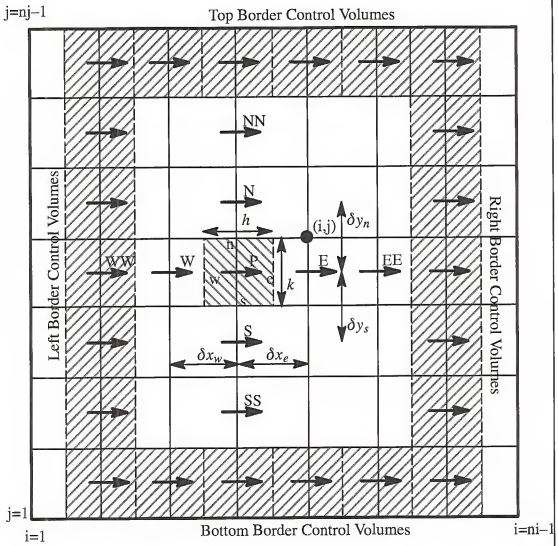

Fig. 2.1. Internal and border u–control volumes.

$$F_e\phi_e - F_w\phi_w + F_n\phi_n - F_s\phi_s = D_e(\phi_E - \phi_P) - D_w(\phi_P - \phi_W) + D_n(\phi_N - \phi_P) - D_s(\phi_P - \phi_S) + S \tag{2.2a}$$

where S denotes source terms such as pressure gradients. The continuity equation can be written as

$$F_e - F_w + F_n - F_s = 0 \tag{2.2b}$$

where

$$F_e = (\varrho u)_e \, k \qquad F_w = (\varrho u)_w \, k$$

$$F_n = (\varrho v)_n \, h \qquad F_s = (\varrho v)_s \, h \tag{2.3a}$$

$$D_e = \frac{\mu_e \, k}{\delta x_e} \qquad D_w = \frac{\mu_w \, k}{\delta x_w}$$

$$D_n = \frac{\mu_n \, h}{\delta y_n} \qquad D_s = \frac{\mu_s \, h}{\delta y_s} \tag{2.3b}$$

where δx_e , δy_n, etc. are the distances shown in Fig. 2.1. F's are the convection fluxes and D's the diffusion fluxes at the control volume interfaces and are estimated by a linear interpolation between the two neighbors to either side of the control volume interfaces. For example, the convection and diffusion fluxes on the east interface, F_e, are respectively estimated as

$$F_e = (\varrho u)_e \, k = \frac{1}{2}(\varrho_P + \varrho_E) \cdot \frac{1}{2}(u_P + u_E) \; k \tag{2.4a}$$

and

$$D_e = \frac{\mu_e \, k}{\delta x_e} = \frac{1}{2}(\mu_P + \mu_E) \cdot \frac{k}{\delta x_e} \quad . \tag{2.4b}$$

The variable ϕ at a control volume interface can be determined using an interpolation involving the values of ϕ at one or more of the grid point neighbors of the interface. The choice of the type and the geometric shape of the interpolation profile dictates the type and the local order of accuracy of the convection scheme. Different convection schemes use different interpolations, as described below.

2.2.1 First–Order Upwind Scheme

For the first–order upwind scheme, the value of ϕ at any control volume interface is estimated using the value at the upwind neighbor. Thus, as is well known, the value ϕ_e at the east face is assigned the value ϕ_P if the flux F_e is positive, and the value ϕ_E if the flux F_e is negative. This choice of extrapolation scheme amounts to a piecewise constant profile, with no variation allowed between the values of ϕ at two adjacent nodes along the one–dimensional convection field, as illustrated in Fig. 2.2. This can be conveniently summarized as

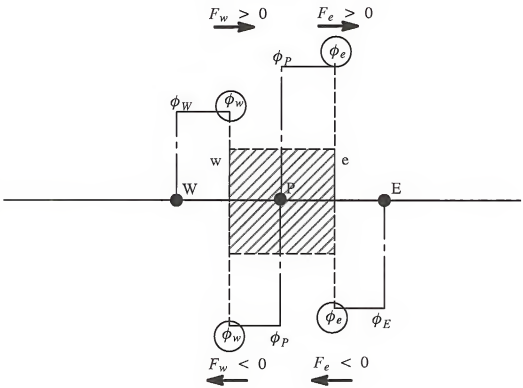

Fig. 2.2. Schematic of the extrapolation for the first–order upwind scheme.

$$F_e\phi_e = \phi_P[\![F_e, 0]\!] - \phi_E [\![-F_e, 0]\!] \tag{2.5}$$

where the symbol $[\![p, q]\!]$ represents the maximum of the two operands p and q. Using the above equation (2.5), Eq. (2a) can be written in the form

$$A_P\phi_p = A_E\phi_E + A_W\phi_W + A_N\phi_N + A_S\phi_S + b \tag{2.6}$$

and for the first–order upwind scheme, after subtracting the continuity equation (2b) multiplied by ϕ_P from the momentum equation Eq. (2.2a), we get

$$\begin{aligned} A_E &= D_e + [\![-F_e, 0]\!] \\ A_W &= D_w + [\![F_w, 0]\!] \\ A_N &= D_n + [\![-F_n, 0]\!] \\ A_S &= D_s + [\![F_s, 0]\!] \end{aligned} \tag{2.7}$$

$$A_P = A_E + A_W + A_N + A_S$$

and $b=0$. A Taylor series expansion about the point P gives

$$\frac{\partial \phi_P \phi_P}{\partial x} = 2\phi_P \phi_P' + \frac{h}{2}\left[-\phi_P \phi_P'' - \phi_P' \phi_P'\right] + h^2\left[\frac{5}{24}\phi_P \phi_P''' + \frac{3}{8}\phi_P' \phi_P''\right] + \ldots.. \tag{2.8}$$

showing that the scheme is locally first–order accurate.

2.2.2 Central Difference Scheme

Here, as depicted in Fig. 2.3, ϕ at any interface is estimated by a linear interpolation between the two grid point neighbors on either side of the interface, regardless of the direction of local convection; for example

$$F_e \phi_e = F_e \frac{1}{2}(\phi_P + \phi_E) \tag{2.9}$$

and now the coefficients in Eq. (2.6), after subtracting the continuity equation (2.2b) multiplied by ϕ_P from Eq. (2.2a), become

$$\begin{aligned} A_E &= D_e - \frac{F_e}{2} \\ A_W &= D_w + \frac{F_w}{2} \\ A_N &= D_n - \frac{F_n}{2} \\ A_S &= D_s + \frac{F_s}{2} \\ A_P &= A_E + A_W + A_N + A_S \end{aligned} \tag{2.10}$$

and $b=0$. For the central difference scheme, doing a Taylor series expansion about the point P, as before, gives

$$\frac{\partial \phi_P \phi_P}{\partial x} = 2\phi_P \phi_P' + h^2\left[\frac{5}{24}\phi_P \phi_P''' + \frac{3}{8}\phi_P' \phi_P''\right] + \ldots \tag{2.11}$$

indicating that the scheme is second–order accurate locally.

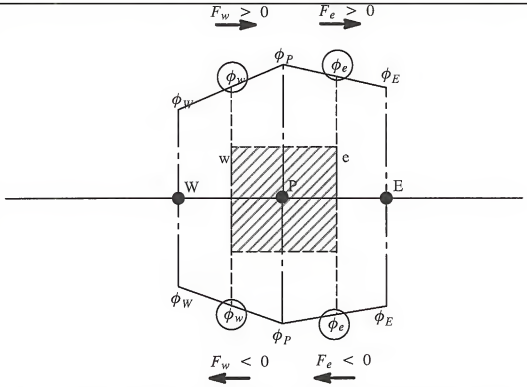

Fig. 2.3. Schematic of the linear interpolation for the central difference scheme.

2.2.3 Second–Order Upwind Scheme

Possible alternatives of the second–order upwind scheme that can be cast in the form of Eq. (2.6) have been reported in the literature, e.g., Shyy (1985), Vanka (1987), Jiang *et al.* (1990), resulting in different handling of the fluxes across the control surface. Moreover, the value of a dependent variable at the finite–volume interfaces can be determined by referring to the sign of the flux either at the interface or at the node where the unknown ϕ is located, depending on the design of a particular scheme. Two alternative schemes have been chosen for study here; they are labelled as Scheme A and Scheme B.

2.2.3.1 Non–conservative formulation: Scheme A

In terms of a straightforward finite difference approximation, the second–order upwind scheme can be written as the following:

$$\left.\frac{\partial(u\phi)}{\partial x}\right|_P = \frac{1}{2h}\left(3u_P\phi_P - 4u_W\phi_W + u_{WW}\phi_{WW}\right) + T_u \ , \qquad \text{for } u > 0 \ ,$$

$$= \frac{1}{2h}\left(-u_{EE}\phi_{EE} + 4u_E\phi_E - 3u_P\phi_P\right) + T_u \ , \qquad \text{for } u < 0 \ . \tag{2.12}$$

where T_u is the truncation error of the discretization scheme. This formula is not consistent with a finite volume formulation.

Scheme A is devised from the finite difference form of the second–order upwind scheme, i.e., Eq. (2.12), by rearranging the terms and using the appropriate coefficients and fluxes at the cell interfaces to suit the control volume formulation, and by enforcing diagonal dominance in the assembly of coefficients. Moreover, it tests for the sign of the fluxes at the point P to determine the upwind direction. Due to these reasons, Scheme A is a non–conservative scheme. If u at point P is positive, the convective flux at the west face, for example, is approximated by

$$\frac{\partial(u\phi)}{\partial x} = A_P\phi_P - A_W\phi_W + b_W \tag{2.13}$$

with the following coefficients:

$$A_W = \frac{1.5}{h}\ u_w$$

$$A_P = A_W \tag{2.14}$$

$$b_w = \frac{0.5}{h}\ \frac{(u_W + u_{WW})}{2}\ (\phi_{WW} - \phi_W) \ .$$

For the u–momentum equation, i.e., $\phi = u$, if we do a Taylor series expansion of all the terms about the point P, then the truncation error of Eq. (2.13) is

$$h^2\left(-\frac{1}{3}\phi_P\phi_P^{'''} - \phi_P^{'}\phi_P^{''}\right) + h^3\left(\frac{1}{4}\phi_P\phi_P^{IV} + \phi_P^{'}\phi_P^{'''} + \frac{3}{4}\phi_P^{''\,2}\right) + O(h^4) \tag{2.15}$$

The above error means that the formula expressed as Eq. (2.13) is second–order accurate with respect to the grid spacing h. The discretization for Scheme A is in the form of Eq. (2.6) where

$$A_N = D_n + \frac{3}{2}[\![-F_n, 0]\!]$$

$$
\begin{aligned}
A_S &= D_s + \frac{3}{2}[\![F_s, 0]\!] \\
A_E &= D_e + \frac{3}{2}[\![-F_e, 0]\!] \\
A_S &= D_s + \frac{3}{2}[\![F_s, 0]\!] \\
A_P &= A_E + A_W + A_N + A_S
\end{aligned}
\tag{2.16}
$$

$$
\begin{aligned}
b &= \frac{h}{2}\left\{\left(\frac{v_{NN} + v_N}{2}\right)\left[(\varrho\phi)_{NN} - (\varrho\phi)_N\right] B_N + \left(\frac{v_{SS} + v_S}{2}\right)\left[(\varrho\phi)_S - (\varrho\phi)_{SS}\right] B_S\right\} \\
&+ \frac{k}{2}\left\{\left(\frac{u_{EE} + u_E}{2}\right)\left[(\varrho\phi)_{EE} - (\varrho\phi)_E\right] B_E + \left(\frac{v_{WW} + v_W}{2}\right)\left[(\varrho\phi)_W - (\varrho\phi)_{WW}\right] B_W\right\}
\end{aligned}
$$

with

$$
B_N = \frac{[\![-F_n, 0]\!]}{(-F_n)} \qquad B_S = \frac{[\![F_s, 0]\!]}{F_s}
$$

$$
B_E = \frac{[\![-F_e, 0]\!]}{(-F_e)} \qquad B_W = \frac{[\![F_w, 0]\!]}{F_w}
$$

and the D's and F's are defined in Eq. (2.3).

Scheme A is designed from the finite difference approximation with the goal of maximizing the diagonal dominance of the coefficient matrix. Hence, in Eq. (2.13), A_P is taken to be the same as A_W, while all the remaining terms are put explicitly in the source term. The flux term A_W is estimated based on the standard averaging procedure, i.e., it is taken as the mean of u_W and u_P .

2.2.3.2 Conservative formulation: Scheme B

Scheme B uses a linear extrapolation of the two upwind neighbors to determine ϕ and is derived exactly by integrating the fluxes over the control volume. Hence it is completely conservative and consistent with the control volume formulation. The upwind directions are determined by the sign of the fluxes at the control volume interfaces.

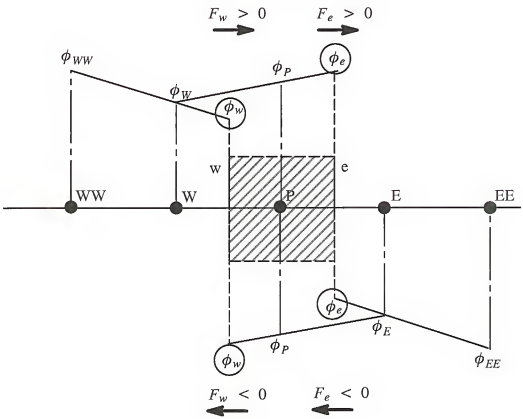

Fig. 2.4. Schematic of the linear extrapolation for the second–order upwind scheme.

In this case, we estimate ϕ at any interface by a linear extrapolation of the ϕ values at two upwind neighbors, as shown in Fig. 2.4. Thus, for example, depending on the sign of F_e , we estimate ϕ_e as

$$\phi_e = \frac{3}{2}\phi_P - \frac{1}{2}\phi_W \quad , \quad \text{if } F_e > 0 \ , \tag{2.17a}$$

$$\phi_e = \frac{3}{2}\phi_E - \frac{1}{2}\phi_{EE} \quad , \quad \text{if } F_e < 0 \ . \tag{2.17b}$$

which can be summarized as follows

$$F_e\phi_e = \left(\frac{3}{2}\phi_P - \frac{1}{2}\phi_W\right) [\![F_e, 0]\!] - \left(\frac{3}{2}\phi_E - \frac{1}{2}\phi_{EE}\right) [\![-F_e, 0]\!] \tag{2.18}$$

Similar expressions can be written for the other interfaces. Thus, Scheme B is based on a weighted estimation of the fluxes as indicated by Eq. (2.17). One can see the motivation of scheme B more clearly by noting that in the spirit of finite volume formulation, $\partial\phi/\partial x$ can be expressed in a generic form as

$$\frac{\partial\phi}{\partial x} = \frac{\phi_e - \phi_w}{h} \tag{2.19}$$

where ϕ_e and ϕ_w are calculated based on the piecewise linear extrapolation given by equations similar to Eq. (2.17).

Many alternatives can be devised to implement the second–order upwind scheme into the standard notation typified by Eqs. (2.7) and (2.10). Here, we investigate two versions of the second–order upwind scheme.

Version 1 of second–order upwind scheme B

In the first version, we use the first–order upwind scheme as the "basis" and assign the difference between the two schemes to the source term b, which are treated explicitly. This arrangement offers a simple and straightforward way to implement more complicated schemes in general, including not only the second–order upwind scheme but also QUICK and other schemes. A merit of such a treatment is that it maintains diagonal dominance in the course of the iterative updating. As will be discussed later, especially for a scheme such as QUICK, the type of formulation of the scheme is very critical for yielding a converged solution for a large size of grid employed for numerical computation. For this version of the second–order upwind scheme, we have the following:

$$F_e u_e = \left[u_P + \frac{1}{2}(u_P - u_W)\right][\![F_e, 0]\!] - \left[u_E + \frac{1}{2}(u_E - u_{EE})\right][\![-F_e, 0]\!] \tag{2.20}$$

Similar to the first–order upwind and second–order central difference schemes, we subtract the continuity equation (2.2b) multiplied by ϕ_P and now all the coefficients are the same as that for the first–order upwind scheme, i.e., those given by Eq. (2.7). However, we now have the following form for the source term b:

$$
\begin{aligned}
b = & -\tfrac{1}{2}(\phi_P - \phi_W)[\![F_e, 0]\!] + \tfrac{1}{2}(\phi_E - \phi_{EE})[\![-F_e, 0]\!] \\
& + \tfrac{1}{2}(\phi_W - \phi_{WW})[\![F_w, 0]\!] - \tfrac{1}{2}(\phi_P - \phi_E)[\![-F_w, 0]\!] \\
& - \tfrac{1}{2}(\phi_P - \phi_S)[\![F_n, 0]\!] + \tfrac{1}{2}(\phi_N - \phi_{NN})[\![-F_n, 0]\!] \\
& + \tfrac{1}{2}(\phi_S - \phi_{SS})[\![F_s, 0]\!] - \tfrac{1}{2}(\phi_P - \phi_N)[\![-F_s, 0]\!]
\end{aligned}
\tag{2.21}
$$

<u>Version 2 of second–order upwind scheme B</u>

If we assemble the fluxes along the x– and y–directions and express the resulting equation in the form of Eq. (2.6), without using the continuity equation (2.2b) to manipulate the momentum equations, as we did in the case of first–order and central difference schemes, we obtain version 2 for which the coefficients are as follows:

$$
\begin{aligned}
A_E &= D_e + \tfrac{3}{2}[\![-F_e, 0]\!] + \tfrac{1}{2}[\![-F_w, 0]\!] \\
A_W &= D_w + \tfrac{3}{2}[\![F_w, 0]\!] + \tfrac{1}{2}[\![F_e, 0]\!] \\
A_N &= D_n + \tfrac{3}{2}[\![-F_n, 0]\!] + \tfrac{1}{2}[\![-F_s, 0]\!] \\
A_S &= D_s + \tfrac{3}{2}[\![F_s, 0]\!] + \tfrac{1}{2}[\![F_n, 0]\!] \\
A_P &= D_e + D_w + D_n + D_s + \tfrac{3}{2}[\![F_e, 0]\!] + \tfrac{3}{2}[\![-F_w, 0]\!] \\
&\qquad + \tfrac{3}{2}[\![F_n, 0]\!] + \tfrac{3}{2}[\![-F_s, 0]\!]
\end{aligned}
\tag{2.22}
$$

$$
b = -\tfrac{1}{2}\phi_{EE}[\![-F_e, 0]\!] - \tfrac{1}{2}\phi_{WW}[\![F_w, 0]\!] - \tfrac{1}{2}\phi_{NN}[\![-F_n, 0]\!] - \tfrac{1}{2}\phi_{SS}[\![F_s, 0]\!]
$$

Version 2 of the second–order upwind scheme does not maintain diagonal dominance, i.e., the coefficient A_P does not equal the sum of the four neighboring coefficients.

It must be noted that versions 1 and 2 are two forms of the same basic scheme, differing only in the diagonal dominance property. Thus, they both will converge to the same solution for any fluid flow problem; however, the convergence and numerical stability properties of the two versions are expected to be different– version 1 is expected to be more

stable and exhibit faster convergence due to the diagonal dominance in the coefficient matrix.

It must be noted that, contrary to a point made by Hayase *et al.* (1992), any form of the same basic scheme, whether it is second–order upwind or QUICK or any other, will be consistent and conservative as long as the following property holds:

$$(F_e u_e)_i = (F_w u_w)_{i+1} \tag{2.23}$$

and likewise for the other faces. Here, in order to evaluate the flux at any interface, we must use an expression of the form given by Eq. (2.20), which includes the coefficients A_P, A_E, etc. multiplied with the respective ϕ's and the source term b. Thus, any form of the scheme that satisfies the above requirement should converge to the same solution. If formulated appropriately, it is only the convergence and numerical stability properties of the different implementations which are expected to be different. As regards the formal order of accuracy of this scheme, a Taylor series expansion about the point P yields

$$\begin{aligned} \frac{\partial \phi_P \phi_P}{\partial x} &= 2\phi_P \phi_P' + h^2\left[-\frac{7}{24}\phi_P \phi_P''' - \frac{1}{8}\phi_P' \phi_P''\right] \\ &\quad + \frac{h^3}{4}\left[\phi_P' \phi_P''' + \phi_P \phi_P^{IV}\right] + \ldots \end{aligned} \tag{2.24}$$

exhibiting the second–order accuracy of this scheme.

Compared to the first–order upwind scheme, the shape function utilized for the extrapolation procedure for the second–order upwind scheme is of a higher order, allowing some variation in the solution profile between the adjacent nodes. There are some implications in this regard. Firstly, it may be recalled that the use of the first–order upwind scheme is basically justified by the observation that, for the high Reynolds number case of the one–dimensional linear Burgers equation, the solution profile is indeed piecewise constant ("flat") throughout the whole domain except in the thin layer next to the boundary. With the use of a linear extrapolation, instead of a piecewise constant extrapolation, the second–order upwind scheme appears capable of accommodating the flow field that contains the cell Reynolds numbers of wide ranges. In this aspect, one should note that for

a nominally high Reynolds number flow, the actual dominance of the convection effect relative to the viscous effect can vary considerably from one region to the other.

Besides Schemes A and B presented here, many other possibilities exist for implementing the second–order upwind schemes. For example, in the expression adopted by Vanka (1987), the upwind direction is estimated based on velocity values at point *P*. That formula is a straightforward implementation of a non–conservative form, similar to Scheme A discussed above. We have chosen to study Schemes A and B here in view of the different characteristics exhibited by their solutions, which can be attributed to their non–conservative and conservative formulations, respectively.

2.2.4 QUICK Scheme

The QUICK scheme has been proposed by Leonard (1979, 1988a). It uses a quadratic interpolation between two upstream neighbors and one downstream neighbor in order to estimate the ϕ value at any control volume interface, as shown in Fig. 2.5.

Depending on the sign of the flux at any interface, we estimate ϕ by a quadratic interpolation; for example, at the east face, we have

$$\phi_e = \frac{3}{8}\phi_E + \frac{3}{4}\phi_P - \frac{1}{8}\phi_W \quad , \quad \text{if } F_e > 0 \ , \tag{2.25a}$$

$$\phi_e = \frac{3}{4}\phi_E + \frac{3}{8}\phi_P - \frac{1}{8}\phi_{EE} \quad , \quad \text{if } F_e < 0 \ . \tag{2.25b}$$

which can be summarized as

$$\begin{aligned} F_e\phi_e = & \left(\frac{3}{8}\phi_E + \frac{3}{4}\phi_P - \frac{1}{8}\phi_W\right) [\![F_e, 0]\!] \\ & - \left(\frac{3}{4}\phi_E + \frac{3}{8}\phi_P - \frac{1}{8}\phi_{EE}\right) [\![- F_e, 0]\!] \end{aligned} \tag{2.26}$$

Version 1 of the QUICK scheme

Similar to the second–order upwind case, if we interpret the net convection flux employed by the QUICK scheme as composed of first–order upwind fluxes and source terms, we can write

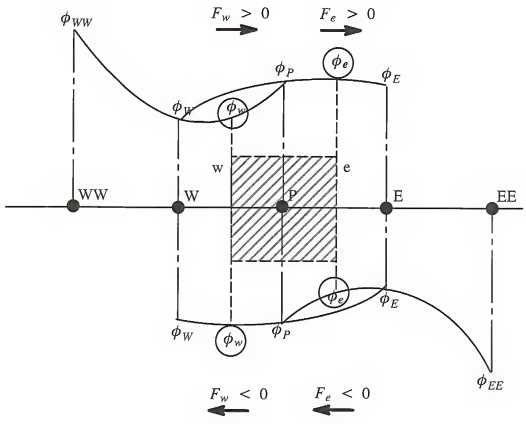

Fig. 2.5. Schematic of the quadratic interpolation for the QUICK scheme.

$$
\begin{aligned}
F_e\phi_e = & \left[\phi_P + \left(-\tfrac{1}{8}\phi_W - \tfrac{1}{4}\phi_P + \tfrac{3}{8}\phi_E\right)\right] [\![F_e, 0]\!] \\
& - \left[\phi_E + \left(\tfrac{3}{8}\phi_P - \tfrac{1}{4}\phi_E - \tfrac{1}{8}\phi_{EE}\right)\right] [\![-F_e, 0]\!]
\end{aligned}
\tag{2.27}
$$

Using expressions for all the fluxes, similar to above, and subtracting the continuity equation (2.2b) multiplied by ϕ_P from the resulting momentum equations, we get the same coefficients as for the first–order upwind scheme, i.e, those given by Eq. (2.7) along with the following form for b:

$$
\begin{aligned}
b \;=\; & -\left(-\tfrac{1}{8}\phi_P - \tfrac{1}{4}\phi_W + \tfrac{3}{8}\phi_E\right)[\![F_e, 0]\!] \;+\; \left(\tfrac{3}{8}\phi_P - \tfrac{1}{4}\phi_E - \tfrac{1}{8}\phi_{EE}\right)[\![-F_e, 0]\!] \\
& + \left(-\tfrac{1}{8}\phi_{WW} - \tfrac{1}{4}\phi_W + \tfrac{3}{8}\phi_P\right)[\![F_w, 0]\!] \;-\; \left(\tfrac{3}{8}\phi_W - \tfrac{1}{4}\phi_P - \tfrac{1}{8}\phi_E\right)[\![-F_w, 0]\!] \\
& - \left(-\tfrac{1}{8}\phi_P - \tfrac{1}{4}\phi_S + \tfrac{3}{8}\phi_N\right)[\![F_n, 0]\!] \;+\; \left(\tfrac{3}{8}\phi_P - \tfrac{1}{4}\phi_N - \tfrac{1}{8}\phi_{NN}\right)[\![-F_n, 0]\!] \\
& + \left(-\tfrac{1}{8}\phi_{SS} - \tfrac{1}{4}\phi_S + \tfrac{3}{8}\phi_P\right)[\![F_s, 0]\!] \;-\; \left(\tfrac{3}{8}\phi_S - \tfrac{1}{4}\phi_P - \tfrac{1}{8}\phi_N\right)[\![-F_s, 0]\!]
\end{aligned}
\tag{2.28}
$$

The present implementation, described by Eq. (2.28), is the same as that proposed by Hayase *et al.* (1992).

<u>Version 2 of the QUICK scheme</u>

Similar to the second–order upwind case, we have version 2 of the QUICK scheme in which we use the net fluxes of the form given by Eq. (2.26), without using the continuity equation (2.2b). In this version of the QUICK scheme, we place only the second neighbors of the grid point P into the source term b and thus do not enforce diagonal dominance in the coefficient matrix. For this version, the coefficients are

$$
\begin{aligned}
A_E &= D_e - \tfrac{3}{8}[\![F_e,\ 0]\!] + \tfrac{3}{4}[\![-F_e,\ 0]\!] + \tfrac{1}{8}[\![-F_w,\ 0]\!] \\
A_W &= D_w + \tfrac{3}{4}[\![F_w,\ 0]\!] - \tfrac{3}{8}[\![-F_w,\ 0]\!] + \tfrac{1}{8}[\![F_e,\ 0]\!] \\
A_N &= D_n - \tfrac{3}{8}[\![F_n,\ 0]\!] + \tfrac{3}{4}[\![-F_n,\ 0]\!] + \tfrac{1}{8}[\![-F_s,\ 0]\!] \\
A_S &= D_s + \tfrac{3}{4}[\![F_s,\ 0]\!] - \tfrac{3}{8}[\![-F_s,\ 0]\!] + \tfrac{1}{8}[\![F_n,\ 0]\!]
\end{aligned}
\tag{2.29}
$$

$$
\begin{aligned}
A_P \;=\; & D_e + D_w + D_n + D_s + \tfrac{3}{4}[\![F_e, 0]\!] - \tfrac{3}{8}[\![-F_e, 0]\!] - \tfrac{3}{8}[\![F_w, 0]\!] \\
& + \tfrac{3}{4}[\![-F_w, 0]\!] + \tfrac{3}{4}[\![F_n,\ 0]\!] - \tfrac{3}{8}[\![-F_n,\ 0]\!] - \tfrac{3}{8}[\![F_s,\ 0]\!] + \tfrac{3}{4}[\![-F_s,\ 0]\!]
\end{aligned}
$$

$$
b \;=\; -\tfrac{1}{8}\phi_{EE}[\![-F_e, 0]\!] - \tfrac{1}{8}\phi_{WW}[\![F_w, 0]\!] - \tfrac{1}{8}\phi_{NN}[\![-F_n, 0]\!] - \tfrac{1}{8}\phi_{SS}[\![F_s, 0]\!]
$$

As for the local order of accuracy of the QUICK scheme, if we do a Taylor series expansion about the velocity at the point P, we get

$$\frac{\partial \phi_P \phi_P}{\partial x} = 2\phi_P \phi_P{}' + h^2\left[\frac{1}{12}\phi_P \phi_P{}''' + \frac{1}{4}\phi'_P \phi_P{}''\right] + \frac{h^3}{16}\left[\phi_P{}' \phi_P{}''' + \phi_P \phi_P{}^{IV}\right] + \ldots \tag{2.30a}$$

which indicates that the scheme is second–order accurate. Since we employ a control volume approach, the Taylor series expansion about the control volume interfaces gives

$$\frac{u_e \phi_e - u_w \phi_w}{h} = \frac{u_e^2 - u_w^2}{h} + \frac{h^3}{16}\left[\frac{u_e u_e{}''' - u_w u_w{}'''}{h}\right] - \frac{3}{128}h^4\left[\frac{u_e u_e{}^{IV} - u_w u_w{}^{IV}}{h}\right] + \ldots \tag{2.30b}$$

The above expression indicates that if the fluxes across the east and west faces of the control volume are expressed strictly based on the central difference scheme, i.e., the first term on the right hand side of Eq. (2.30b), then the QUICK scheme is third–order accurate. However, this interpretation is not really meaningful since the order of accuracy of a scheme should be judged only by considering the original differential equation itself. Furthermore, the central difference scheme is not a good reference here, since it is the unsatisfactory performance of the central difference scheme in some cases that requires the development of alternatives such as the QUICK scheme.

Compared to the first– and second–order upwind schemes, the QUICK scheme assumes a parabolic shape profile for conducting the interpolation procedure. From this viewpoint, it seems that although QUICK is still a second–order scheme in terms of the formal order of accuracy, it can yield a higher degree of actual accuracy for many practical computations. However, on the other hand, it is well known that the performance of a convection scheme is not correlated with either the degree of formal order of accuracy or the complexity of the scheme. Is has been shown by Shyy (1985), for instance, that for the linear Burgers equation, the critical cell Peclet number for the QUICK scheme is 8/3, which is only slightly higher than that for the second–order central difference scheme (namely, 2). Hence,

the actual performance of the scheme depends on the balance between the higher order upwind extrapolation profile and the weaker ability of resisting spurious oscillations. It is not appropriate to make a universal assertion regarding the relative performance among these higher–order upwind schemes since their performance can vary for different physical problems.

2.3. Boundary Treatments: u–Control Volumes

The boundary treatment entails the treatment of the border control volumes shown in Fig. 2.1. Different cases arise for different convection schemes employed for the "internal" control volumes (e.g., control volume for point P in Fig. 2.1) which are defined as the control volumes not adjacent to the boundaries, i.e., the control volumes in the domain other than the "border" control volumes shown in Fig. 2.1. For the left and right border u–control volumes (and the top and bottom v–control volumes), the use of two–point schemes, such as the first–order upwind and the second–order central difference schemes, involves treatment identical to any internal control volume. However, the schemes with a larger stencil such as the second–order upwind and the QUICK schemes cannot be applied at the border control volume interfaces nearest to the boundary, if the direction of the convective flux is inwards from the boundary, since such schemes would require grid points outside the physical boundary of the domain. For these schemes, one has to use a two–point scheme such as the first–order upwind or the central difference scheme for the interface nearest to the boundary. However, for the other ("interior") interface of these border control volumes, one is free to choose between a two–point scheme or the larger–stencil scheme being used for the internal control volumes. It is these options that we wish to formulate in this section and evaluate in the next.

The remaining border control volumes, namely, the top and bottom u–control volumes (and the left and right v–control volumes), entail a new aspect in that one of the interfaces lies on the boundary. For these interfaces, no extrapolation or interpolation is

required since the values of ϕ on these faces are specified by the given boundary conditions. For the other ("interior") face, once again we are free to choose either a two–point scheme or the larger–stencil scheme which is being used for the internal control volumes. The use of the larger–stencil scheme for the interior face of these border control volumes introduces a new aspect, namely, the distances between the interior face and the two upwind neighbors are no longer the same as those for an interface belonging to an internal control volume. This leads to a modification of the coefficients, as will be discussed in detail in this section.

We will present here a detailed discussion for the left and bottom border u–control volumes. For sake of brevity and to minimize confusion, the boundary treatment for only Version 1 of the second–order upwind and QUICK schemes will be presented here. The equations corresponding to Version 2 and those for the right and top border u–control volumes, as well as those for all of the border v–control volumes can be derived in a similar manner, and will not be presented here.

2.3.1 Left Border Control Volumes

The situation for the left border control volumes is shown in Fig. 2.6. For this control volume, we have $u_W = u(boundary)$ which is determined from the type of boundary condition specified:

$$Dirichlet\ \ B.C. \quad : \quad u_W \equiv u_b = given \tag{2.31a}$$

$$Outflow\ \ B.C. \quad : \quad u_W \equiv u_b = u_P \quad (zero\ \ gradient) \tag{2.31b}$$

2.3.1.1 Two–point schemes: first–order upwind or central difference

If the scheme used for the internal control volumes is either first–order upwind or central difference, then the situation for the left border control volume, shown in Fig. 2.6, is no different than any internal control volume. Thus, the coefficients A_P, A_W, A_E, etc. are defined in the usual manner as given by Eqs. (2.7) or (2.10). Such a treatment has the same local order of accuracy as the internal scheme and the flux across these control volume interfaces are consistent.

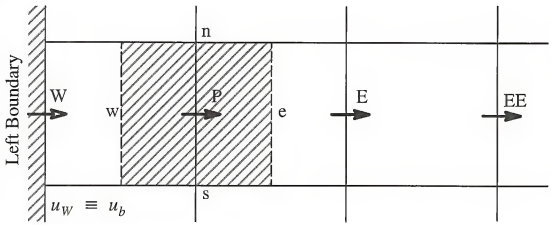

Fig 2.6. A typical left–border u–control volume.

2.3.1.2 Second–order upwind scheme

The situation is different when the second–order upwind scheme is used for the internal control volumes. For example, the point P, shown in Fig. 2.6, has only one neighbor (namely W) to its left and if the flux F_w is coming in from the boundary, we can only use a scheme that involves only one neighbor, such as the first–order upwind or the central difference scheme, to estimate the value of ϕ_w. If the flux F_w is coming towards the west face from the interior of the domain, we can use the second–order upwind scheme. As far as the east face of the control volume is concerned, we are free to estimate ϕ_e using the same scheme as that for the west face or the second–order upwind scheme, since the east face has two upwind neighbors in either direction. These two options are discussed next.

Option I: cell–based.

For the control volume shown in Fig. 2.6, the first option is to use either the first–order upwind or the central difference scheme for both east and west faces. This means that for the control volume in question, the convection flux treatment will be either first– or second–order accurate locally, depending on whether we use the first–order upwind or the

second–order central difference scheme. However, the flux at the east face of the control volume (marked 'e' in Fig. 2.6) will not be consistent in the sense that the flux calculated at that face for the current control volume will not equal the flux calculated at the same face belonging to the control volume immediately to the right of the current control volume (i.e., the control volume corresponding to the point E in Fig. 2.6, for which we use second–order upwind scheme for both the faces). However, since the numerical procedure is cell–based, the fluxes estimated from two different cells across the common face do not cause explicit inconsistency in formulation. For the second–order upwind scheme, since the derivation of the coefficients entails the same steps as for the first–order upwind and second–order central difference, the coefficients for the left–border control volumes, using option I, are the same as those given by Eqs. (2.7) and (2.10) for first–order upwind and second–order central difference schemes, respectively.

Option II: face–based.

East face. To eliminate the inconsistency in the estimation of the flux at the east face of the left border control volume, as discussed above, we can use second–order upwind scheme at that face, since two neighbors are available for the east face in both the directions (namely, P and W to its left, and E and EE to its right):

$$F_e u_e = \left(\frac{3}{2}u_P - \frac{1}{2}u_W\right) [\![F_e, 0]\!] - \left(\frac{3}{2}u_E - \frac{1}{2}u_{EE}\right) [\![-F_e, 0]\!] \tag{2.32}$$

West face with $F_w < 0$. The west face can have different treatments depending on the direction of the flux F_w. If the flux F_w is negative, i.e., if the local upwind direction is to the left, we can use second–order upwinding for the west face because two neighbors (P and E) are available. In such a situation, we obtain a second–order accurate scheme for the left border control volume. Thus, if $F_w < 0$, we use second–order upwinding, i.e.,

$$F_w u_w = F_w\left(\frac{3}{2}u_P - \frac{1}{2}u_E\right) \tag{2.33a}$$

To take into account that above holds only for $F_w < 0$, we can write

$$F_w u_w = -\left(\frac{3}{2}u_P - \frac{1}{2}u_E\right)[\![-F_w, 0]\!] \tag{2.33b}$$

Thus, when $F_w < 0$, we maintain second–order local accuracy as well as consistency across the control volume interfaces.

<u>West face with $F_w > 0$</u> If the local upwind direction is to the right, i.e., the flux F_w is coming in from the boundary, then we have to use the first–order upwind or the second–order central difference estimation for u_w. Such a situation in which we use second–order upwinding on the east face and first–order upwinding or second–order central differencing on the west face of the control volume gives rise to a deterioration in the formal order of local accuracy of the flux estimation, as can be seen from a Taylor series expansion, to be presented later. If $F_w > 0$, then we use either first–order upwind or central difference scheme to estimate u_w:

$$First - Order\ Upwind \quad : \quad F_w u_w = F_w u_b \tag{2.34a}$$

$$Central\ Difference \quad : \quad F_w u_w = F_w \frac{1}{2}\left(u_P + u_b\right) \tag{2.34b}$$

which, taking into account that it holds only for $F_w > 0$, can be written as

$$First - Order\ Upwind \quad : \quad u_w = u_b\ [\![F_w, 0]\!] \tag{2.35a}$$

$$Central\ Difference \quad : \quad F_w u_w = \frac{1}{2}\left(u_P + u_b\right)[\![F_w, 0]\!] \tag{2.35b}$$

<u>If we use first–order upwinding for the west face when $F_w > 0$</u>, namely Eq. (2.35a), then the flux at the east face is again given by Eq. (2.32) and that at the west face is given by

$$F_w u_w = u_W[\![F_w, 0]\!] - \left(\frac{3}{2}u_P - \frac{1}{2}u_E\right)[\![-F_w, 0]\!] \tag{2.36}$$

Now, following a similar procedure as for the internal control volumes, we obtain the same coefficients as for the first–order upwind scheme, i.e., those given by Eq. (2.7), with the following form for the source term b:

$$b = -\frac{1}{2}(u_P - u_W)[\![F_e, 0]\!] + \frac{1}{2}(u_E - u_{EE})[\![-F_e, 0]\!] + \frac{1}{2}(u_P - u_E)[\![-F_w, 0]\!] \tag{2.37}$$

For this case, i.e, Option II with first–order upwinding at the east face if the flux is coming in from the boundary, if we assume that $F_w > 0$ and $F_e > 0$ and do a Taylor series expansion of the terms about the point P, we get

$$\frac{\partial(u_P u_P)}{\partial x} = \frac{5}{2}u_P u_P' + h\left[-\frac{3}{4}u_P u_P'' - \frac{1}{2}u_P' u_P'\right] + \ldots \tag{2.38}$$

This indicates that across the control volume in question, the overall scheme is not even first–order accurate !

<u>If we use central differencing for the west face when $F_w > 0$,</u> namely Eq. (2.35b), then the flux at the east face is again given by Eq. (2.32) and that at the west face is given by

$$F_w u_w = \frac{1}{2}(u_P + u_W)[\![F_w, 0]\!] - \left(\frac{3}{2}u_P - \frac{1}{2}u_E\right)[\![-F_w, 0]\!] \tag{2.39}$$

If we use central differencing on the west face if $F_w > 0$, then we have the following

$$\begin{aligned} A_E &= D_e + [\![-F_e, 0]\!] \\ A_W &= D_w + \frac{1}{2}[\![F_w, 0]\!] \\ A_p &= A_E + A_W \end{aligned} \tag{2.40}$$

and the form of b is the same as that in Eq. (2.37). Note that Eq. (2.37) for b differs from Eq. (2.21) for internal control volumes only in the third term on the right hand side which is absent in Equation (2.37) for the left border control volumes. Doing a Taylor series analysis of this case, similar to the previous case, we get

$$\frac{\partial(u_P u_P)}{\partial x} = 2u_P u_P' - \frac{h}{2}u_P u_P'' + h^2\left[\frac{5}{24}u_P u_P''' + \frac{1}{8}u_P' u_P''\right] + \ldots \tag{2.41}$$

which indicates that the overall scheme is one order less accurate in the left border control volumes than in the internal control volumes.

2.3.1.3 The QUICK scheme

The situation for the QUICK scheme is similar to the second–order upwind scheme and we can use the same two options described above. In this section we will provide the expressions for the coefficients resulting from these options, for the QUICK scheme.

Option I

For the QUICK scheme, the coefficients resulting from the use of Option I are exactly the same as those for the second–order upwind scheme, namely those given by Eqs. (2.7) and (2.10), depending on whether we use first–order upwinding or central differencing on the west face when $F_w > 0$.

Option II

Similar to the second–order upwind case, if we employ a first–order upwind scheme at the west face when $F_w > 0$, we obtain the same coefficients as for the first–order upwind scheme, i.e., those given by Eq. (2.7), with the following form for the source term b:

$$b = -\left(-\frac{1}{8}\phi_P - \frac{1}{4}\phi_W + \frac{3}{8}\phi_E\right)[\![F_e, 0]\!] + \left(\frac{3}{8}\phi_P - \frac{1}{4}\phi_E - \frac{1}{8}\phi_{EE}\right)[\![-F_e, 0]\!]$$
$$+ \left(\frac{3}{8}\phi_W - \frac{1}{4}\phi_P - \frac{1}{8}\phi_E\right)[\![-F_w, 0]\!] \qquad (2.42)$$

If we use central differencing on the west face when $F_w > 0$, we obtain the same coefficients as for the second–order upwind scheme given by Eq. (2.40), with the source term b given by Eq. (2.42) given above.

2.3.2 Bottom Border Control Volumes

The situation is slightly different for the top and bottom border control volumes shown in Fig. 2.1; a typical control volume on the bottom border is shown in Fig. 2.7. The interface nearest to the boundary of the domain lies on the boundary itself. Thus, both components of velocity at this interface are known according to the specified boundary condition:

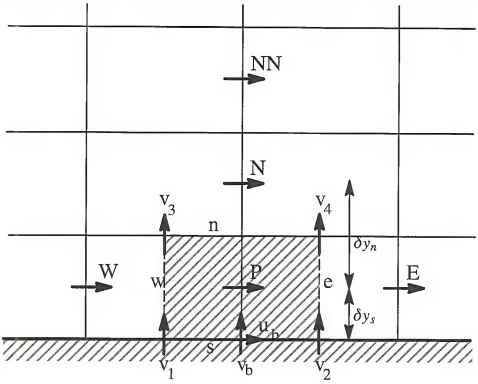

Fig. 2.7. A typical bottom–border u–control volume.

$$\textit{Dirichlet B.C.} \quad : \quad \begin{aligned} u_S &\equiv u_b = given \\ v_b &= 0.5(v_1 + v_2) = given \end{aligned} \tag{2.43a}$$

$$\textit{Outflow B.C.} \quad : \quad \begin{aligned} u_S &\equiv u_b = u_P \quad (zero\ gradient) \\ v_b &= 0.5(v_3 + v_4) \quad (zero\ gradient) \end{aligned} \tag{2.43b}$$

Since the velocities are specified at the south interface directly, as shown in Fig. 2.7, no interpolation or extrapolation is required to estimate them at this interface. The discretized equation (2.2a) still holds but we need to substitute the coefficient D_s with $D_s{}^*$,which is given by

$$D_s^* = \frac{\mu_s\ h}{0.5\ k} \tag{2.44}$$

Note the additional factor 0.5 in Eq. (2.44) which reflects the fact that the south neighbor is only a half control volume height away from the point P instead of the usual full height, i.e.,

$$(\delta y_s)_{south\ border\ C.V.} = \frac{1}{2}(\delta y_s)_{internal\ C.V.} \tag{2.45}$$

This amounts to using a first–order one–sided differencing to approximate the gradient, resulting in a reduction of "local" order of accuracy by one, for the diffusion term. Also, at the south face, the convective flux is given by

$$F_s^* = \varrho_s v_b \tag{2.46}$$

2.3.2.1 Internal scheme: first–order upwind

Using Eq. (2.2a) and subtracting the continuity equation (2.2b) multiplied by u_P, for the first–order upwind scheme, we get

$$\begin{aligned} A_N &= D_n + [\![-F_n, 0]\!] \\ A_S &= D_s^* + F_s^* \\ A_P &= A_N + A_S \end{aligned} \tag{2.47}$$

2.3.2.2 Internal scheme: central difference

Using Eq. (2.2a) and subtracting the continuity equation (2.2b) multiplied by u_P, for the central difference scheme applied to a bottom border control volume, we get:

$$\begin{aligned} A_N &= D_n - \frac{F_n}{2} \\ A_S &= D_s^* + F_s^* \\ A_P &= A_N + A_S \end{aligned} \tag{2.48}$$

2.3.2.3 Internal scheme: second–order upwind scheme

We have two options to treat the north and the south interfaces of the bottom border control volumes, similar to the left border discussed earlier.

Option I

The first option is to use the first–order upwind or the central difference scheme for both the faces of the control volume, for which we get the same coefficients as for the

first–order upwind or second–order central difference schemes given by Eqs. (2.7) and (2.10), respectively.

Option II

As discussed earlier, for Option II, we use second–order upwinding for the north face which gives

$$F_n u_n = (2u_P - u_S)[\![F_n, 0]\!] - \left(\frac{3}{2}u_N - \frac{1}{2}u_{NN}\right) [\![- F_n, 0]\!] \tag{2.49}$$

Note that the first term on the right hand side of Eq. (2.49) uses different factors than the second term because of Eq. (2.45). For the south face, we use Eq. (2.46), irrespective of the sign of the flux F_s, since the south face lies on the boundary itself. Thus, at the bottom border, for the second–order upwind scheme with Option II, we have:

$$\begin{aligned} A_N &= D_n + [\![- F_n, 0]\!] \\ A_S &= D_s^* + F_s^* \\ A_P &= A_N + A_S \\ b &= -(\phi_P - \phi_S)[\![F_n, 0]\!] + \frac{1}{2}(\phi_N - \phi_{NN})[\![- F_n, 0]\!] \end{aligned} \tag{2.50}$$

Note the missing factor of 1/2 in front of the first term in the expression for b above which is due to Eq. (2.45). Also note the absence of any contribution to b from the flux on the south face, since the south face lies on the boundary.

It should be mentioned here that a treatment similar to above has to be imparted to the south face of control volumes for u–velocity associated with j=3 grid line if $F_s>0$ and to the north face of control volumes associated with j=nj–2 grid line if $F_n<0$, due to equations similar to Eq. (2.45). The coefficients for these control volumes thus get modified accordingly but we will not present them here.

2.3.2.4 Internal scheme: QUICK

Option I

The coefficients are the same as that for the second–order upwind case, namely, those given by Eqs. (2.7) and (2.10).

Option II

For the north face, the situation is the same as any internal control volume if $F_n<0$, but if $F_n>0$, then Eq. (2.45) leads to a slightly different interpolation formula for the evaluation of u_n ,which now becomes

$$u_n = \frac{1}{3}u_N - \frac{1}{3}u_S + u_P \quad , \qquad \text{if } F_n > 0 \ . \tag{2.51}$$

The coefficients A_N, A_S and A_P are the same as for the second–order upwind case, namely those given by Eq. (2.50), with the following source term:

$$b = -\left(-\frac{1}{3}\phi_S + \frac{1}{3}\phi_N\right)[\![F_n, 0]\!] + \left(\frac{3}{8}\phi_P - \frac{1}{4}\phi_N - \frac{1}{8}\phi_{NN}\right)[\![-F_n, 0]\!] \tag{2.52}$$

Note that analogous to the second–order upwind boundary treatment with option II, the first term on the right hand side of the expression for b has different expressions than for an internal control volume due to Eq. (2.45). Also note the absence of any contribution from the flux on the south face since it lies on the boundary, as discussed earlier. Similar to the second–order upwind case, a treatment similar to Eq. (2.51) has to be imparted to the south face of control volumes for u–velocity associated with j=3 grid line if $F_s > 0$ and to the north face of control volumes associated with j=nj–2 grid line if $F_n < 0$, due to equations similar to Eq. (2.45). The coefficients thus get modified accordingly but we will not present them here.

2.3.3 Summary of the Boundary Treatments

We present here the essence of the various boundary treatments detailed above. The shear stress terms generally need to be approximated by the first–order one–sided

differencing instead of the standard second–order central difference scheme. As to convection terms, the treatment of the border control volumes for two–point schemes, such as the first–order upwind and the second–order central difference schemes, is no different from the internal control volumes, except for the interfaces lying on the boundary for which no interpolation or extrapolation is required (we use the values specified by the boundary condition there). For schemes with a larger stencil, such as the second–order upwind and QUICK schemes, the coefficients for the border control volumes can be formulated using two options. The first option, labelled Option I, involves an application of a two–point scheme across both the interfaces and is thus consistent within these control volumes in the sense that "local" order of accuracy is the same as that of the two–point scheme employed. However, using Option I does not maintain the consistency of the flux across the interior face of the border control volumes, between the border control volumes and their immediate neighbors on the downwind side. The second option, labelled Option II, remedies this situation by using the same scheme as for the internal control volumes (namely, second–order upwind or QUICK) for the interior face of the border control volumes. But, now the "local" order of accuracy, as far as the border control volumes are concerned, deteriorates. However, in general, the "global" order of accuracy of the solution does not deteriorate by this reduction of "local" accuracy. In the next section, we discuss the performance of the various convection schemes and the effect of the different boundary treatments on overall solution accuracy.

2.4 Results of the Test Case

The standard lid–driven cavity flow problem is chosen as a test case, in order to evaluate the performance of the various convection schemes, along with the different boundary treatments discussed above. The problem consists of a square cavity bounded by solid stationary walls on all sides, except the top wall which is replaced by a lid moving at a constant velocity, thus inducing a recirculating flow in the cavity. The flow field contains

a primary recirculation region whose extent of penetration into the cavity is dictated by the Reynolds number of the flow which is based on the length and the velocity of the moving lid. Secondary recirculation regions also exist near the corners of the cavity. This problem has been extensively used to assess various codes and schemes by several researchers, and serves as a useful test bed owing to substantial skewness of the streamlines of the flow relative to the grid employed for numerical simulation.

2.4.1 Overall Accuracy

In this section, we present the results in two parts. In the first part, we assess the relative merits of non–conservative (Scheme A) and conservative (Scheme B) implementations of the second–order upwind scheme. A direct comparison with the central difference scheme is also presented by performing computations of the driven cavity flow on four successively refined grids for four Reynolds numbers. In the second part of this section, we evaluate the four convection schemes formulated earlier– –the first–order upwind, central difference, second–order upwind and the QUICK schemes– –by comparing results obtained on a 21x21 grid for Reynolds number of 1000.

2.4.1.1 Assessment of central difference and the two second–order upwind schemes

Four Reynolds numbers are studied, namely, 100, 400, 1000 and 3200. Four different uniform meshes are used for the numerical calculation, consisting of 21x21, 41x41, 81x81 and 161x161 uniformly distributed grid points. The well–known results of Ghia *et al.* (1982) have been used as a benchmark to assess the relative performance of these schemes. Ghia *et al.* have employed the central difference scheme in the streamfunction–vorticity formulation on a 129x129 grid to obtain a grid independent solution. The u–velocity profiles at the centerline of the cavity (x=0.5) obtained by using different schemes have been compared. In the following, results obtained by using the second–order central difference scheme are presented and discussed first. The solutions obtained by using the two second–order upwind schemes will then follow.

For the present problem, the central difference operator for the convection term is seen to yield good results. Fig. 2.8 shows that there is a monotonic trend of improvement in numerical accuracy yielded by the second–order central difference scheme. The degradation of numerical accuracy of solutions with the same number of grid points increases as the Reynolds number increases. With the Reynolds number, defined as

$$\mathrm{Re} = \frac{uL}{\nu} \tag{2.53}$$

of 100, a 21 x 21 grid is sufficient for obtaining a grid–independent solution. For Re of 400, however, at least an 81 x 81 grid is needed. For Re of greater than 1000, more than 161 x 161 nodes are required before the solutions can be deemed as very accurate. Overall, it is interesting to observe that for the driven cavity flow, the second–order central difference scheme seems to be very robust; it not only can yield convergent solutions in a numerically stable manner, but also exhibits no numerical oscillations, as demonstrated in Fig. 2.8. More information of the behavior of the central difference scheme can be revealed from the contour plots of the cell Reynolds numbers. The cell Reynolds number represents the relative ratio of the modelled convection and diffusion terms and is given by

$$R_{\Delta u} = \frac{\Delta u \;\; k}{\nu} \; . \tag{2.54}$$

It should be pointed out here that we have chosen to define the cell Reynolds number based on the local velocity variation rather than the local velocity itself. This definition, as suggested by Cheng and Shubin (1978), is more representative of the computational resolution since it is based on the velocity variation across a finite volume. The appropriateness of this definition can be better illustrated for the linear convection–diffusion equation where regardless of how high the Reynolds number is, no difficulty in numerical computation appears unless solution gradients are large enough. Hence a cell Reynolds number based on the absolute velocity (which can be arbitrarily adjusted via a change of coordinate) is not always indicative.

As already mentioned, it is well known that for the steady–state, linear Burgers equation, the critical cell Reynolds number beyond which wiggles are seen in the solution, is

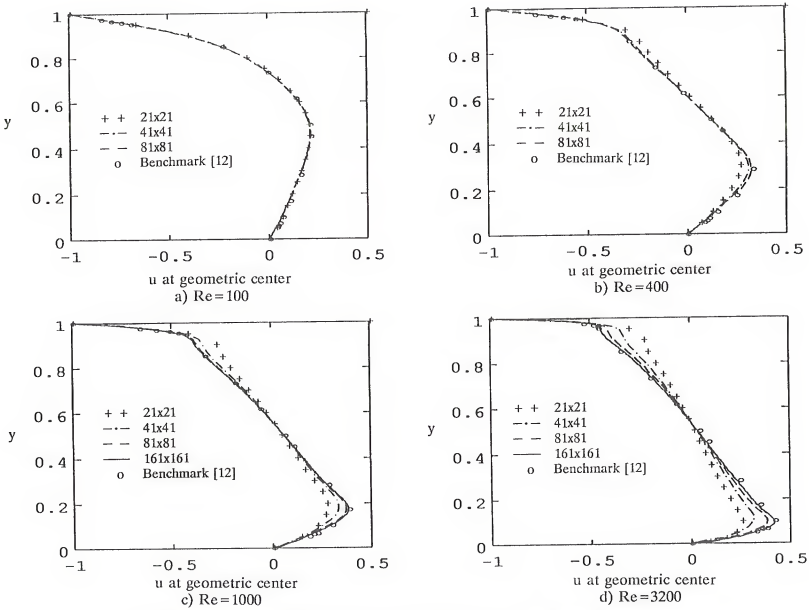

a) Re=100 b) Re=400 c) Re=1000 d) Re=3200

Fig. 2.8. u–velocity profiles using the second–order central difference scheme.

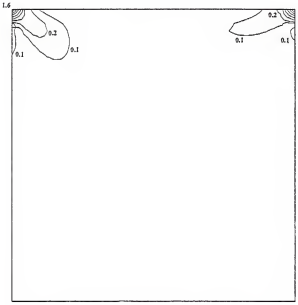

a) Re = 100

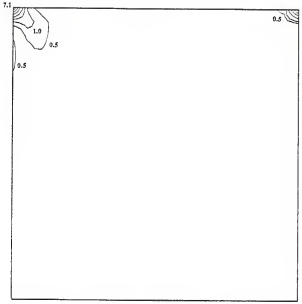

b) Re = 400

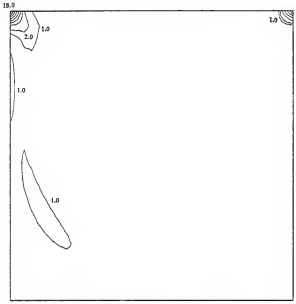

c) Re = 1000

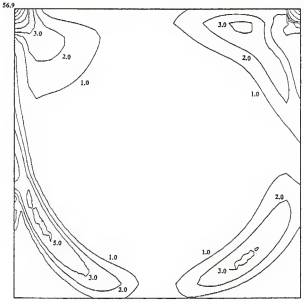

d) Re = 3200

Fig. 2.9. Cell Reynolds number contours using the central difference scheme on the 41x41 grid.

2. Fig. 2.9 depicts the cell Reynolds number contours of the u–velocity components of four flows on the 41 x 41 grid. It can be seen from Fig. 2.9 that the majority of the flowfield has modest values of cell Reynolds number. Thus for most of the flow domain the magnitudes of the convection and diffusion terms are of the same order. However, the regions of large cell Reynolds number do exist and they grow in sizes as Re increases. The case of Re=3200, Fig. 2.9(d), clearly shows that the regions of large cell Reynolds numbers coincide with the top corners as well as the boundary surrounding the primary eddy. Figs. 2.8 and 2.9 illustrate an interesting point. Based on the aforementioned linear analysis, it is generally accepted that there exists a critical limit of the cell Reynolds number when using the second–order scheme. It has been suggested by Gresho and Lee (1981) that this characteristic can be used to indicate the regions that need further mesh refinement, i.e., when there are wiggles exhibited by the solutions of the second–order central difference scheme, one knows there is a need to refine the grid distribution. However, Figs. 2.8 and 2.9 demonstrate that the notion of a critical cell Reynolds number for the central difference scheme may not be reliable; they clearly show that the solutions on a coarse grid can be wiggle free and yet far from accurate.

Figs. 2.10 and 2.11 show the solutions yielded by the two second–order upwind schemes. Both quantitatively and qualitatively, Scheme A does not behave the same as Scheme B. For Scheme A, it seems that while the accuracy of the solutions generally improves as the grid is refined, within the range of the finite spatial resolution used here, noticable errors exist for all Reynolds numbers. This phenomenon is similar to that reported by Vanka (1987) based on a different implementation. Nevertheless, in this study, unlike that in Vanka (1987), no numerical stability problems have been encountered.

The solutions of Schemes B, shown in Fig. 2.11, are much more satisfactory. Not only are the solutions more closely agreeable to the benchmark results but also appear to require fewer number of grid points than either Scheme A or the second–order central difference scheme to yield good accuracy. Scheme B conforms to the idea of a control volume formulation. For 41 x 41 nodes, Scheme B can yield quite satisfactory solutions for the

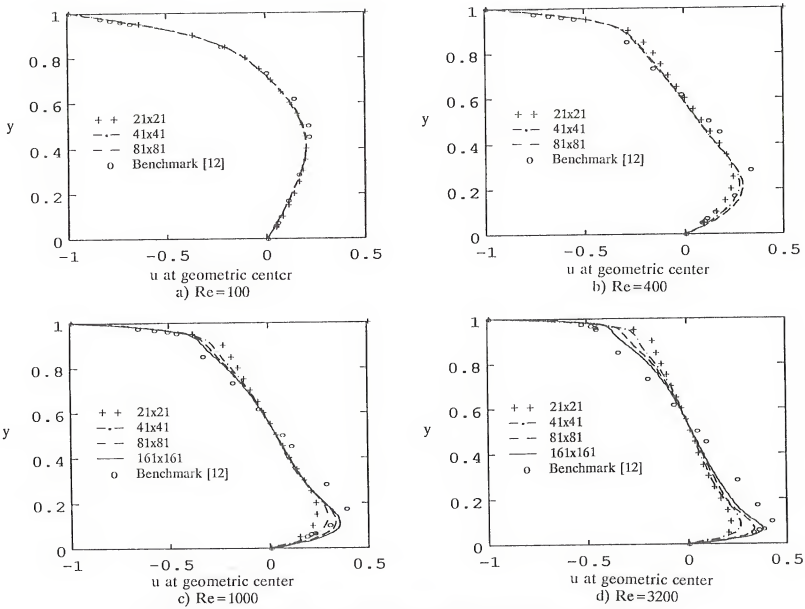

Fig. 2.10. u–velocity profiles using the second–order upwind scheme, Scheme A.

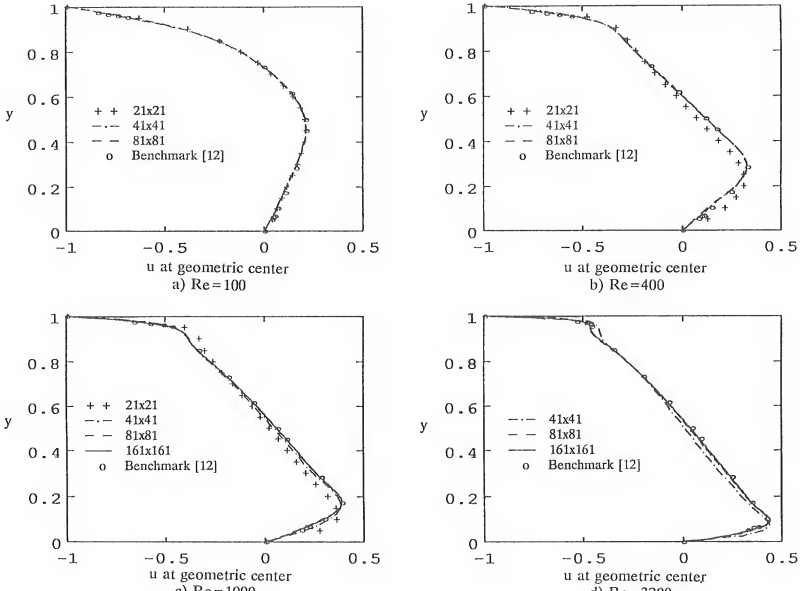

Fig. 2.11. u–velocity profiles using the second–order upwind scheme, Scheme B.

u–velocity profile along a vertical line through the center of the cavity, for all Reynolds numbers studied.

It should be noted that although the comparisons presented in Figs. 2.8, 2.10 and 2.11 (along x = 0.5) are standard, they may not be the most critical ones as far as the true accuracy of a scheme is concerned. This is due to the fact that, as demonstrated in Fig. 2.9, the central vertical line of the cavity is a location that is consistently of smaller cell Reynolds numbers; hence the solutions of u–velocity profile along this line may be more accurate than at other places. Figure 2.12 compares the u–velocity profiles along the horizontal line y=0.25, drawn at 0.25 times the overall cavity height from the bottom wall with different Reynolds numbers and schemes. Although the relative performance of the schemes with respect to the Reynolds number and the grid density remains the same, Fig. 2.12 shows that the numerical accuracies of the predicted u–velocity profile are generally worse along y=0.25 than along x=0.5. Figs. 2.12(c) and (d) show that Scheme B yields more satisfactory results than the other schemes along the line y=0.25 in the sense that the velocity profiles seem to converge to the same solution as the grid density is increased, i.e., the velocity profiles on the 81x81 and 161x161 grids are very close to each other, whereas no such observation can be made for the other schemes.

As already mentioned, Schemes A and B are formally of second order accuracy. The differences of their numerical accuracy can not be explained in terms of leading terms of the local truncation error analysis. It appears that the degrees of agreement of these schemes to the finite volume formulation are more influential. This can also explain why the second–order upwind scheme used by Vanka (1987) is not very satisfactory either. In view of the very confined regions of high cell Reynolds number, it is possible that large gradients (and singularity) caused by the corners (Ghia *et al.* 1982) may be responsible for unsatisfactory performance of the schemes not expressed in conservative form. The other point worth noting is that the use of the first–order upwind scheme at some nodes close to the boundary is not all that critical to the overall numerical accuracy; this fact is clearly demonstrated by the cell Reynolds number distribution shown in Fig. 2.9. Finally, a

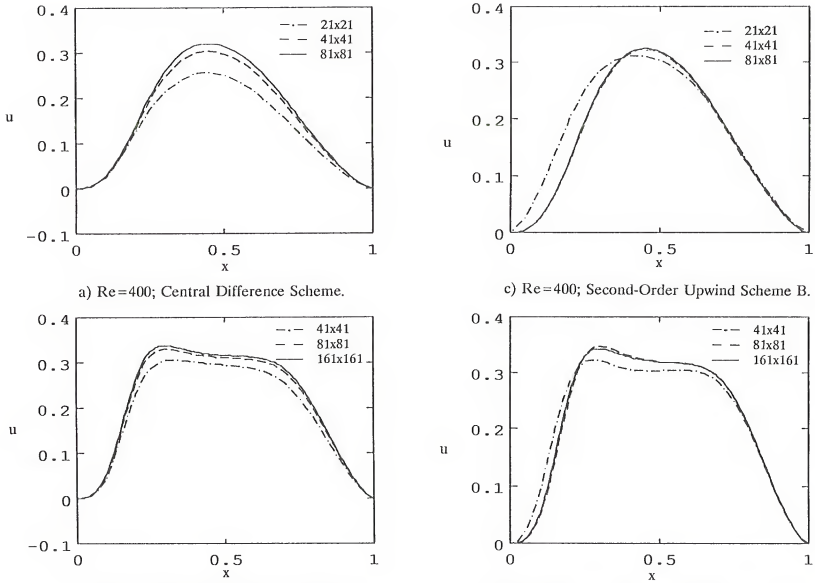

a) Re=400; Central Difference Scheme.

c) Re=400; Second-Order Upwind Scheme B.

b) Re=1000; Central Difference Scheme.

d) Re=1000; Second-Order Upwind Scheme B.

Fig. 2.12. u–velocity profiles along the horizontal line at y=0.25 in the driven cavity.

comment regarding the issue of numerical dissipation is in order. As is known, numerical damping is often responsible for stabilizing the computational procedure and smearing the solution profile, causing reduced accuracy. Shyy (1985a) has shown that the second–order upwind scheme can be considered as a combined form of both the second and fourth order central difference schemes with some added numerical damping. The results shown here demonstrate that with numerical damping (relative to the central difference schemes), the solution obtained by a second–order scheme can still be better than that obtained by the central difference scheme, even though the latter can yield wiggle–free solution.

2.4.1.2 Comparison of various schemes on the 21x21 grid

The streamline contours obtained for Reynolds number 1000 on a 21x21 grid, using the four convection schemes––first–order upwind, central difference, second–order upwind and QUICK––are plotted in Fig. 2.13. In Fig. 2.14, the u–velocity profiles along the vertical centerline of the cavity, using the four schemes on the 21x21 grid are plotted. The results shown in Figs. 2.13 and 2.14 have been obtained using Option I with first–order upwinding for all the boundary control volumes, in order to have a common basis for comparison of the four schemes, without the interference of varying boundary treatments for the different schemes. As is well known, the first–order upwind scheme has an excessive amount of numerical diffusion inherent to it, which is evident from the maximum value of the streamfunctions for this scheme compared to the other three schemes, shown in Fig. 2.13, and also from the u–velocity profiles on the 21x21 grid, shown in Fig. 2.14. The central difference yields satisfactory results for this problem, though some nonphysical kinks can be observed in the streamfunction contours, especially near the top right corner of the cavity. These regions in the flowfield correspond to regions of cell Reynolds numbers larger than 2, as has been shown in Fig. 2.9. In the majority of the flow domain, however, the cell Peclet numbers are less than 2, thus leading to the satisfactory performance of the central difference scheme. We will not evaluate the first–order upwind and the central difference schemes any further, since much has already been said about them in the literature. Our main focus here

is on the two higher–order upwinding schemes, namely, the second–order upwind and QUICK schemes.

Owing to the higher formal order of accuracy of the second–order upwind and QUICK schemes, resulting from the higher–order upwind extrapolation and interpolation, respectively, employed by these schemes, one expects better overall performance from these schemes compared to the first–order upwind scheme, in terms of numerical diffusion. This is indeed the case in the present problem, as can be seen from Fig. 2.13 by the relative magnitudes of the streamfunction values as well as the u–velocity profiles along the centerline of the cavity, plotted in Fig. 2.14, for the 21x21 grid. This is especially true for the second–order upwind scheme which gives the least diffusive solution profile on the 21x21 grid. As seen from Fig. 2.13, the maximum streamfunction value on the 21x21 grid obtained by the second–order upwind scheme (0.103) is higher compared to the other schemes (Ghia *et al.* (1982) obtained a maximum value 0.1175 on a 129x129 grid). Similarly, the u–velocity profile obtained by the second–order upwind scheme on the 21x21 grid, as seen from Fig. 2.14, is in closest agreement with the benchmark results. The QUICK scheme, on the other hand, yields results very close to that for the central difference scheme, as seen from the streamfunction values in Fig. 2.13 and the u–velocity profiles in Fig. 2.14, for the 21x21 grid, and appears to be not as accurate as the second–order upwind scheme. However, the localized nonphysical kinks observed with the central difference scheme are not observed with both of these higher–order upwind schemes, even though the critical cell Peclet number for the model linear one–dimensional Burgers equation using the QUICK scheme is 8/3, as shown by Shyy (1985), which is only slightly larger than that for the central difference scheme. (It should be noted that the exact value of the corresponding critical cell Peclet number for the system of Navier–Stokes equations is not known.) Both second–order upwind and QUICK schemes exhibit quite satisfactory performance and yield a virtually grid independent solution for the 81x81 grid. As shown in Fig. 2.8, a 161x161 grid is required to obtain a solution of comparable accuracy with the central difference scheme. In this

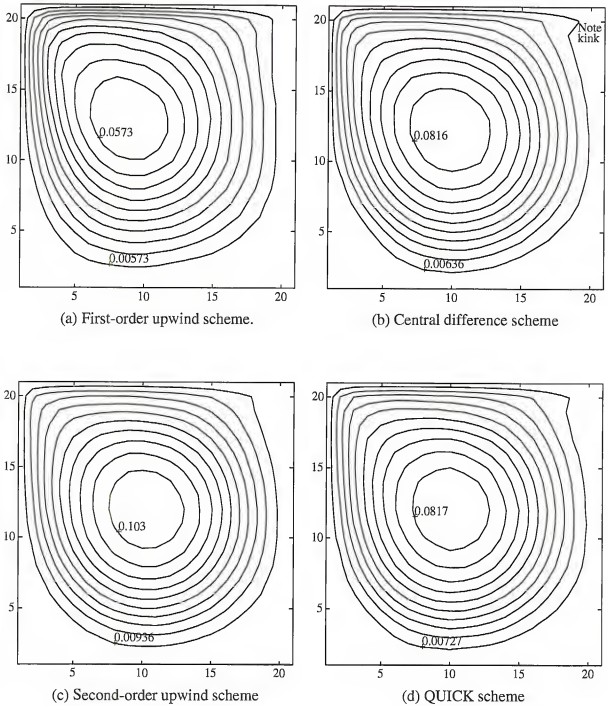

(a) First-order upwind scheme.

(b) Central difference scheme

(c) Second-order upwind scheme

(d) QUICK scheme

Fig. 2.13. Streamfunction contours on the 21x21 grid for various convection schemes.

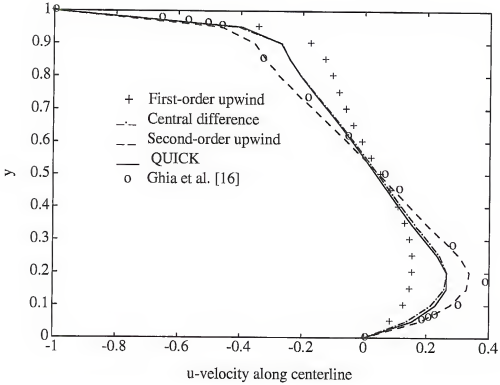

Fig. 2.14. u–velocity profiles along the centerline of the cavity using various schemes.

respect also, the second–order upwind and QUICK schemes perform better than the central difference scheme. Moreover, for flows with high Reynolds number and high cell Peclet numbers in the majority of the flow domain, the central difference scheme is known to either be numerically unstable or yield substantial wiggles in the solution profiles. One expects the second–order upwind and QUICK schemes to perform better in this regard, too, for more complex flows.

2.4.2 Stability And Convergence

The convergence path of the residuals associated with the u–momentum equation for the entire flow field using the 21x21 grid, for all four schemes, including both the versions of second–order upwind and QUICK schemes are plotted in Fig. 2.15. The second–order upwind and QUICK schemes take a larger amount of CPU time compared to the first–order

upwind and central difference schemes, due not only to more number of iterations required by these schemes to achieve the same level of convergence, but also to more time needed to compute the more complex coefficients associated with them. However, this drawback is more than offset by the superior performance of these schemes, even on a coarse grid like the 21x21 grid employed here for the cavity flow.

Versions 1 of the second–order upwind and QUICK schemes are designed with the objective of achieving better numerical stability and faster convergence rate, by enforcing diagonal dominance in the coefficient matrix. This is indeed achieved for the second–order upwind scheme as seen from Fig. 2.15, which shows that version 1 of this scheme converges faster than version 2. However, version 1 of the QUICK scheme converges slower than version 2. The same trend is seen for the 41x41 grid. This would seem to indicate that for the QUICK scheme, version 2, which does not enforce diagonal dominance, is more

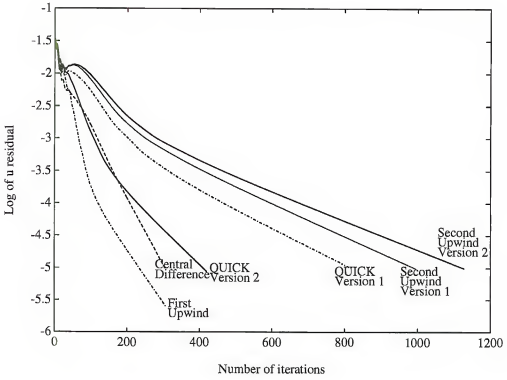

Fig. 2.15. Convergence history of u residuals on the 21x21 grid for various schemes.

desirable from the point of view of convergence rate. However, as we refine the grid any further (say, to 51x51 grid points), version 2 of the QUICK scheme becomes completely unstable and does not yield convergence. Moreover, the residuals diverge to machine limits very quickly, usually in two iterations, for moderate values of relaxation factors employed in the solution procedure. This very surprising behavior of the QUICK scheme for grids with more than 41x41 nodes for the cavity flow problem has also been observed by other authors (Han *et al.* 1981, Hayase *et al.* 1992). However, version 1 of the QUICK scheme, which maintains diagonal dominance in the coefficient matrix for the whole flow domain, is quite stable for all the grids employed in the present study – up to 161x161 nodes used for the present problem. This shows that version 1 of the QUICK scheme is more robust than version 2 and hence is the more desirable one. At this point, it may be recalled that both versions, if they converge, must do so to the same solution since they are different versions of the same basic formulation of the QUICK scheme.

On the other hand, for the second–order upwind scheme, both the versions are quite stable for all the cases studied in the present work. However, from the above mentioned experience with the QUICK scheme, one might expect version 1 of the second–order upwind scheme to be more robust and stable compared to version 2 for more complex flows.

2.4.3 Effect of Various Boundary Treatments

Having assessed the relative robustness of the two versions of second–order upwind and QUICK schemes, we now turn our attention to the relative effects of the various boundary treatments on the overall performance of these schemes. Fig. 2.16 shows the u–velocity profiles along the centerline of the cavity using 21x21, 41x41 and 81x81 grids and second–order upwind scheme along with Options I and II. It is observed that Option I, which employs a consistent two–point scheme across both the interfaces of the border control volumes, is more robust in terms of performance on the coarser grids, compared to Option II, which employs different schemes on the two interfaces. For example, the

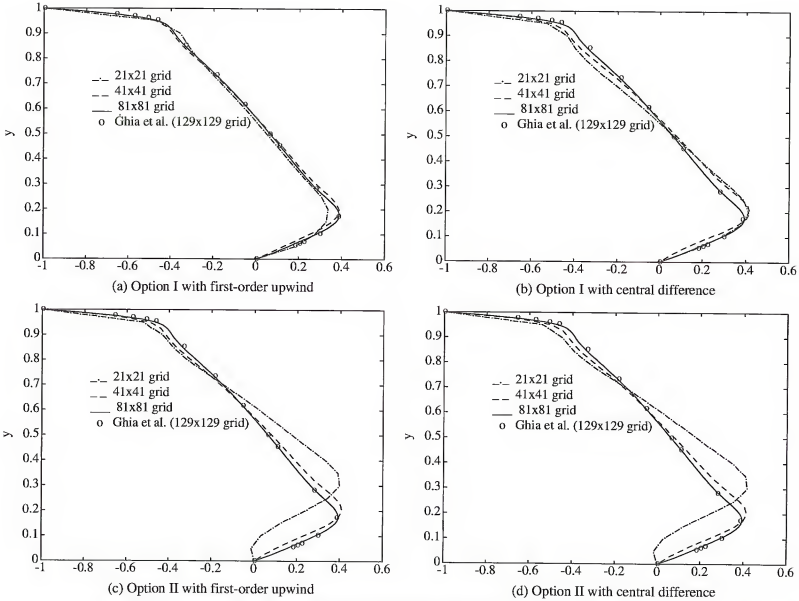

(a) Option I with first-order upwind

(b) Option I with central difference

(c) Option II with first-order upwind

(d) Option II with central difference

Fig. 2.16. u–velocity profiles using the second–order upwind scheme with different boundary treatments.

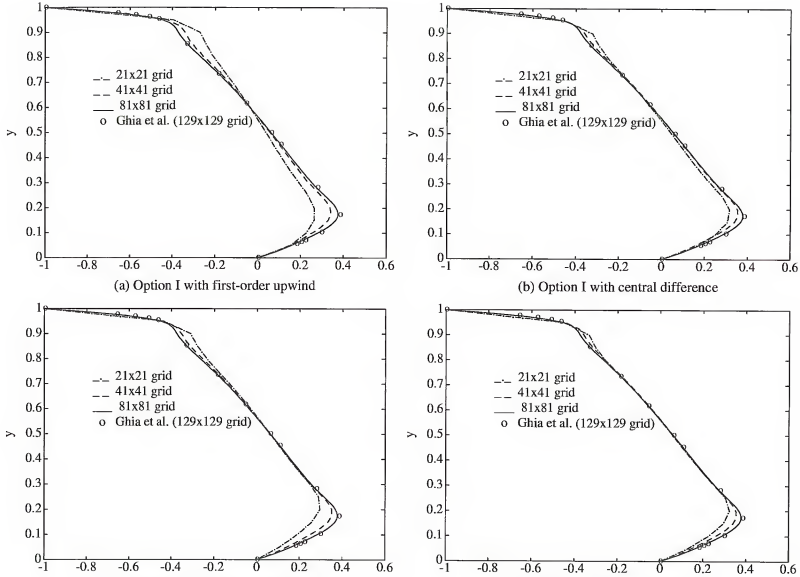

(a) Option I with first-order upwind

(b) Option I with central difference

(c) Option II with first-order upwind

(d) Option II with central difference

Fig. 2.17. u–velocity profiles using the QUICK scheme with boundary treatments.

u–profiles obtained using Option II on the 21x21 grid (Figs. 2.16 (c) and (d)) are qualitatively very different from the benchmark results as well as the profiles obtained om the same grids with Option I (Figs. 2.16 (a) and (b)). In fact, on these grids, Option II yields a nonphysical inflexion in the u–profile near the bottom boundary, exhibiting a negative value of u, for the 21x21 grid. Thus, the deterioration of local order of accuracy in the border control volumes with Option II seems to cause a substantial deterioration in the overall accuracy of the solution. The above observation holds for both first–order upwinding and central differencing with Option II, as seen in Figs. 2.16 (c) and (d). However, the trends of convergence towards a grid independent solution with first–order upwinding and central differencing for boundary treatment, for both Option I and II, are different. For first–order upwinding in the border control volumes, the solutions on the 21x21, 41x41 and 81x81 grids converge towards the benchmark profile from inside out, as seen in Figs. 2.16 (a) and (c). The use of central differencing, on the other hand, yields solutions on the same grids converging to the benchmark solution from outside in, as seen in Figs. 2.16 (b) and (d).

Contrary to the performance of the second–order upwind scheme, the QUICK scheme appears to be more robust with respect to variation of the boundary treatment. For both Option I and II, with both first–order upwinding and central differencing in the border control volumes, we observe very similar solution profiles an the 21x21 and 41x41 grids, converging to the grid independent solution profiles on the 81x81 grid, as seen from Fig. 2.17. Moreover, with both first–order upwinding and central differencing, the solution profiles on the successively refined grids converge to the benchmark solution from inside out.

2.5 Concluding Remarks

From the results obtained in this study, it can be said that a conservative and consistent formulation of a convection scheme is essential for achieving accuracy; this has been demonstrated here by studying non–conservative (Scheme A) and conservative

(Scheme B) implementations of the second–order upwind scheme. Even though the truncation error is of the same formal order for Schemes A and B, as seen from Taylor series analysis, Scheme B exhibits better performance. Thus, it is concluded that, in order to obtain satisfactory performance out of a scheme, it should be formulated in the spirit of the control volume formulation and should be strictly conservative. With regard to the performance of the central difference scheme for the driven cavity flow problem, no wiggles are observed for any of the Reynolds number cases studied, even though the cell Reynolds (or Peclet) number defined in a conventional manner (based on the velocity at the grid point) is more than 2 in several regions of the flowfield. This shows that the generally accepted concept of a critical cell Reynolds number beyond which the central difference scheme yields wiggles (which is strictly based on the analysis for linear Burgers equation) may not be a reliable indicator of the performance of the central difference scheme for general multidimensional flowfields. It has been shown here that a modified definition of cell Reynolds number (based on the velocity difference across the control volume) may be a better indicator of the relative strength of local convection and physical diffusion.

As for the comparison of the various convection schemes, the higher–order upwind schemes, namely, the second–order upwind and QUICK schemes perform better than the first–order upwind and central difference schemes. The increased computing time required by these schemes to achieve the same level of convergence is more than offset by the higher accuracy offered by these schemes. These schemes can converge to a grid independent solution for substantially fewer grid points compared to the first–order upwind and central difference schemes. As for the comparison between the second–order upwind and QUICK schemes, no universal claim can be made as to which one is better. For the problem studied here, the QUICK scheme is very sensitive to the formulation of the coefficients in the numerical algorithm. If diagonal dominance is not maintained, the QUICK scheme is very unstable, especially for large number of grid points. On the other hand, the second–order upwind scheme appears to be quite forgiving as far as its numerical implementation is

concerned– –it is observed to be stable with or without the maintenance of diagonal dominance in the coefficient matrix. However, the QUICK scheme seems to be less sensitive to variations in the boundary treatment. Second–order upwind scheme, on the other hand, shows substantially different behavior on relatively coarse grids for different boundary treatments. To summarize, while the QUICK scheme appears to be sensitive to its numerical implementation, the second–order upwind scheme appears to be sensitive to the consistency of the boundary treatment. With locally consistent boundary treatment (Option I) along with first–order upwinding, the performance of these two schemes is quite satisfactory, with the second–order upwind scheme yielding slightly better accuracy. Hence, one cannot unequivocally assert a universal superiority of one of these two schemes over the other. Moreover, all the above observations are based on the driven cavity flow problem studied here and may not hold identically for all fluid flow problems in general.

With regard to the boundary treatment, it appears that the cell–based treatment (labelled Option I) which employs a first–order upwind or central difference scheme consistently across both the faces of the border control volumes, is more robust compared to the face–based one (labelled Option II) which uses the higher–order upwinding for as many faces as possible. Also, from the numerical instability of the QUICK scheme and the slightly slower convergence rate for the second–order upwind scheme when diagonal dominance is not maintained, it appears that one should strive to formulate the schemes in a manner so as to achieve diagonal dominance if an iterative solver is used. Finally, while only a uniform grid is considered in the present study, formulas presented for the various schemes can be easily modified to account for a grid non–uniformity by utilizing the geometric interpretation discussed in the present work.

CHAPTER III
CONCEPTS OF TVD SCHEMES AND EXTENSION TO SEQUENTIAL SOLVERS

3.1. Background

Some conventional convection schemes, which are based on a geometrical interpretation of the fluxes on control volume interfaces, were studied in Chapter II. There the focus was on the performance of those schemes for convection–dominated, recirculating flows. In this chapter, we focus our attention on numerical schemes for resolving sharp gradients and discontinuities. The convection scheme to be developed in this chapter is based on a Total Variation Diminishing (TVD) scheme developed by Harten (1983) and can be interpreted broadly as consisting of the basic central difference flux augmented with an appropriate amount of nonlinear numerical dissipation.

To present the basic concepts of TVD schemes and to lay the foundation for extension of these schemes to multiple dimensions within the framework of the pressure–based sequential solver, we concentrate in this chapter on one–dimensional hyperbolic systems of equations. Conventional higher–order schemes (like the second–order central difference and Lax–Wendroff schemes) for hyperbolic systems of conservation laws are too dispersive, leading to spurious oscillations near sharp gradients. Moreover, some of these schemes may select a nonphysical solution. These problems can be overcome by using monotone conservative finite difference schemes which always converge and yield a physical weak solution satisfying an entropy inequality (Harten 1983, 1984). However, monotone schemes are only first–order accurate and are especially diffusive near discontinuities in the solution. A landmark development in the long quest for a satisfactory shock–capturing scheme was the introduction of the TVD concept (Harten 1983). The TVD schemes belong to a class of

monotonicity preserving schemes that possess the so–called total variation diminishing property, to be defined in the next section. These schemes are required to be total variation diminishing in the nonlinear scalar case and the constant coefficient system case and to be consistent with the conservation law and an entropy inequality. The first requirement ensures suppression of spurious oscillations and the second guarantees that the weak solutions are the physical ones (Harten 1983, 1984). The present chapter focuses its attention on TVD schemes. Before discussing the basic theory of TVD schemes, a summary of some of the several modern high resolution schemes is presented, in order to provide a feel for the enormous research activity in this area.

Overall, a multitude of strategies have been employed that have led to a wide variety of modern shock capturing schemes. These schemes can be broadly (and not very distinctively) classified into two approaches– –algebraic and geometric. The algebraic methods eliminate the spurious oscillations by limiting algebraic quantities such as the interface flux, whereas geometric approaches limit geometrical quantities like the slope of the dependent variables and/or their fluxes. The algebraic approaches include the two–step FCT schemes such as those by Boris & Book (1973), Boris *et al.* (1975) and Zalesak (1979) and several TVD schemes. For example, Harten has developed an explicit TVD scheme (1983) as well as a one–parameter family of implicit second–order accurate TVD schemes (1984). Yee *et al.* (1985) have examined the application of explicit and implicit second–order accurate TVD schemes to steady state calculations. Yee & Harten (1987) have also extended the TVD schemes to curvilinear coordinates. Some of the other TVD schemes include the second–order scheme of Roe–Sweby (Sweby 1984, Roe 1985, 1986), the symmetric TVD scheme of Yee–Roe–Davis (Davis 1984, Roe 1986, Yee 1987a), the one parameter family TVD scheme of Chakravarthy & Osher (1983) and the flux–splitting TVD scheme of Liou (1987). Many other studies have been conducted, e.g., Moretti (1987), Chang & Liou (1988) and Chen *et al.* (1989). The geometric methods include Godunov's first–order scheme developed by Godunov (1959) and also described by Sod (1983), its second–order accurate

extensions such as the MUSCL schemes of Van Leer (1979), Colella (1985), Davis (1988) and Goodman & LeVeque (1988), and the piecewise parabolic method (PPM) of Woodward & Colella (1984). Recently, a new class of geometric schemes called the Essentially Non–Oscillatory (ENO) schemes have been developed (Harten & Osher 1987, Harten *et al.* 1987, Harten 1989). Przekwas & Yang (1989) and LeVeque (1990) have summarized most of the modern shock–capturing schemes.

The conventional convection schemes, such as the central difference, upwind (both first– and second–order) and QUICK schemes, can be easily implemented in pressure–based algorithms, as documented in chapter II. On the other hand, the high resolution shock capturing schemes, notably TVD schemes, have so far been implemented effectively and reliably only in density–based simultaneous solvers (Yee & Warming 1985, Yee 1987b) which are commonly employed for compressible flows. For these simultaneous solvers, the TVD schemes can be implemented in a relatively straightforward manner via a similarity transformation applied to the system of equations whose characteristic speeds are the eigenvalues of the system's Jacobian matrix. By employing appropriate flux or slope limiters and artificial compression techniques, a high resolution of discontinuities can be obtained using simultaneous solvers. On the other hand, the contemporary pressure–based sequential solvers (Patankar 1980, Shyy & Braaten 1988) originally developed for incompressible flows, in which the governing differential equations are solved iteratively in a sequential manner, do not employ these attractive schemes due mainly to two reasons. One reason is the nature of the pressure–based sequential algorithms which treat the pressure gradient terms as source terms unlike the simultaneous algorithms which treat them as part of the flux vectors and hence the dependent variables such as the velocity vectors do not retain the TVD property. The other reason is that the issue of defining the local characteristic speeds (on which the nonlinear flux or slope limiters of the TVD schemes are based) for sequential formulations is largely unresolved. Moreover, the interaction between the cell Peclet number and a TVD–type scheme for recirculating flows (which often possess large gradients caused

by the balance between convective and viscous effects, instead of a Rankine–Hugoniot type of jump condition) for these sequential formulations has also not been addressed in the literature.

The present chapter attempts to understand the issues concerning the application and implementation of the above mentioned high resolution schemes in the context of a pressure–based sequential algorithm to solve Navier–Stokes equations. To better understand the implementation issues for these schemes applied to two–dimensional Navier–Stokes equations in the context of simultaneous and sequential solvers, the simpler system of one–dimensional inviscid gas dynamics (Euler) equations is the focus of study in this chapter.

Three test cases are investigated in this chapter. First, the standard shock tube problem is studied in order to evaluate the accuracy of the flowfield obtained by a sequential algorithm in the presence of discontinuities. Next, more stringent test beds such as the so–called unsteady shock tube problem and the resonant pipe problem are employed to investigate the performance of the high resolution TVD type scheme within the framework of the sequential solver. The unsteady shock tube problem involves the interaction of various waves, such as shock waves and contact surfaces, with the closed reflecting ends of the shock tube and with each other. The resonant pipe problem involves the unsteady evolution of an initial smooth pressure wave perturbation into a shocked N–wave. A larger amount of dissipation is usually required in the sequential approach in order to coordinate the couplings among different equations and to suppress the oscillations near discontinuities, leading to increased smearing of the solution profiles. To overcome this, the present study also investigates the effect of artificial compression techniques (Harten 1978) in the scheme. It is our belief that these one–dimensional unsteady flow studies will clarify the issues regarding the applicability and implementation of TVD–type modern convection schemes within a pressure–based sequential solution framework to enable their extension to multi–dimensional fluid flow problems involving complex physics.

3.2. Basic Theory of TVD Schemes

A scalar hyperbolic conservation law can be written as

$$w_t + f(w)_x \equiv w_t + a(w)\ w_x = 0 \tag{3.1}$$

$$w(x,0) = w_0$$

To allow for discontinuities, weak solutions to the system (3.1) must be admitted. The weak solutions to a conservation law are not unique and thus to obtain a physically correct solution a concept of an entropy condition is introduced (Harten 1983). The system (3.1) is assumed to possess an entropy function $\eta(w)$ such that

a) $\eta_w f_w = \Omega_u$, where Ω is some function called entropy flux, and

b) η is a convex function of w.

For smooth solutions, the entropy function η and its corresponding flux Ω satisfy the conservation law. For the weak solutions to be uniquely determined from the initial data, they must satisfy the entropy inequality (Harten 1983)

$$\eta(w)_t + \Omega(w)_x \leq 0 \tag{3.2}$$

This condition ensures that the weak solution to the hyperbolic conservation law is the physically correct one. To guarantee that we do not converge to non–solutions, the numerical scheme is preferably cast in the conservation form. If the computational domain is discretized using equal spacing Δx and Δt and k for the space and time coordinates, respectively, then the numerical approximation to the solution in the conservation form can be written as

$$w_j^{n+1} = w_j^n - \lambda\ (\bar{f}_{j+1/2}^n - \bar{f}_{j-1/2}^n) \equiv (P.w^n)_j \tag{3.3}$$

where the subscripts denote the space coordinates on the discretized grid and the superscripts denote the time level, as shown in Fig. 3.1(a). Here λ is defined as $\Delta t/\Delta x$ and $\bar{f}$ is the numerical flux at the control volume interface as shown in Fig. 3.1(a) and is based on (2k+1) points, i.e.,

$$\bar{f}^n_{j+1/2} = \bar{f}\ (w^n_{j-k+1},\ \ldots\ldots\ ,w^n_{j+k}) \tag{3.4}$$

If the numerical flux is consistent with the physical flux in the sense that

$$\bar{f}(w,\ \ w,\ \ \ldots.\ \ ,w) = f(w) \tag{3.5}$$

then the numerical scheme is said to be consistent. Moreover, the numerical scheme P in (3.3) is consistent with the entropy condition (3.2) if there exists a numerical entropy flux $\Omega_{j+1/2}$ consistent with $\Omega(w)$ in the same sense as (3.5), such that

$$\eta(w^{n+1}_j) \leq \eta(w^n_j) - \lambda(\Omega_{j+1/2} - \Omega_{j-1/2})$$

The numerical scheme has to be conservative and consistent in order to yield a weak solution to the conservation law. Scheme P, whose total variation at the current time level is defined as

$$TV(w) = \sum_{j=1}^{N} \left|w_j - w_{j-1}\right| \tag{3.6}$$

is said to be TVD (Harten 1983) if

$$TV\ (w^{n+1}) \leq TV(w^n) \tag{3.7}$$

This means that the total variation in the solution at any timestep can not be more than the total variation of the initial data and hence no spurious oscillations are exhibited in the solution. The TVD concept was first introduced by Harten (1983, 1984). These schemes are required to be total variation diminishing in the homogeneous, nonlinear, scalar case and the constant–coefficient system case. The presence of source terms in the conservation law can cause these schemes to lose their TVD property (Harten 1984, Yee 1987b).

In the present work, a typical representative of the algebraic schemes– –the well known TVD scheme of Harten (1983, 1984) is chosen for application to the shock tube problem. The basic idea in the algebraic TVD schemes is to blend a high–order flux, f^H and a low–order flux, f^L using an appropriate flux–limiter. The idea is to use the high–order flux in the smooth regions of the flow and thus maintain high accuracy and to use the low–order flux

with the appropriate flux–limiter near the discontinuity to prevent spurious oscillations. Thus the numerical flux can be expressed as

$$\bar{f}_{i+1/2} = \phi\ \bar{f}^{H}_{i+1/2} + (1-\phi)\ \bar{f}^{L}_{i+1/2}$$

$$= \bar{f}^{L}_{i+1/2} + \phi\left[\bar{f}^{H}_{i+1/2} - \bar{f}^{L}_{i+1/2}\right] \tag{3.8}$$

The function ϕ is based on an appropriate flux limiter.

Any general high resolution scheme in the form (3.3) can also be written as

$$(P.w^n)_j = w^n_j + C^{+}_{j+1/2}\Delta_{j+1/2}w^n - C^{-}_{j-1/2}\Delta_{j-1/2}w^n \tag{3.9}$$

i.e., the numerical flux can be written as

$$\bar{f}_{j+1/2} = -\frac{1}{\lambda}C^{+}_{j+1/2}\ \Delta_{j+1/2}w^n \tag{3.10}$$

It can be shown that if, for all j, the $C^{\pm}$ satisfy the following conditions:

$$C^{\pm}_{j+1/2} \geq 0\ , \qquad C^{+}_{j+1/2} + C^{-}_{j+1/2} \leq 1 \tag{3.11}$$

then the scheme P is TVD.

3.2.1. Harten' TVD Scheme for Scalar Conservation Laws

Harten (1983, 1984) has developed a five–point second–order TVD scheme from a three–point first–order accurate TVD scheme by applying the latter to a modified flux as described below. For the first–order three–point scheme, i.e., for which we have

$$\bar{f}_{j+1/2} = \bar{f}\ (w_j,\ w_{j+1}) \tag{3.12}$$

the numerical flux can be written as

$$\bar{f}_{j+1/2} = \frac{1}{2}\left[f_j + f_{j+1} - \frac{1}{\lambda}Q\left(\nu_{j+1/2}\right)\ \Delta_{j+1/2}w\right] \tag{3.13}$$

where

$$\nu = \lambda a_{j+1/2} \tag{3.14a}$$

and

$$a_{j+1/2} = \begin{cases} \dfrac{|f_{j+1} - f_j|}{\Delta_{j+1/2} w} & , \quad \text{if } \Delta_{j+1/2} w \neq 0 \\ \dfrac{\partial f}{\partial u}(w_j) & , \quad \text{if } \Delta_{j+1/2} w = 0 \end{cases} \tag{3.14b}$$

where

$$\Delta_{j+1/2} w = w_{j+1} - w_j \tag{3.14c}$$

and $Q(x)$ is a bounded function representing an appropriate amount of numerical dissipation, to be discussed later.

The numerical flux (3.13) can also be written in the form of Eq. (3.10) where $C^{\pm}$ are

$$C^{\pm}_{j+1/2} = \frac{1}{2}\left[Q\left(\nu_{j+1/2}\right) \mp \nu_{j+1/2}\right] \tag{3.15}$$

The function $Q(x)$ in (3.13) is referred to as the coefficient of numerical viscosity. It can be shown that if $Q(x)$ satisfies the inequalities

$$|x| \leq Q(x) \leq 1 \qquad \text{for} \qquad 0 \leq |x| \leq \mu \leq 1 \tag{3.16}$$

then the finite–difference scheme (3.3) with numerical flux given by (3.13) is TVD under the CFL–like restriction

$$\lambda . \max |\bar{a}^n_{j+1/2}| \leq \mu \tag{3.17}$$

where μ is the prescribed CFL criterion.

Now, we describe how to obtain a second–order TVD scheme from the above first–order scheme (Harten 1983). Truncation error analysis shows that the first–order TVD scheme, i.e, Eq. (3.3) with flux given by (3.13) approximates the modified equation

$$w_t + f_x = \Delta t\left[\tilde{g}(w,\lambda) w_x\right]_x \tag{3.18a}$$

where

$$\tilde{g}(w,\lambda) = \frac{1}{2}\left[Q(\nu) - \nu^2\right] \tag{3.18b}$$

to second–order accuracy, i.e, the first–order TVD scheme approximates the above modified viscous equation better than it does the original conservation law (3.1). Thus a second–order scheme is obtained by applying the first–order scheme to a modified flux *(f+g)* where the flux g is an approximation to the right–hand side of Eq. (3.18a), i.e.,

$$g = \Delta t\ \tilde{g}\ w_x + \mathcal{O}\left((\Delta x)^2\right) \tag{3.19}$$

The application of the first–order scheme to the flux *(f+g)* cancels the error due to the viscous terms on the right hand side of Eq. (3.18a) to $\mathcal{O}((\Delta x)^2)$; thus g behaves like an anti–diffusion flux and serves to improve the resolution of the discontinuities. The numerical flux corresponding to the second–order TVD scheme is given by

$$\tilde{f}_{j+1/2} = \frac{1}{2}\left[f_j + f_{j+1} + \frac{1}{\lambda}\left\{ g_j + g_{j+1} - Q\left(\nu_{j+1/2} + \gamma_{j+1/2}\right)\Delta_{j+1/2}w\right\}\right] \tag{3.20a}$$

where

$$\gamma_{j+1/2} = \begin{cases} \dfrac{|\,g_{j+1} - g_j\,|}{\Delta_{j+1/2}w} & , \quad \text{if } \Delta_{j+1/2}w \neq 0 \\ 0 & , \quad \text{if } \Delta_{j+1/2}w = 0 \end{cases} \tag{3.20b}$$

The function $\tilde{g}$ in (3.18a) is now the effective numerical viscosity coefficient for this second–order accurate scheme. A natural choice of $Q(x)$ under the restriction (3.15) is $Q(x)=|x|$ since it gives the least dissipative TVD scheme of the form (3.3). But for $\nu = 0$ (i.e., for zero propagation speed of discontinuities) the numerical viscosity $\tilde{g}$ vanishes and this leads to an entropy violation in scheme (3.3) with the numerical flux given by (3.20a) (this is true only in genuinely nonlinear characteristic fields). To eliminate this entropy violation, $Q(x)$ is modified near $x = 0$ and made positive. One such form of Q which has the desired

properties, suggested by Harten (1983), is the following:

$$Q(x) = \begin{cases} \frac{1}{2}\left(\frac{x^2}{\delta} + \delta\right) , & \text{if } |x| < \delta \\ |x| , & \text{if } |x| \geq \delta \end{cases} \tag{3.21}$$

Here $\delta = \delta_{j+1/2} = \delta(w_j, w_{j+1}) > 0$. An expression for δ, based on local values of w, has been developed by Harten & Hyman (1983). Thus, the amount of dissipation in this scheme can be varied by varying a parameter δ which is implicitly embedded in the scheme. The range of δ, as mentioned earlier, for the scheme to be TVD is 0 to 1, the lower extreme corresponding to the least diffusive scheme and the upper value to the most dissipative one.

The construction suggested by Harten (1983) which satisfies all the above requirements is the following:

$$g_j = minmod\left(\tilde{g}_{j+1/2}\Delta_{j+1/2}w \ , \ \tilde{g}_{j-1/2}\Delta_{j-1/2}w\right) \tag{3.22a}$$

where the function *minmod(a,b)* yields the absolute value of the minimum of a and b if they are of the same sign and zero otherwise. Mathematically this function can be expressed as

$$g_j = s.\max\left\{0, \ \min\left(\tilde{g}_{j+1/2}|\Delta_{j+1/2}w|, \ s.\tilde{g}_{j-1/2}\Delta_{j-1/2}w\right)\right\} \tag{3.22b}$$

where

$$s = sign\left(\Delta_{j+1/2}w\right) \tag{3.23}$$

and $\tilde{g}_{j\pm 1/2}$ are defined by Eq. (3.18b).

3.2.2. Artificial Compression

The resolution of the discontinuities, especially the contact discontinuity can be further improved by applying artificial compression. The basic motivation of converting a first–order TVD scheme into the second–order TVD scheme can be found in the original concept of artificial compression (Harten 1978). The resolution of the above second–order scheme can be further increased by applying the first–order scheme to $[f+(1+\omega)g]$, $\omega>0$, rather than to $(f+g)$. This is the essence of artificial compression in the context of the

second–order TVD scheme. This can be achieved by increasing the size of g by adding a term which is $O((\Delta x)^2)$ in the regions of smoothness. Two such methods have been reported in literature, in the context of Harten's TVD scheme. One method, labelled ACM1, suggested by Yee *et al.* (1985), is to replace the flux g by $\overline{g}$:

$$\overline{g}_j = \left(1 + \omega\theta_j\right)g_j, \quad \omega > 0 \tag{3.24}$$

where

$$\theta_j = \frac{\left|\Delta_{j+1/2}w - \Delta_{j-1/2}w\right|}{\left|\Delta_{j+1/2}w\right| + \left|\Delta_{j-1/2}w\right|} \tag{3.25}$$

which means that the amount of artificial compression is regulated by the ratio of second to first derivatives of the variable w on each surface of a control volume. This method involves a manual assignment for the value of ω. Yee *et al.* (1985) recommend a value of ω=2 from numerical experiments.

The second method, labelled ACM2, is the one used by Harten (1983) in which $\overline{g}$ is given by

$$\overline{g}_j = g_j + \theta_j\hat{g}_j \tag{3.26}$$

where $\hat{g}_j$ follows the minmod function, i.e.

$$\hat{g}_j = S.\max\left[\ 0, \min\left(S.\sigma_{j-1/2}\Delta_{j-1/2}w,\ \sigma_{j+1/2}\left|\Delta_{j+1/2}w\right|\right)\right] \tag{3.27a}$$

$$S = sgn\left(\Delta_{j+1/2}w\right) \tag{3.27b}$$

$$\sigma_{j+1/2} = \sigma\left(\nu_{j+1/2}\right) = \frac{1}{2}\left[1 - Q\left(\nu_{j+1/2}\right)\right] \tag{3.27c}$$

and θ_j is the same as in Eq. (3.25). In this method the manual assignment of ω as in Eq. (3.24) is replaced by the assignment of the compression factor implicitly in Eq. (3.26) using the gradient information from the evolving solution profile.

3.2.3. Application of the TVD Scheme to Systems of Conservation Laws

The TVD schemes described above can be extended to systems of conservation laws by applying them scalarly to each of the appropriately linearized variables. The system of equations in one space dimension can be written as

$$\frac{\partial W}{\partial t} + A(W)\frac{\partial W}{\partial x} = 0, \qquad A(W) = \frac{\partial F(W)}{\partial W} \tag{3.28}$$

where W and $F(W)$ are column vectors of m components and $A(W)$ is the Jacobian matrix. Since the system is hyperbolic, the matrix A has real eigenvalues denoted by $a^l(W)$ (where $l=1,...,m$) and a complete set of right eigenvectors $\mathfrak{R}^l(W)$, written as

$$\mathfrak{R}(W) = \left[\mathfrak{R}^1(W),\ \mathfrak{R}^2(W), \ldots\ldots, \mathfrak{R}^m(W)\right] \tag{3.29}$$

The inverse of the above matrix consists of the left eigenvectors of $A(W)$, denoted by $\mathfrak{R}^{-1}$ or $\mathcal{L}$. Premultiplying the basic equation by $\mathfrak{R}^{-1}$ gives

$$\mathfrak{R}^{-1}\frac{\partial W}{\partial t} + \mathfrak{R}^{-1}A\mathfrak{R}\mathfrak{R}^{-1}\frac{\partial W}{\partial x} = 0 \tag{3.30}$$

If we define characteristic variables Z as

$$Z = \mathfrak{R}^{-1}W \tag{3.31}$$

and assume locally constant coefficients, the vector equation (3.28) can be written as m decoupled scalar equations as follows:

$$\frac{\partial z^l}{\partial t} + a^l\frac{\partial z^l}{\partial t} = 0\ , \qquad a^l = const\ ; \qquad l = 1, 2, \ldots, m \tag{3.32}$$

The characteristic variables z^k can also be treated as the components of W in the coordinate system $\{\mathfrak{R}^k\}$, i.e.,

$$W = \sum_{k=1}^{m} z^k\mathfrak{R}^k \tag{3.33}$$

Let W hereafter stand for the numerical approximation to the physical variable vector W and

let $W_{j+1/2}$ be an average of W_j and W_{j+1} and let $\alpha^k_{j+1/2}$ denote the component of $\Delta_{j+1/2}W = W_{j+1} - W_j$ in the coordinate system $\{\mathfrak{R}^k\}$, i.e.,

$$\Delta_{j+1/2}W = \sum_{k=1}^{m} \alpha^k_{j+1/2}\mathfrak{R}^k_{j+1/2} \tag{3.34a}$$

$$\alpha^k_{j+1/2} = \mathcal{L}^k_{j+1/2}\Delta_{j+1/2}W \tag{3.34b}$$

Harten's TVD scheme described above for the scalar conservation law in Eqs. (3.20)–(3.23) can be extended for a general system of conservation laws as follows:

$$W^{n+1}_j = W^n_j - \lambda(\overline{F}^n_{j+1/2} - \overline{F}^n_{j-1/2}) \tag{3.35}$$

where

$$\overline{F}_{j+1/2} = \frac{1}{2}\Big[F(W_j) + F(W_{j+1})\Big] + \frac{1}{2\lambda}\sum_{k=1}^{m} \mathfrak{R}^k_{j+1/2}\Big[G^k_j + G^k_{j+1} - Q^k(\nu^k_{j+1/2} + \gamma^k_{j+1/2})\alpha^k_{j+1/2}\Big] \tag{3.36a}$$

$$\nu^k_{j+1/2} = \lambda a^k\Big(W_{j+1/2}\Big) , \tag{3.36b}$$

$$G^k_j = s^k_{j+1/2}\max\left[0,\ \min\left(\left|\tilde{G}^k_{j+1/2}\right|,\ \tilde{G}^k_{j-1/2}\ s^k_{j+1/2}\right)\right] \tag{3.36c}$$

$$s^k_{j+1/2} = sgn\left(\tilde{G}^k_{j+1/2}\right) \tag{3.36d}$$

$$\tilde{G}^k_{j+1/2} = \frac{1}{2}\Big[Q^k(\nu^k_{j+1/2}) - (\nu^k_{j+1/2})^2\Big]\alpha^k_{j+1/2} \tag{3.36e}$$

$$\gamma^k_{j+1/2} = \begin{cases} \dfrac{\left(G^k_{j+1} - G^k_j\right)}{\alpha^k_{j+1/2}}, & when\ \alpha^k_{j+1/2} \neq 0, \\ 0, & when\ \alpha^k_{j+1/2} = 0\ . \end{cases} \tag{3.36f}$$

Note that the quantities such as $U, F, \overline{F}, G, \tilde{G}$, etc. denote vector quantities for the system of

conservation laws and are written in capital letters to distinguish them from their corresponding counterparts in Eqs. (3.20)–(3.23) for the scalar conservation law (3.1).

3.3. Application to Euler Equations for the Shock Tube Problem

The system of Euler equations can be treated either as a system of simultaneous equations or a system of sequential equations. The former treatment has been the conventional one in which the TVD schemes are applied to the system of simultaneous equations using the eigenvalues and the eigenvectors of the Jacobian matrix, as described above. The latter approach, to be presented shortly, treats the equations as a collection of wave equations and the TVD scheme has to be applied with each equation considered as a scalar conservation law. To our knowledge, such an approach has not been attempted in literature and the present study explores this approach. As the first test case, the standard shock tube problem is used. An ideal gas is present in the tube on either side of a diaphragm located at the center of the tube with initial states to the left and the right of the diaphragm as shown in Fig. 3.1(b). The total length of the shock tube is 14 units and is discretized using 141 equally spaced grid points. The Courant number λ is chosen to be 0.1 and thus the timestep size Δt is 0.01. It should be pointed out that for this value of λ the CFL condition is satisfied for all the cases studied. At time t=0 the diaphragm is broken and the solution is traced at subsequent time steps. The solution profile consists of a shock wave and a contact discontinuity moving to the right of the initial location of the diaphragm and an expansion fan moving to the left. The solution profiles at any instant are compared with the exact solution used as the benchmark.

3.3.1. Euler Equations as a Simultaneous System

The inviscid gas dynamics equations in the conservation form are:

$$\frac{\partial W}{\partial t} + \frac{\partial F(W)}{\partial x} = 0 \tag{3.37}$$

where the vector W of conservative variables and the flux vector F are given by

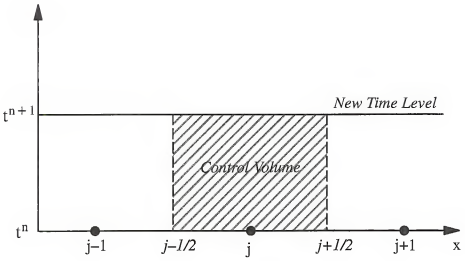

(a) Schematic of the control volume.

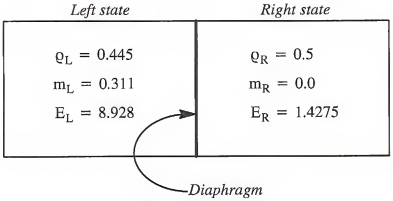

(b) Schematic of the shock tube problem.

Fig. 3.1. Schematics of the control volume and the shock tube problem.

$$W = \begin{bmatrix} \varrho \\ m \\ E \end{bmatrix}, \qquad F = \begin{bmatrix} m \\ m^2/\varrho + p \\ (E + p)m/\varrho \end{bmatrix} \tag{3.38}$$

where $m = \varrho u$, ϱ is the density, u is the velocity, p is the static pressure and E is the total energy per unit volume defined as

$$E = \varrho\left(e + \frac{u^2}{2}\right) \tag{3.39a}$$

where $e = c_v T$ is the specific internal energy. The pressure p for a perfect gas is defined using the equation of state as

$$p = \varrho e(\gamma - 1) = \left(E - \frac{m^2}{2\varrho}\right)(\gamma - 1) \tag{3.39b}$$

where γ is the ratio of specific heats at constant pressure and constant volume, respectively. The total enthalpy of the gas can be expressed as

$$H = \frac{c^2}{\gamma - 1} + \frac{u^2}{2} \tag{3.39c}$$

in which c is the sound speed given by

$$c = \sqrt{\frac{\partial p}{\partial \varrho}} = \sqrt{\gamma \frac{p}{\varrho}} \tag{3.39d}$$

The equation (3.37) can also be written in the form

$$\frac{\partial W}{\partial t} + A(W)\frac{\partial W}{\partial x} = 0 \tag{3.40}$$

where $A(W) = \partial F/\partial W$ is the Jacobian matrix given by

$$\begin{bmatrix} 0 & 1 & 0 \\ (\gamma - 3)u^2/2 & (3 - \gamma)u & (\gamma - 1) \\ u(\gamma - 1)u^2/2 - uH & H - (\gamma - 1)u^2 & \gamma u \end{bmatrix} \tag{3.41}$$

The eigenvalues of the above Jacobian matrix are given by

$$(a^1, a^2, a^3) = (u - c, \quad u, \quad u + c) \tag{3.42}$$

The right eigenmatrix corresponding to these eigenvalues is given by

$$\mathfrak{R} = \begin{bmatrix} 1 & 1 & 1 \\ u - c & u & u + c \\ H - uc & \frac{u^2}{2} & H + c \end{bmatrix} \tag{3.43}$$

The inverse of the above $\mathfrak{R}$ matrix is the left eigenmatrix given by

$$\mathfrak{R}^{-1} = \begin{bmatrix} \frac{1}{2}\left(b_1 + \frac{u}{c}\right) & \frac{1}{2}\left(-b_2 u - \frac{1}{c}\right) & \frac{1}{2} b_2 \\ 1 - b_1 & b_2 u & -b_2 \\ \frac{1}{2}\left(b_1 - \frac{u}{c}\right) & \frac{1}{2}\left(-b_2 u + \frac{1}{c}\right) & \frac{1}{2} b_2 \end{bmatrix} \tag{3.44}$$

where

$$b_1 = b_2 \frac{u^2}{2} \qquad\qquad b_2 = \frac{\gamma - 1}{c^2} \tag{3.45}$$

Thus the vector α of Eq. (3.34b) can be written as

$$\begin{bmatrix} \alpha^1_{j+1/2} \\ \alpha^2_{j+1/2} \\ \alpha^3_{j+1/2} \end{bmatrix} = \begin{bmatrix} (aa - bb)/2 \\ \Delta_{j-1/2}\varrho - aa \\ (aa + bb)/2 \end{bmatrix} \tag{3.46}$$

where aa and bb are defined as

$$aa = \frac{\gamma - 1}{c^2_{j+1/2}}\left[\Delta_{j+1/2}e + \frac{u^2_{j+1/2}}{2}\Delta_{j+1/2}\varrho - u_{j+1/2}\Delta_{j+1/2}m\right] \tag{3.47a}$$

$$bb = \frac{\Delta_{j+1/2}m - u_{j+1/2}\Delta_{j+1/2}\varrho}{c_{j+1/2}} \tag{3.47b}$$

Recall that $\Delta_{j+1/2}\, m = m_{j+1} - m_j$, etc.

The simplest form of averaging for calculating $W_{j+1/2}$ is the algebraic average of W_j and W_{j+1}. Another form of averaging has been suggested by Roe (1981) that resolves stationary discontinuities perfectly for the gas dynamics equations. Both averaging methods

have been used in the present study. Also, as seen from Eq. (3.35), the time–discretization scheme used is the well known explicit backward Euler scheme.

The density profiles of the shock tube problem after elapsed time t=2.0 for the system of simultaneous Euler equations obtained by using the first–order upwind and the conventional second–order Lax–Wendroff schemes are shown in Fig. 3.2. The first order scheme smears out the profiles near the discontinuities whereas the second–order Lax–Wendroff scheme yields spurious oscillations. The density and energy profiles at t=2.0 obtained using Harten's TVD scheme, i.e. Eqs. (3.35)–(3.36), for the system of simultaneous Euler equations with δ=0, both with and without artificial compression are plotted in Fig. 3.3. The profiles in Fig. 3.3(b) correspond to ω = 0.0, 2.0 and 3.0 for the expansion fan, contact discontinuity and the shock regions, respectively (i.e., corresponding to the eigenvalues a^1, a^2 and a^3, respectively). It can be seen that the TVD scheme gives high–order accuracy in the smooth region of the flow and a much better resolution of the discontinuities, more so with artificial compression, exhibiting no presence of spurious oscillations, compared to the conventional schemes. As the amount of dissipation in the TVD scheme is increased by successively using higher δ, the profiles become more and more smeared.

3.3.2. Euler Equations as a Sequential System

Using a sequential solution approach, the gas dynamics equations have to be treated as a collection of individual wave equations and the TVD scheme has to be applied to each equation treated as a scalar conservation law. Different approaches have been employed in the present study in order to understand the issues behind effective application of the TVD schemes for a sequential solution approach and are described below.

Approach A: naive extension of the TVD scheme for scalar conservation laws

Treating the Euler equations as individual scalar conservation laws for the dependent variables ϱ, m and E, respectively, the equations can be written as

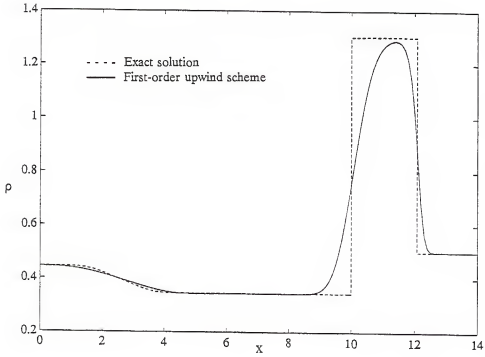

(a) First-order upwind scheme

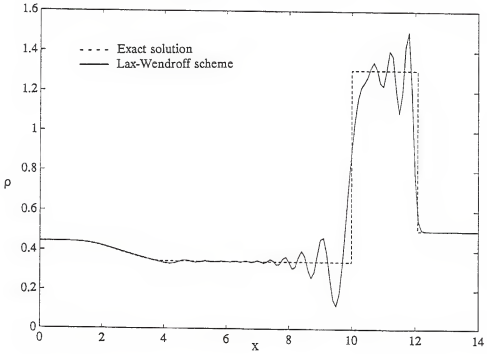

(b) Lax-Wendroff scheme

Fig. 3.2. Density profiles of the shock tube problem using the simultaneous solution approach with first–order upwind and second–order Lax–Wendroff schemes.

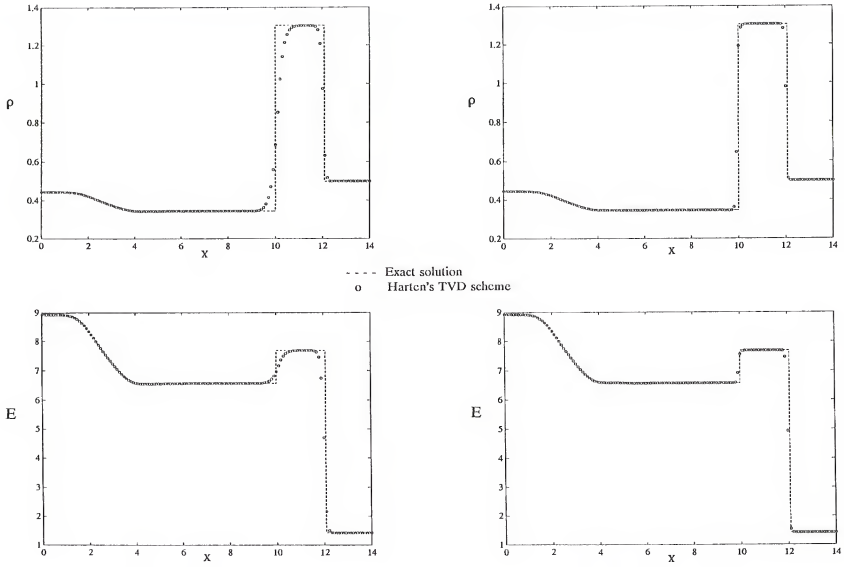

(a) Without artificial compression

(b) With artificial compression

Fig. 3.3. Density and energy profiles for the shock tube using the simultaneous solution approach with Harten's TVD scheme.

$$\frac{\partial \varrho}{\partial t} + \frac{\partial [m]}{\partial x} = 0 \tag{3.48a}$$

$$\frac{\partial m}{\partial t} + \frac{\partial}{\partial x}\left[\frac{m^2}{\varrho} + (\gamma - 1)\left(E - \frac{m^2}{2\varrho}\right)\right] = 0 \tag{3.48b}$$

$$\frac{\partial E}{\partial t} + \frac{\partial}{\partial x}\left[\frac{Em}{\varrho} + (\gamma - 1)\left(E - \frac{m^2}{2\varrho}\right)\frac{m}{\varrho}\right] = 0 \tag{3.48c}$$

The convective fluxes for the three dependent variables, namely f_ϱ, f_m and f_E, respectively are the quantities in the square brackets in the above three equations. The local characteristic speeds ($a_{j+1/2}$) for these three equations, according to the standard notion, i.e, Eq. (3.14b), are

$$a_{j+1/2} = \frac{f_{j+1} - f_j}{w_{j+1} - w_j} \tag{3.49}$$

where f is the flux and w denotes the relevant conserved quantity, i.e., ϱ, m or E. Thus the TVD scheme can be applied to these three equations individually, using a different characteristic speed for each scalar conservation law as specified by Eq. (3.49). Fig. 3.4(a) shows the density and energy profiles at elapsed time t=2.0 using δ=0.2. Though the shock seems to be captured quite effectively, one observes nonphysical oscillations away from the shock. This behavior is found to be independent of the size of the timestep and the amount of dissipation in the scheme. Fig. 3.4(b) shows the density and energy profiles for δ=1.0, i.e, the maximum allowable amount of dissipation in the scheme. The nonphysical oscillations are still present, though less than the previous case. Another point to be noted is that this behavior is not due to a instability caused by violation of the CFL condition given by Eq. (3.17). If we calculate λ for every timestep based on the CFL criterion (3.17) with μ=0.9 and the local characteristic speed (3.14b), the value of λ turns out to be very low as given in Table 3.1. This might lead one to conclude that very small values of λ, i.e., a very small timestep size is needed in order to avoid spurious oscillations using the TVD scheme in the framework of

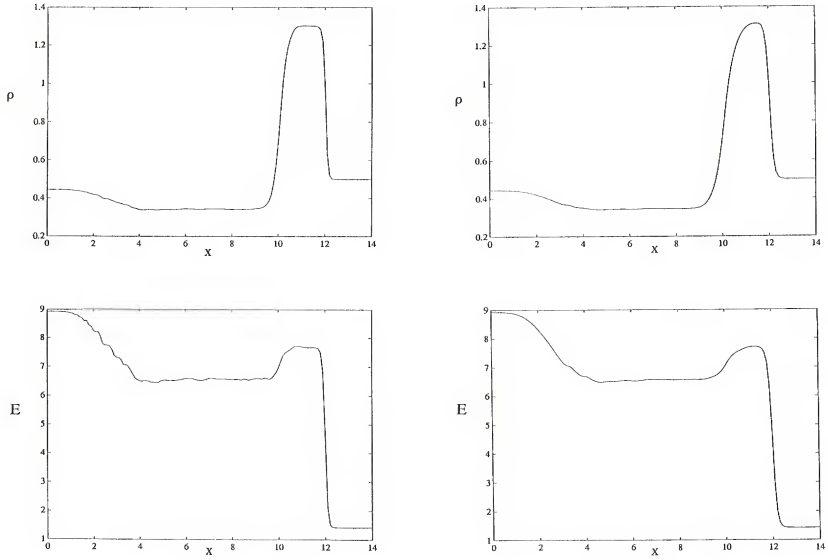

(a) $\delta = 0.2$ (b) $\delta = 1.0$

Fig. 3.4. Density and energy profiles for the shock tube using the sequential approach A.

approach A. But, in reality, these small values of λ are a result of the fact that the characteristic speeds of the three equations in the Euler system are different, leading to a nonphysical and asynchronous propagation of the physical variables. This is evident from the corresponding values of λ for the case of the simultaneous system of equations (Table 3.1) which are more realistic, namely they are of order O(1), due to the fact that the propagation of all the variables is synchronized by the eigenvalues of the Jacobian matrix of the Euler system. Thus it can be seen that a straightforward implementation of such schemes in a sequential solution approach can not be meaningful because according to Eq. (3.49), each equation possesses a different characteristic speed that is not commensurate to others. In reality, however, as indicated by Eqs. (3.34) and (3.36) for the simultaneous system of equations, all three characteristic speeds are present in every equation; this requirement cannot be accommodated in sequential approach A, and hence a strict adoption of a characteristic–based technique can not be applied. Thus, a new approach has to be taken as described next.

Table 3.1. Values of λ for sequential approach A and simultaneous approach using CFL number = 0.9.

Timestep	For sequential approach A	For simultaneous approach
1	8.81×10^{-2}	0.235
2	1.05×10^{-2}	0.216
3	2.11×10^{-3}	0.214
4	2.74×10^{-3}	0.210
5	3.03×10^{-3}	0.207
6	3.24×10^{-3}	0.205
7	3.41×10^{-3}	0.204
8	3.57×10^{-3}	0.203
9	2.80×10^{-3}	0.202
10	3.66×10^{-3}	0.202

Approach B: coordinated characteristics

From the above discussion it is clear that we need to prescribe a characteristic speed for the entire system of sequential equations, instead of the individual equations. The obvious choice is the convection speed u in the Euler equations. Thus the system can be written as follows

$$\frac{\partial \varrho}{\partial t} + \frac{\partial [\varrho u]}{\partial x} = 0 \tag{3.50a}$$

$$\frac{\partial m}{\partial t} + \frac{\partial [mu]}{\partial x} = -\frac{\partial p}{\partial x} \tag{3.50b}$$

$$\frac{\partial E}{\partial t} + \frac{\partial [Eu]}{\partial x} = -\frac{\partial (pu)}{\partial x} \tag{3.50c}$$

where the pressure p is defined in Eq. (3.39b). In Eq. (3.50), the terms on the right–hand side are treated as source terms. Previously in Eq. (3.48) for approach A, they are placed on the left–hand side of the equations and considered as part of the fluxes. The local characteristic speed $a_{j+1/2}$ defined on the right interface of the control volume for all of the above three equations is now defined as

$$a_{j+1/2} = \frac{1}{2}\left(u_j + u_{j+1}\right) \tag{3.51}$$

Thus each of the scalar conservation laws has the same characteristic speed, namely u, and the terms involving pressure are now source terms. It should be noted that this form of the equations is consistent with the form of Navier–Stokes equations written for the sequential pressure–based methods (Patankar 1980, Shyy & Braaten 1988).

The algebraic TVD scheme of Harten is now applied to this system. Explicit backward Euler time discretization is used as shown in Eq. (3.3) with the source terms appearing explicitly. The source terms are not treated in any special manner and just appear explicitly in the discretized equation. As in the simultaneous case, the value of λ used in these calculations is 0.1 with the timestep size Δt=0.01. For δ=0, i.e., for the least amount of

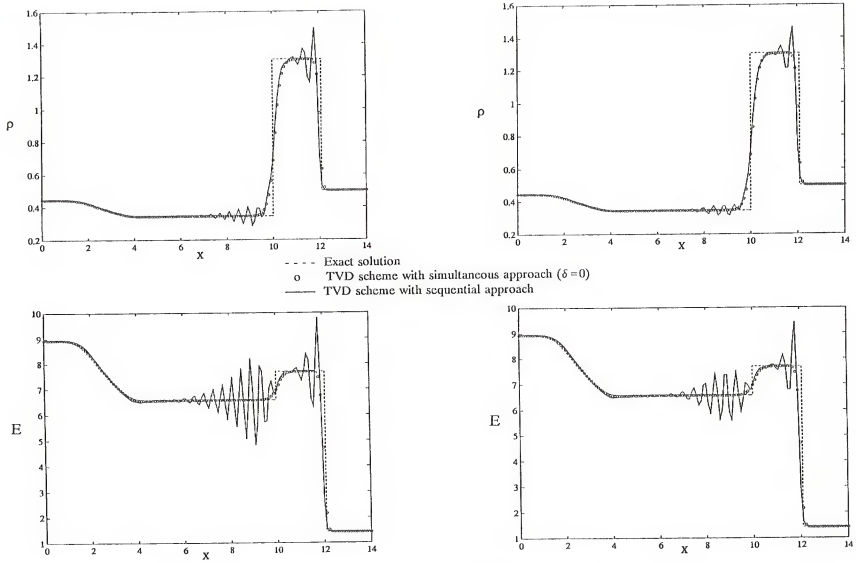

(a) $\delta = 0.0$ (b) $\delta = 0.2$

Fig. 3.5. Density and energy profiles for the shock tube using the sequential solution approach B with no special treatment for source terms, for differenrt values of δ.

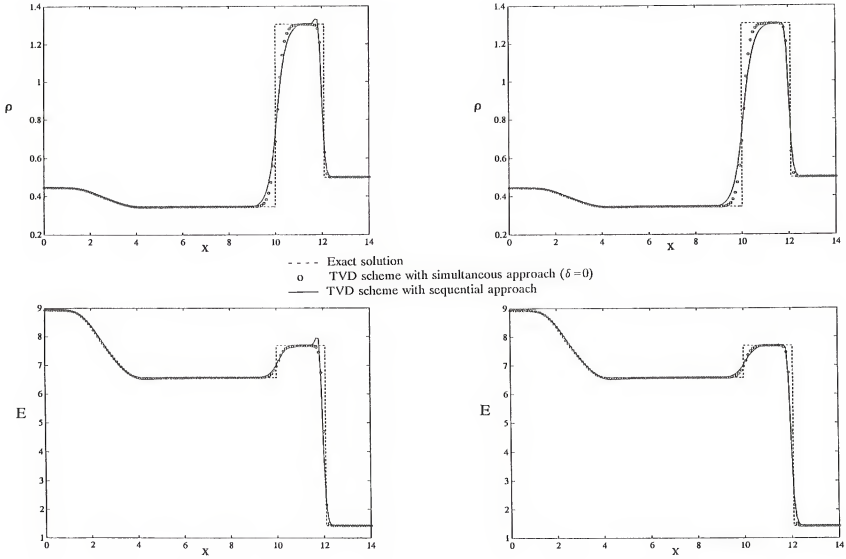

(c) δ = 0.6

(d) δ = 0.8

Fig. 3.5. continued.

allowable dissipation in this scheme, it yields severe oscillations near the discontinuities, as seen in Fig. 3.5(a), which can be attributed to two factors. One is the lack of dissipation in the scheme and the other is the presence of source terms on the right hand side of Eq. (3.50). To observe the effect of the amount of dissipation on the accuracy of the scheme, the value of δ is successively increased; the plots for various δ are shown in Fig. 3.5. The profiles obtained using the simultaneous solution approach (with δ=0.2 for all the plots of the simultaneous equations case) are also plotted in Fig. 3.5 to compare the relative accuracy of the sequential approach for varying values of δ, both in terms of the presence of oscillations and the amount of smearing of the profiles. Figure 3.5 shows that the oscillations, which are present near the contact discontinuity and the shock, are successively reduced as δ is increased but the profiles become more and more smeared. It is seen that for lower δ the density and energy profiles compare very well with that obtained using the simultaneous approach in terms of smearing of the profile in the region of the contact discontinuity and the shock but some oscillations are present. The oscillations are completely suppressed for $\delta \geq 0.8$, as seen in Fig. 3.5(d), but the profiles are more smeared compared to the simultaneous approach.

Approach C: Coordinated Characteristics with Special Source Term Treatment

As mentioned earlier, one of the reasons for the presence of oscillations is the source terms. It is well known (Yee 1987, LeVeque & Yee 1990) that the high resolution schemes no longer possess the TVD property in the presence of source terms, except in some special cases. A conservation law for the dependent variable w, with a source term $\Psi(w)$ can be written as

$$w_t + f(w)_x = \psi(w) \tag{3.52}$$

In order to treat the source terms, several approaches have been suggested in literature (Yee 1987, LeVeque & Yee 1990, Chang 1990), and are described below.

Method I. The first method, labelled method I, is an extension of MacCormack's predictor–corrector method, treating the source terms in an explicit manner and maintaining second–order accuracy. Let w denote the dependent variable in the scalar conservation law, namely ϱ, m or E for the three equations, respectively; then this method can be written as follows: first, for the predictor step

$$\Delta w_j^{(1)} = -\lambda\left(f(w_j^n) - f(w_{j-1}^n)\right) + \Delta t\psi(w_j^n) \tag{3.53a}$$

$$w_j^{(1)} = w_j^n + \Delta w_j^{(1)}$$

next, for the corrector step,

$$\Delta w_j^{(2)} = -\lambda\left(f(w_{j+1}^{(1)}) - f(w_j^{(1)})\right) + \Delta t\psi(w_j^{(1)}) \tag{3.53b}$$

$$w_j^{(2)} = w_j^n + \frac{1}{2}\left(\Delta w_j^{(1)} + \Delta w_j^{(2)}\right)$$

and the final updated value at the time step (n+1) is obtained from

$$w_j^{n+1} = w_j^{(2)} - \lambda\left[\ \bar{f}_{j+1/2}\left(w^{(2)}\right) - \bar{f}_{j-1/2}\left(w^{(2)}\right)\ \right] \tag{3.53c}$$

where the last step involves the incorporation of flux limiters using the TVD flux $\bar{f}$ defined in Eq. (3.20a).

Method II. For stiff source terms, one technique is to handle the source term implicitly whereas the flux terms remain explicit. Such a modification of method I, labelled method II, is a semi–implicit extension of MacCormack's predictor–corrector method (Yee 1987, LeVeque & Yee 1990). This method can be written as:

$$\left[1 - \frac{1}{2}\,\Delta t\ \psi'\left(w_j^n\right)\right]\Delta w_j^{(1)} = -\lambda\left\{f\left(w_j^n\right) - f\left(w_{j-1}^n\right)\right\} + \Delta t\ \psi\left(w_j^n\right)$$

$$w_j^{(1)} = w_j^n + \Delta w_j^{(1)}$$

$$\left[1 - \frac{1}{2}\,\Delta t\ \psi'\left(w_j^n\right)\right]\Delta w_j^{(2)} = -\lambda\left\{f\left(w_{j+1}^{(1)}\right) - f\left(w_j^{(1)}\right)\right\} + \Delta t\ \psi\left(w_j^n\right) \tag{3.54}$$

$$w_j^{(2)} = w_j^n + \frac{1}{2}\left(\Delta w_j^{(1)} + \Delta w_j^{(2)}\right)$$

$$w_j^{n+1} = w_j^{(2)} - \lambda\left[\tilde{f}_{j+1/2}\left(w^{(2)}\right) - \tilde{f}_{j-1/2}\left(w^{(2)}\right)\right]$$

where the last step involves the incorporation of flux limiters using the TVD flux $\tilde{f}$ defined in Eq. (3.20a). The above method is second–order accurate both in space and time. For the system given by Eqs. (3.50), the $\psi'(w)$ terms can be obtained using Eq. (3.39b) as follows:

$$\textit{Momentum} \;:\quad \psi'(m) = \frac{\partial}{\partial m}\left(-\frac{\partial p}{\partial x}\right) = (\gamma - 1)\frac{\partial(m/\varrho)}{\partial x} \tag{3.55a}$$

$$\textit{Energy} \;:\quad \psi'(E) = \frac{\partial}{\partial E}\left(-\frac{\partial(pu)}{\partial x}\right) = -(\gamma - 1)\frac{\partial(m/\varrho)}{\partial x} \tag{3.55b}$$

<u>Method III.</u> The third approach is to use a time–splitting method in which the conservation law without the source term and the ODE involving the unsteady term and the source term are solved alternately (LeVeque & Yee 1990). Strang's time–splitting (Strang 1968) is used, which maintains second–order accuracy:

$$w^{n+1} = S_\psi(\Delta t/2)\;\; S_f(\Delta t)\;\; S_\psi(\Delta t/2)\;\; w^n \tag{3.56}$$

where S_f represents the numerical solution operator for the system

$$w_t + f(w)_x = 0 \tag{3.57a}$$

and $S\psi$ is the numerical solution operator for the ODE

$$w_t = \psi(w) \tag{3.57b}$$

These operators have the following form:

$S\psi(\Delta t/2)$:

$$\left[1 - \frac{1}{4}\,\Delta t\,\psi'\left(w_j^n\right)\right]\Delta w_j^* = \frac{1}{2}\,\Delta t\,\psi\left(w_j^n\right) \tag{3.58a}$$

$$w_j^* = w_j^n + \Delta w_j^*$$

$S_f(\Delta t)$:

$$\Delta w_j^{(1)} = -\lambda\left(f(w_j^*) - f(w_{j-1}^*)\right)$$

$$w_j^{(1)} = w_j^* + \Delta w_j^{(1)}$$

$$\Delta w_j^{(2)} = -\lambda\left(f(w_{j+1}^{(1)}) - f(w_j^{(1)})\right) \tag{3.58b}$$

$$w_j^{(2)} = w_j^* + \frac{1}{2}\left(\Delta w_j^{(1)} + \Delta w_j^{(2)}\right)$$

$$w_j^{**} = w_j^{(2)} - \lambda\left[\,\bar{f}_{j+1/2}\left(w^*\right) - \bar{f}_{j-1/2}\left(w^*\right)\,\right]$$

$S\psi(\Delta t/2)$:

$$\left[1 - \frac{1}{4}\,\Delta t\,\psi'\left(w_j^{**}\right)\right]\Delta w_j^{**} = \frac{1}{2}\,\Delta t\,\psi\left(w_j^{**}\right) \tag{3.58c}$$

$$w_j^{n+1} = w_j^{**} + \Delta w_j^{**}$$

where again the numerical flux $\bar{f}$ is defined in Eq. (3.20a).

The above three methods are employed to treat the source terms (i.e, the terms involving pressure) in the Euler equations. Harten's TVD scheme is used with and without artificial compression. Artificial compression is applied using the two methods described by Eqs. (3.24)–(3.27). For each of the three scalar equations (3.50a–c), we use $w \equiv \varrho$ in Eq. (3.25). Any other flow variable which is discontinuous across shocks and contact discontinuities, such as entropy, can also be used to serve as an automatic switch to identify the discontinuities (Harten 1978). In order to prevent the application of artificial compression in the regions of small fluctuation of flow variables due to the numerical

procedure rather than the presence of a discontinuity, the following modification is made:

$$\theta_j = \begin{cases} \theta_j \ \ of \ \ Eq.(3.25) & \text{if} \quad \left|\Delta_{j+1/2}\varrho\right| + \left|\Delta_{j-1/2}\varrho\right| > \varepsilon \\ 0 & otherwise \end{cases} \tag{3.59}$$

where ε is a measure of an insignificant variation of density. Since artificial compression should not be applied in the regions where the characteristics are divergent, namely in expansion waves, θ_j is set to zero in the expansion waves where the following inequality holds:

$$\frac{m_{j+1} - m_{j-1}}{\varrho_{j+1} - \varrho_{j-1}} \cdot sign\left(u_j\right) > 0 \tag{3.60}$$

The density and energy profiles obtained using method I to treat the source terms are shown in Fig. 3.6. For the same values of δ the oscillations in the profiles are substantially reduced compared to the previous case (Fig. 3.5) where no special treatment is given to the source terms. As the amount of dissipation is increased, by increasing the value of δ to 0.6, the oscillations are eliminated. It should be noted that the oscillation–free density profile for δ=0.6 is only slightly smeared compared to that obtained using the simultaneous approach, as seen in Fig. 3.6(c), whereas for the previous case in which no special treatment is extended to the source terms, a higher value of δ, namely δ=0.8, has to be used to completely eliminate oscillations leading to a more smeared profile (Fig. 3.5(d)). The density and energy profiles obtained using methods II and III to treat the source terms are shown in Figs. 3.7 and 3.8, respectively. Method II does not perform as well as method I. For method II, the density and energy profiles exhibit some spurious oscillation near the shock and relatively more smearing in the contact discontinuity region for δ up to 0.6, as seen in Fig. 3.7, whereas for method I, a relatively satisfactory solution is observed for δ=0.6. As seen from Figs. 3.6 and 3.8, method III yields results very similar to those obtained by method I. Fig. 3.9 summarizes

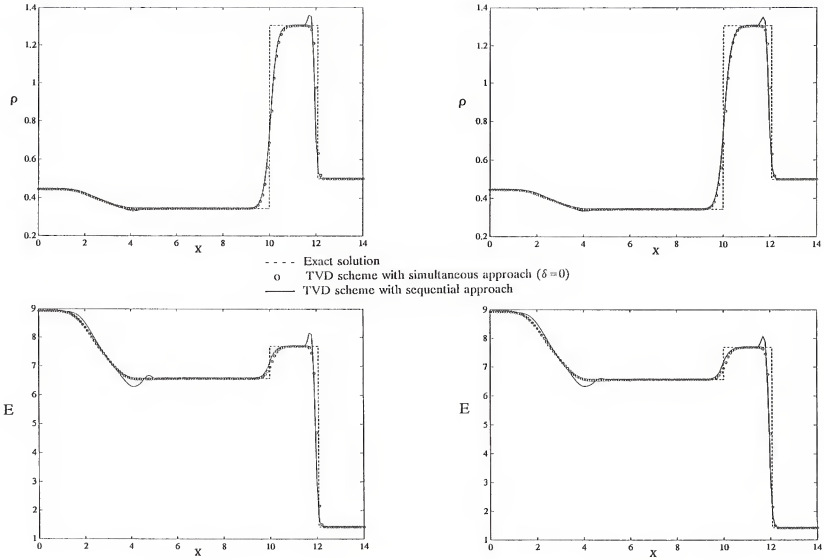

(a) $\delta = 0.0$ (b) $\delta = 0.2$

Fig. 3.6. Density and energy profiles using the sequential solution approach C with method I to treat the source terms, for various δ.

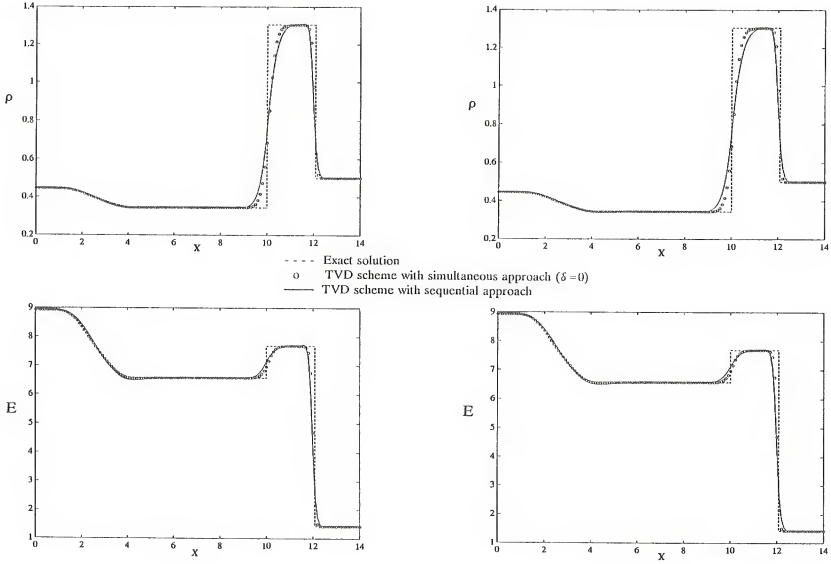

(c) δ = 0.6

(d) δ = 0.8

Fig. 3.6. continued.

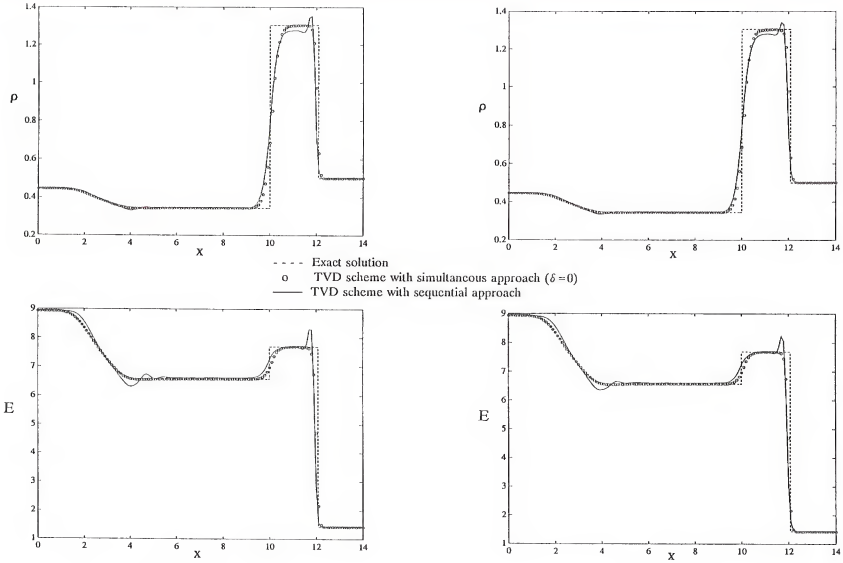

(a) $\delta = 0.0$ (b) $\delta = 0.2$

Fig. 3.7. Density and energy profiles using the sequential solution approach C with method II to treat the source terms, for various δ.

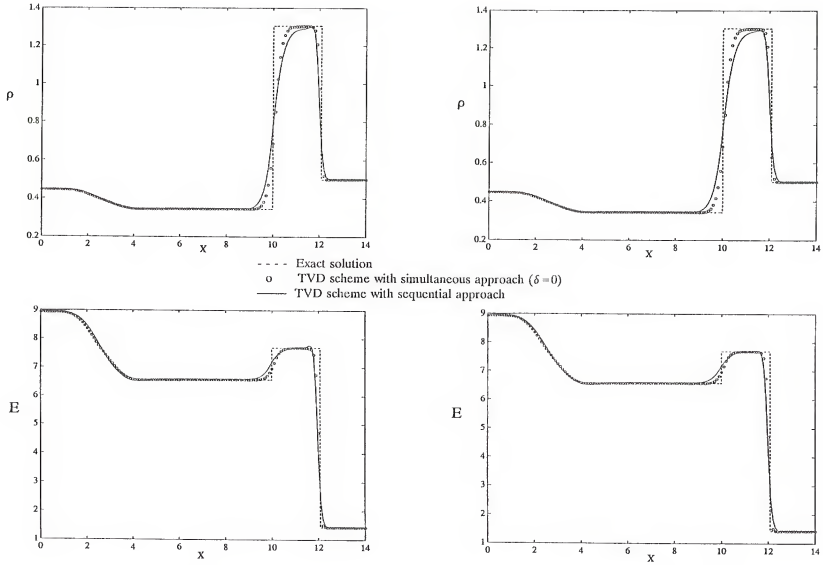

(c) δ = 0.6

(d) δ = 0.8

Fig. 3.7. continued.

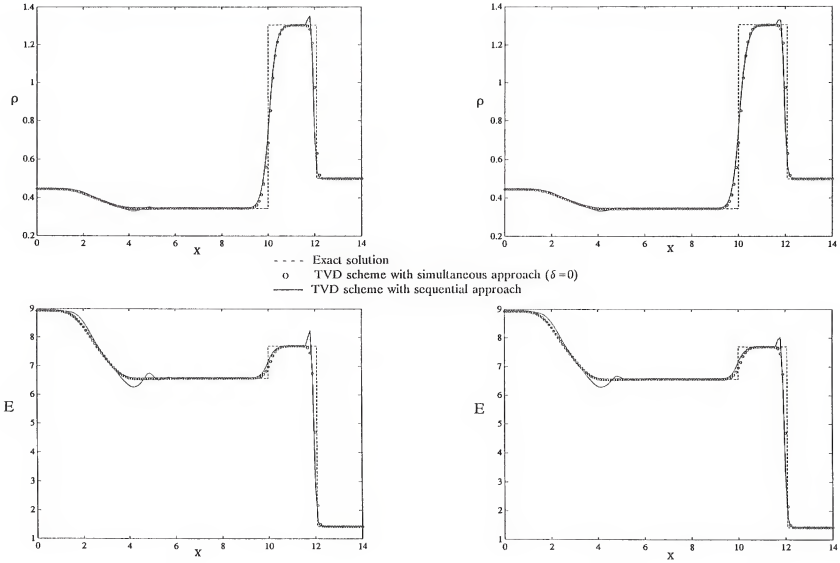

(a) $\delta = 0.0$ (b) $\delta = 0.2$

Fig. 3.8. Density and energy profiles using the sequential solution approach C with method III to treat the source terms, for various δ.

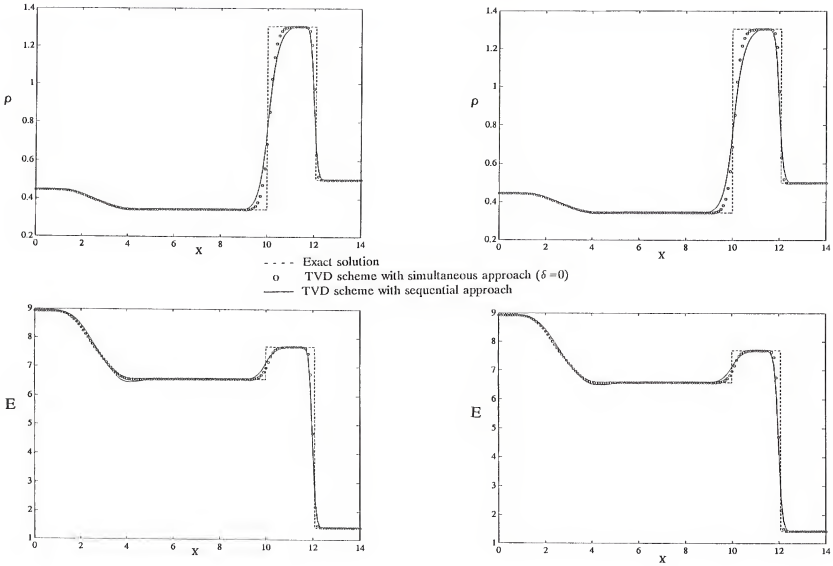

(c) $\delta = 0.6$

(d) $\delta = 0.8$

Fig. 3.8. continued.

- - - - - - Exact solution
o TVD scheme with simultaneous approach ($\delta = 0$)
——— TVD scheme with sequential approach

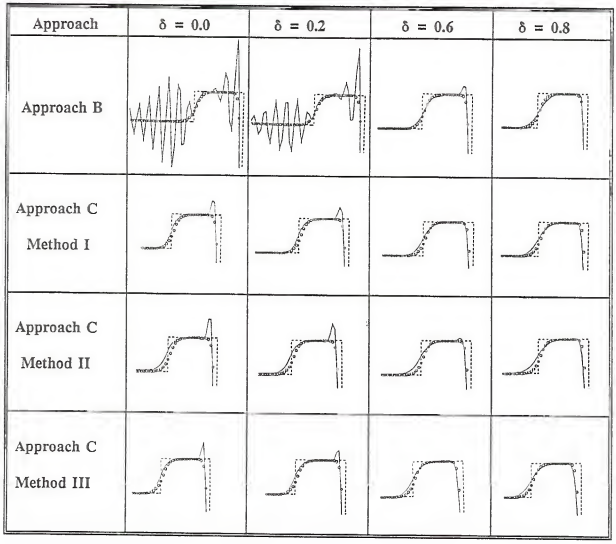

- Approach B : Coordinated characteristics; no special source term treatment
- Approach C : Coordinated characteristics with special source term treatment-
  - Method I : MacCormack's explicit predictor-corrector method
  - Method II : MacCormack's semi-implicit predictor-corrector method
  - Method III : Strang's time-splitting method

Fig. 3.9. Summary of energy profiles near the shock for the shock tube problem using the sequential solution approaches B and C; $\lambda = 0.01$, $t = 2.0$.

the performance of approaches B and C by tabulating energy profiles in the vicinity of the shock and the contact discontinuity.

3.3.3. Effect of Numerical Dissipation on the Shock Tube Problem

Taking advantage of the fact that the treatment of the source terms in a special manner, as described above, substantially increases the accuracy of the scheme, we next present some numerical experiments with selective dissipation within the framework of a method to treat the source terms in a special manner, e.g., method I discussed above, both in the context of time and space variables. First, since the magnitude of δ is an indicator of the amount of dissipation in the scheme, we use different values of δ in different regions along the shock tube, namely, higher values of δ in the regions in which oscillations occur (e.g., in the vicinity of the expansion fan and the shock wave) and lower δ in the rest of the domain to minimize smearing of the profile. This serves to suppress the oscillations by increasing the dissipation in the regions in which they occur while giving high resolution in the profile by minimizing the dissipation in the rest of the field. Density profiles using four such experiments are shown in Fig. 3.10. The length of the shock tube in the present case is 14 units. The initial location of the diaphragm before it is broken is at x=7.0. After time t=2.0 the expansion fan spans the region x=1.5 to x=4.5, and the shock wave spans x=11.7 to x=12.2, approximately. With the method I, one observes the oscillations mainly in the region x=3.8 to x=4.5 and x=11.4 to x=11.8, respectively. The values of δ used in various regions in the four cases shown in Fig. 3.10 have been summarized in Table 3.2. We see that results of accuracy comparable to those obtained from the simultaneous approach can be obtained in this manner, as seen in Fig. 3.10(d), where higher δ is used for the entire development of the expansion fan region and the final location of the shock. Such experiments, obviously are *ad hoc* in the sense that they demand knowledge of the location of the discontinuities as well as the resulting oscillations *a priori*, which means that we first need to obtain results exhibiting oscillations before we can selectively increase δ along the domain to obtain the final solution.

Table 3.2. Values of δ for four cases shown in Fig. 3.10 using the sequential approach C with method I to treat the source terms.

Case	Range of x	Value of δ
I	1.5–5.0 rest of x	0.6 0.0
II	1.5–5.0 11.4–12.0 rest of x	0.6 0.6 0.0
III	3.2–4.8 11.4–12.0 rest of x	0.6 0.6 0.0
IV	1.0–7.5 11.4–12.0 rest of x	0.6 0.6 0.0

Clearly, an automatic selection mechanism is required to select the appropriate value of δ for different regions in the flowfield in order to inject just the right amount of dissipation at all points in the domain such that the oscillations are suppressed, while maintaining high resolution at the same time. Nevertheless, these results (Fig. 3.10) clearly show that we can achieve the desired accuracy using the sequential approach by selectively using higher dissipation in the required regions of the flowfield.

The second set of numerical experiments involve the variation of δ with time. All the profiles are plotted at time t=2.0 which takes 200 timesteps to be reached, with the step size Δt=0.01. Since the amount of dissipation in the scheme accumulates with time, we explore the possibility of using the minimum allowable dissipation, namely δ=0, for a majority of the timesteps, and using a high amount of dissipation, say δ=0.8, for the remaining timesteps leading to the final time t=2.0 at which the solution is desired. The timestep at which the value of δ is increased from 0 to 0.8 is labelled as the switching timestep. Figure 3.11 shows the density profiles for various switching timesteps. With this approach the solution exhibits oscillations at the intermediate time steps for which δ=0 is used (this is indeed the case but has not been shown in the figure), but the high resolution of the solution profiles is not affected. As observed from Fig. 3.11, the high amount of dissipation in the last few timesteps

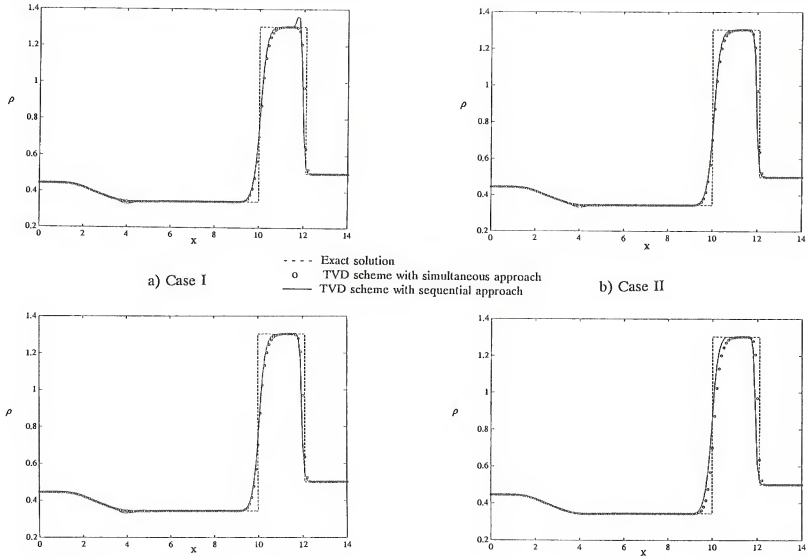

a) Case I

b) Case II

c) Case III

d) Case IV

Fig. 3.10 Density profiles using the sequential solution approach C with method I to treat the source terms, for various values of δ given in Table 3.2.

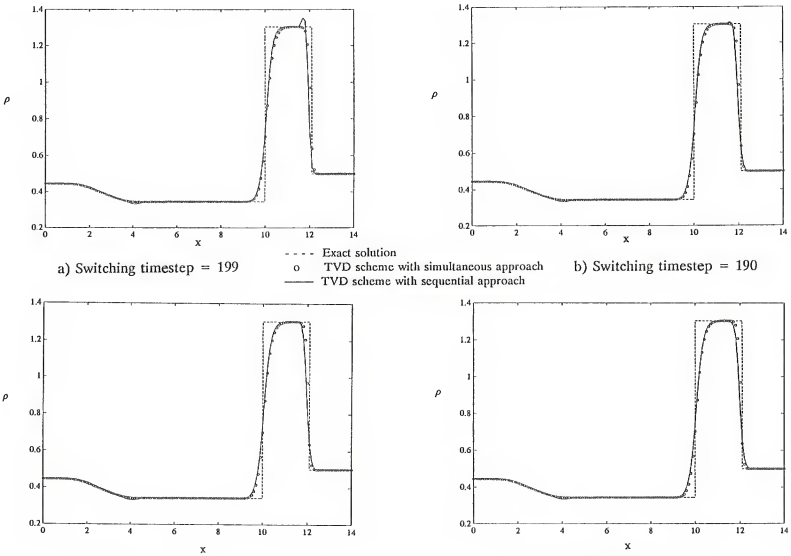

a) Switching timestep = 199

b) Switching timestep = 190

c) Switching timestep = 180

d) Switching timestep = 170

Fig. 3.11. Density profiles using the sequential solution approach C with method I to treat the source terms, for different switching timesteps.

is sufficient to damp out the oscillations, provided a sufficient number of timesteps are allowed to accumulate enough dissipation, while not deteriorating the resolution of the solution profiles by a large extent.

3.4. Unsteady Flow in a Shock Tube with Reflecting Boundaries

The second case studied is the unsteady flow of a polytropic gas (γ=1.4) in a closed shock tube. The case investigated here is the same as that studied by Wang and Widhopf (1989) and involves the reflections of the various waves at the solid ends of the tube and their subsequent interactions with each other. This case tests the efficacy of the scheme to resolve the complex flowfield resulting from the interaction of the various waves. The initial conditions of the gas on either side of the diaphragm and the exact values of flow variables at any instant after the diaphragm is broken are shown in Fig. 3.12. After the diaphragm is broken, a shock wave and a contact discontinuity propagate towards the right end of the tube whereas an expansion wave propagates towards the left. The shock is reflected from the right end of the tube at (x,t)=(–4.1,1.823), interacts with the contact surface at (3.238,2.529) and is transmitted as shown in the figure. The contact surface is reflected at the point of interaction with the shock and moves to the left with a speed 0.411; at the same point an expansion wave is generated and propagates to the right. At this time, the original expansion wave front that is reflected at the left end of the tube is located to the left of x=1.889 and it can be shown that its interaction with the transmitted shock is very weak (Wang & Widhopf 1989).

The conditions of reflection of the pressure wave, no heat conduction and rigidity at the ends of the tube specify the boundary conditions, namely

$$\frac{\partial p}{\partial x} = 0 \quad \Rightarrow \quad p_1 = p_2 \,, \quad p_{nj} = p_{nj-1} \tag{3.61a}$$

$$\frac{\partial T}{\partial x} = 0 \quad \Rightarrow \quad T_1 = T_2 \,, \quad T_{nj} = T_{nj-1} \tag{3.61b}$$

$$u_{bound} = 0 \quad \Rightarrow \quad u_1 = 0 \,, \quad u_{nj} = 0 \tag{3.61c}$$

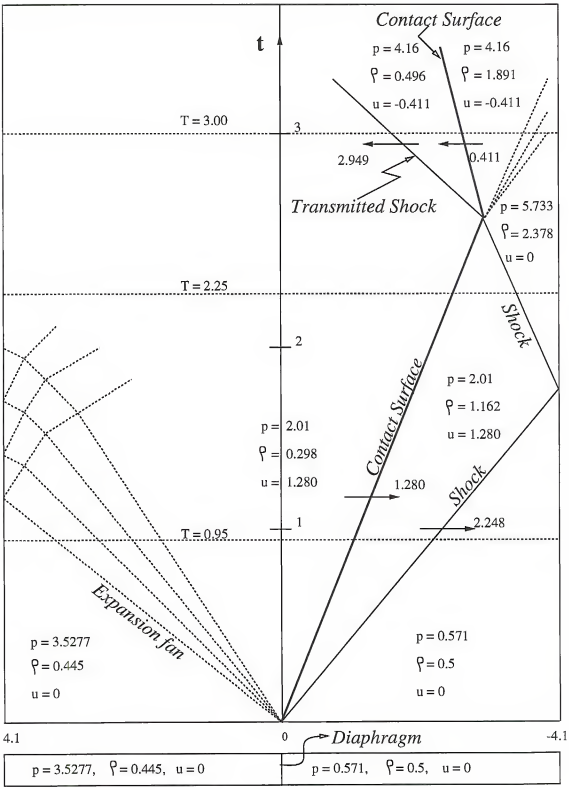

Fig. 3.12. The unsteady shock tube problem: initial state and the exact solution at various time levels (Wang & Widhopf 1989).

where the subscripts denote the grid points used for the numerical calculation, *1* specifying the left boundary and *nj* the right boundary. In the above, first–order extrapolation is used for the gradients to evaluate the pressure and temperature at the boundaries. The density values at the boundaries, ϱ_1 and ϱ_{nj}, are estimated using the equation of state and the total energy values, E_1 and E_{nj}, are computed using T_1 and T_{nj}.

The results are presented in the form of density profiles obtained using the simultaneous and the sequential solvers at times t=0.95, 2.25 and 3.00. The time instant t=0.95 corresponds to a state before the reflection of the shock wave and the expansion wave, time t=2.25 to a state after the reflections from the boundaries but before the interaction among the waves and t=3.00 corresponds to the state after the interaction among the various waves. The exact solution is used as the benchmark as shown in the plots. It has been shown by Wang and Widhopf (1989) that a first–order monotonic scheme such as the Godunov scheme cannot resolve these discontinuities.

Fig. 3.13 shows the density profiles without any artificial compression, using the total number of grid points (*nj*), equal to 83, i.e., Δx=0.1, for both simultaneous and sequential solvers. Although the reflected and the transmitted shock waves, and the contact surface can all be identified by the numerical scheme, exhibiting no overshoots, the profiles are quite smeared near the discontinuities if no artificial compression is used – more so for the sequential solver because a value of δ=0.8 is required to suppress any oscillations whereas a value of δ=0.2 is sufficient for the simultaneous solver. Both the artificial compression methods discussed earlier, namely ACM1 and ACM2 (Eqs. (3.24)–(3.27)), have been implemented; ACM2 appears to perform better and the results obtained by using it will be presented. Here a value of ε=0.05 in Eq. (3.59) is used. Fig. 3.14 compares the effect of ACM2 for both simultaneous and sequential solvers using twice the spatial resolution compared to the previous case, namely, *nj*=165. Fig. 3.14(a) shows the density profiles without using artificial compression, exhibiting the profiles that are less smeared, for both the simultaneous and thesequential cases, compared to the profiles obtained on the coarser

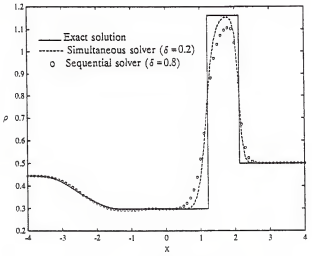

i) t = 0.95

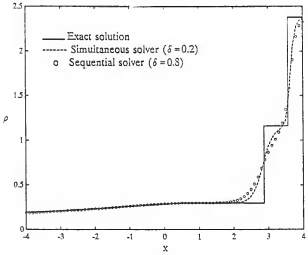

ii) t = 2.25

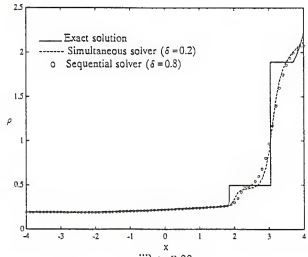

iii) t = 3.00

Fig. 3.13. Density profiles for the unsteady shock tube problem at various time levels for nj=83, without artificial compression.

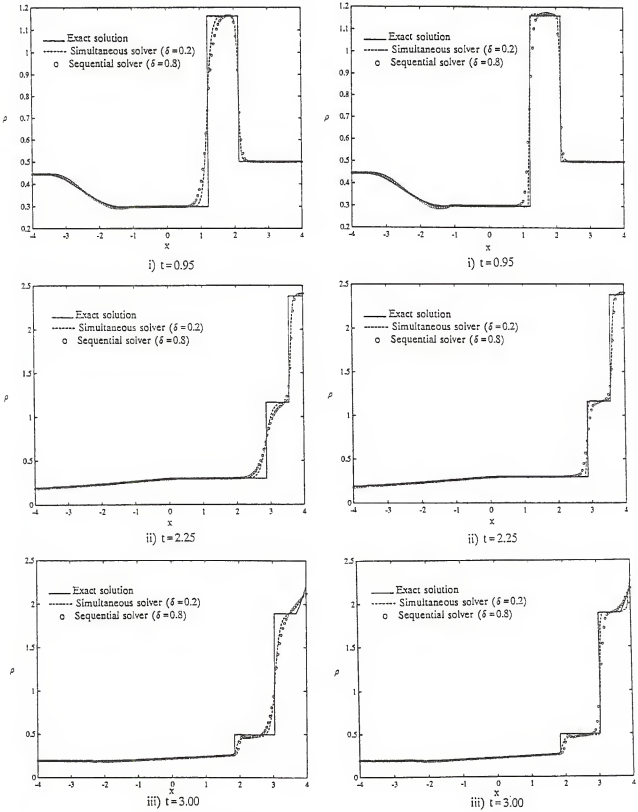

(a) Without artificial compression. (b) With artificial compression method ACM2.

Fig. 3.14. Density profiles for the unsteady shock tube problem at various time levels for nj=165.

grid (Fig. 3.13). The resolution of the solution profiles is further increased when we apply artificial compression with nj=165, as seen in Fig. 3.14(b) which shows results obtained using ACM2. Thus refining the grid coupled with an application of artificial compression yields good resolution of discontinuities in the solution. Overall, for the present test problem, the sequential solver yields profiles which are more smeared than those obtained by the simultaneous solver due to an inherent necessity of higher dissipation, compared to the simultaneous solver, to suppress spurious oscillations.

3.5. The Resonant Pipe Problem

The third case used here to test the efficacy of TVD schemes within a sequential solution framework is the so–called resonant tube problem. The system consists of a one–dimensional tube closed at both ends and filled with an ideal gas. The equations that govern the flow in this system are the Euler equations of gas dynamics. These equations are relevant to the flow in a uniform cross–section area propulsive duct and thus this problem serves as a benchmark for studying combustion instabilities. The phenomenon of interest is the nonlinear evolution of gas dynamics of the system subject to an initial smooth pressure wave disturbance. It is important to correctly model and understand such nonlinear acoustic phenomenon since any initial disturbance in the system may interact with the combustion processes and may lead to instabilities. The resonant tube flow problem tests whether the shock capturing schemes can preserve the high–frequency content of the wave forms, be relatively non–dispersive and non–dissipative up to many wave cycles, and capture discontinuities without generating any overshoots.

The problem involves an initially smooth sinusoidal pressure wave; since the wave crests have the sound speed larger than the troughs, a shock is formed after some time. Subsequently, the amplitude of the shocked N–wave decays due to a loss of energy by entropy production across the shock and eventually the N–wave becomes a smooth wave.

The flow parameters and the initial conditions specified in the tube of length 1 meter are as follows. The ratio of specific heats for the fluid in the tube is γ=1.236 and c_p=0.3727. The mean pressure p_o and temperature T_o are 40 atm. and 2800 K, respectively. The initial pressure disturbance in the stagnant fluid (u=0) is a full cosine wave with an amplitude $1.2p_o$. The initial density and energy perturbations are calculated using isentropic relations. The time is non–dimensionalized using the initial sound speed $c_0 = \sqrt{\gamma p_0/\varrho_0}$ and the length of the tube. The boundary conditions are the same as described by Eqs. (3.61a–c).

The simultaneous and the various sequential solution approaches are employed to solve the resonant tube problem, using Harten's second–order TVD scheme. Fig. 3.15(a) shows the variation of pressure at the boundary with time using the simultaneous solver without any artificial compression, employing δ=0 and λ=0.01 (which corresponds to a CFL number of about 0.2). The pressure variation at the boundary using δ=0, with artificial compression, is plotted in Fig. 3.15(b). The TVD scheme in the simultaneous solver captures the N–wave formation quite effectively, exhibiting no overshoots for all the values of λ corresponding to CFL numbers up to 0.9. Moreover, a small amount of dissipation (δ=0), is sufficient to suppress any spurious oscillation in the solution profile.

Next we present the results obtained using the sequential solution approaches. Unlike the standard shock tube case discussed in Section 3.3, for this problem, results obtained with or without special source term treatment yield qualitatively similar results. The plots shown are the results obtained using special source term treatment as described in Eq. (3.58). The high accuracy convection scheme implemented in the sequential solver is able to capture all the features of the solution obtained using the simultaneous solver but the sequential approach is effective for this problem up to smaller CFL numbers and necessitates a higher amount of dissipation. The solution becomes unstable for values of λ greater than 0.01 (CFL numbers greater than 0.2) irrespective of the amount of dissipation in the scheme. This can be seen in Fig. 3.16(a) which shows instability in the pressure variation at the boundary as time increases, for λ=0.02 (which corresponds to a CFL number about 0.4) and δ=1 (the highest

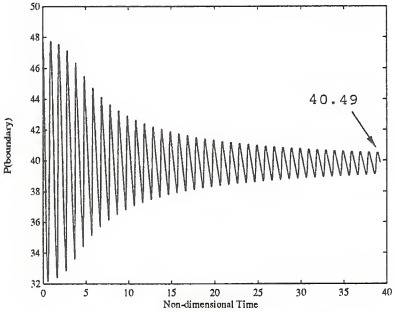

(a) Without artificial compression.

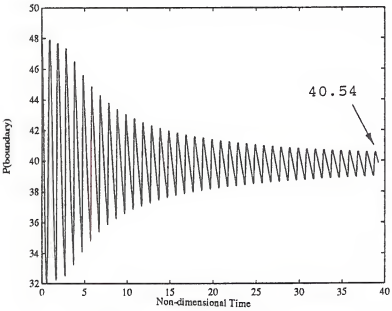

(b) With artificial compression method ACM2.

Fig. 3.15. The resonant pipe problem: pressure variation at the boundary using the simultaneous solver.

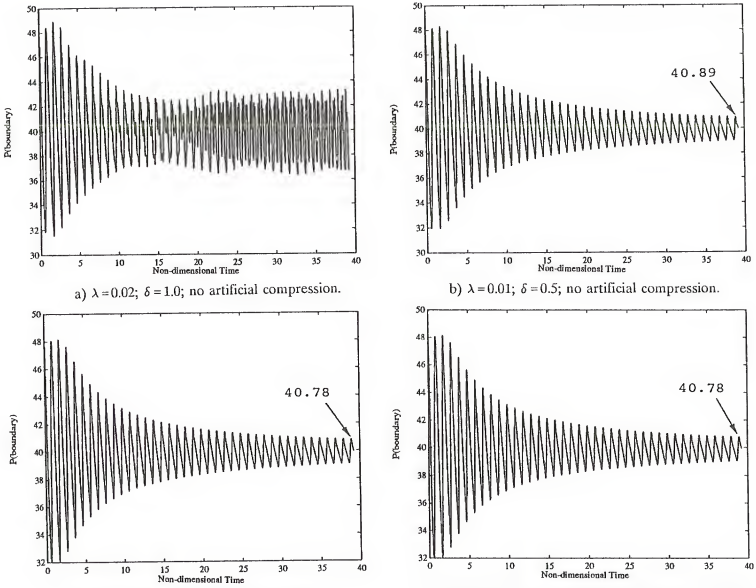

a) $\lambda = 0.02$; $\delta = 1.0$; no artificial compression.

b) $\lambda = 0.01$; $\delta = 0.5$; no artificial compression.

c) $\lambda = 0.01$; $\delta = 0.8$; no artificial compression.

d) $\lambda = 0.01$; $\delta = 0.8$ with artificial compression - ACM2.

Fig. 3.16. The resonant pipe problem: pressure variation at the boundary using the sequential solver.

amount of allowable dissipation). To obtain a stable solution, we have to assign a lower CFL number, about 0.2 (λ=0.01). But with this value of λ we observe spurious wave numbers in the solution for low to moderate amount of dissipation, i.e., for δ up to 0.5, as seen in Fig. 3.16(b). Using δ=0.5, we see spurious oscillations at large time and as the value of δ is decreased, the onset of these oscillations occurs earlier and their magnitudes are larger. Similar observations can be made for the other sequential solution approaches. To achieve an oscillation–free solution that satisfactorily captures the evolution of the nonlinear gas dynamics of the system, we have to employ a higher amount of dissipation, namely δ=0.8, as seen in Fig. 3.16(c). The application of artificial compression using Eq. (3.26) shows little improvement in the resolution of the shocked N–waves, as seen in Fig. 3.16(d). A summary of results obtained using the sequential solver is given in Table 3.3. It appears that the sequential solver can yield a solution with characteristics similar to that obtained using the simultaneous solver; however, the allowable CFL number is lower than that for the simultaneous solver.

λ	Corresponding CFL number	δ=0.0	δ=0.5	δ=0.8
0.005	0.1	Oscillations	Accurate	Accurate
0.01	0.2	Oscillations	Oscillations at large time	Accurate
0.02	0.4	Blows up	Oscillations	Oscillations

Table 3.3. Summary of results for the resonant pipe problem using the sequential solver.

3.6. Concluding Remarks

The high resolution shock capturing schemes seem to be amenable for application in a sequential solution algorithm for solving Navier–Stokes equations but care must be taken when defining the characteristic speed of the equations to be solved sequentially. A naive extension of the TVD schemes for scalar conservation laws leads to a definition of different characteristic speeds for the different equations in the system. This leads to nonphysical oscillations away from the discontinuities in the solution which has nothing to do with dispersion in the TVD schemes but rather with nonphysical specification of characteristic propagation speeds. In our context, the convection speed should be specified as the characteristic speed and the pressure terms should be treated as source terms. Proper handling of these source terms is required to maintain the accuracy of the high resolution schemes and thus eliminate oscillations in solution profiles. A useful approach is to selectively increase the amount of dissipation near the discontinuities in order to avoid the oscillations near the shock and to avoid smearing of the overall profile at the same time.

As seen from the results of the unsteady shock tube problem and the resonant pipe problem, the TVD type convection scheme in a sequential solution framework is capable of resolving discontinuities in unsteady flows involving complex gas dynamics. Furthermore, it is established that the numerical damping term originally designed to help satisfy the entropy condition, Eq. (3.2), plays a different role in the sequential solver. With an adequate source term treatment, the sequential solver produces solutions of accuracy comparable to those obtained with the simultaneous solver, indicating that even without resorting to an explicit flux splitting technique, satisfactory performance can be obtained from a sequential solver. The use of artificial compression techniques can further improve the gradient resolution capabilities of both simultaneous and sequential solvers. An automatic switch, based on the gradients of density, is used to identify the location of discontinuities in the flowfield (where artificial compression is needed) in the sequential solver. The unsteady shock tube problem results illustrate that for the complex flowfield resulting from the

interaction of shock waves, contact surfaces and expansion waves with solid boundaries and with each other, the sequential solver smears the solution profiles somewhat more than the simultaneous solver. The results of the resonant pipe problem demonstrate that the sequential solver can yield a solution of accuracy comparable to that obtained using a simultaneous solver exhibiting good resolution of the shocked N–waves and retaining all the essential features of the gas dynamics of the system, though the maximum allowable CFL number is lower than that for the simultaneous solver.

CHAPTER IV
TREATMENT OF SOURCE TERMS: A LONGITUDINAL COMBUSTION INSTABILITY PROBLEM

4.1. Background

The previous two chapters have attempted to address some issues related to the treatment of convection terms. For many flow problems, the difficulty encountered by the convection scheme is further compounded by the presence of source terms. Special techniques for treating source terms along with a high–accuracy convection treatment based on Harten's second–order TVD scheme, within the framework of a sequential algorithm, have been discussed in Chapter III. The source terms encountered in the test cases studied in Chapter III were not a result of any physical mechanism but instead arose due to the nature of the sequential algorithm which treats the pressure gradient terms as source terms. It would be very desirable to assess the performance of the high accuracy source term treatment discussed in Chapter III in conjunction with the high accuracy convection treatment for a coupled system of equations governing an unsteady fluid flow with strong source terms due to some physical process, e.g., combustion. In the present chapter, an effort is made to do so by solving a one–dimensional reacting flow, subject to a thermo–acoustic longitudinal combustion instability, which has heat release terms as the dominant source terms.

As mentioned in Chapter I, the intent here is by no means to resolve the complex physics associated with the combustion instability phenomenon. Instead this physical problem is used here to illustrate the numerical difficulties that stiff source terms can cause and to demonstrate the utility of special source term treatments within the framework of the high accuracy sequential solver developed in Chapter III. With this objective in mind, only a

brief background of the physics associated with the combustion instability phenomenon is presented next.

The combustion instability phenomenon has been studied for a long time by many researchers. It involves pressure oscillations which are self–sustained, in the absence of any external forcing, during combustion processes, e.g., in combustors or afterburners. Rayleigh (1945) advanced a criterion for sustenance of pressure oscillations, according to which the oscillations are driven if they are in phase with the heat release oscillations. It is generally known that the main mechanisms of combustion instability are thermo–acoustic and vortical in nature; it is the thermo–acoustic aspect that is being focused here.

Shyy *et al.* (1992a) and Mittal (1991) have developed a one–dimensional computational model to simulate the phenomenon of longitudinal combustion instability involving low frequency, large amplitude oscillations. The heat release model they have chosen relates the heat fluctuations at the gutter (flameholder) location to the velocity fluctuations and is based on experimental observations of Langhorne (1985) and the study by Bloxidge *et al.* (1985). Though this one–dimensional model is unable to capture the shear layer instability and vortex formation, which are essential features of a multidimensional combustion instability, it provides useful insight into the thermo–acoustic phenomena associated with the instability. Moreover, this model is simple enough not to require prohibitively large amount of computer time.

Another issue of interest in the present study is the investigation of an active control strategy, in order to attenuate or enhance the magnitudes of the oscillations associated with the combustion instability, depending on the desired application. For instance, in pulse combustor applications, it is desirable to maintain these oscillations at a large amplitude, without any external excitation. On the other hand, for systems like ramjet combustors and jet engine afterburners, the oscillations associated with combustion instability can deteriorate the engine performance and may even cause damage to the mechanical structure, and hence must be attenuated as much as possible. As is well known (Chu 1964), the modes

of feeding energy into the system in order to sustain the combustion instability involve the pressure–mass flux coupling and the pressure–heat release coupling. An active control strategy seeks to dynamically adjust either the pressure field, the heat addition or the mass flux. One form of active control strives to affect the oscillations in the system by manipulating the heat fluctuations through controlled fuel injection (Shyy & Udaykumar 1990, Langhorne *et al.* 1990, Wilson *et al.* 1991, Menon 1991). This is the form of active control employed in the present study, as will be described later.

The numerical studies by Shyy & Udaykumar (1990) and Shyy *et al.* (1992a) use the first–order upwind scheme with the aid of a nonlinear filtering scheme (Engquist *et al.* 1989) to approximate the convection terms in the governing equations. Their algorithm does not utilize the concept of flux splitting and hence, in the absence of numerical oscillations, is expected to yield solutions more accurate than the first–order upwind scheme based on flux splitting. Nevertheless, the solution profiles obtained in their study are expected to be smeared since there is no explicit control of numerical viscosity. It has been demonstrated in Chapter III that a high solution accuracy can be achieved in a sequential solution approach, by using a TVD scheme to approximate the convection terms. This technique is extended now to simulate the combustion model developed by Shyy & Udaykumar (1990). This problem involves source terms, due to the chemical heat release, which have a substantial magnitude. In Chapter III, the issue of source terms is mainly caused by the formulation of the sequential solution technique. In the present chapter, an extra heat transport equation is incorporated into the system to model the heat release; it not only gives one more equation to solve but also supplies a significant source term to the energy equation, which is the dominant source term in the system. It is seen that a special source term treatment accompanied by a low level of dissipation in the scheme yields high solution accuracy, exhibiting substantially higher magnitudes in the profiles compared with the studies by Shyy & Udaykumar (1990) and Shyy *et al.* (1992a).

4.2. Basic Equations for the Combustion Instability Problem

In the following, the basic governing equations and the equations used to model the heat release terms are presented. The equations governing the system are the continuity, momentum and energy equations, respectively:

$$\frac{\partial \varrho}{\partial t} + \frac{\partial (\varrho u)}{\partial x} = 0 \tag{4.1a}$$

$$\frac{\partial m}{\partial t} + \frac{\partial (mu)}{\partial x} = -\frac{\partial p}{\partial x} + \frac{1}{\mathrm{Re}_\infty}\frac{\partial \tau_{11}}{\partial x} \tag{4.1b}$$

$$\frac{\partial E}{\partial t} + \frac{\partial (Eu)}{\partial x} = -\frac{\partial (pu)}{\partial x} + \frac{1}{\mathrm{Re}_\infty}\left[\frac{1}{\mathrm{Pr}_\infty}\frac{\partial}{\partial x}\left(\frac{\partial h}{\partial x}\right) + \frac{\partial}{\partial x}(u\tau_{11})\right] + Q(x,t) \tag{4.1c}$$

with

$$p = (\gamma - 1)\left(E - \frac{1}{2}\varrho u^2\right) \tag{4.2a}$$

$$h = \frac{\gamma}{\gamma - 1}\left(\frac{p}{\varrho}\right) \tag{4.2b}$$

$$\tau_{11} = \frac{4}{3}\mu\left(\frac{\partial u}{\partial x}\right) \tag{4.2c}$$

where u, ϱ, $m(=\varrho u)$, E, p and Q are, respectively, the non–dimensional velocity, density, momentum, total energy, pressure and heat release. These quantities are non–dimensionalized using inlet velocity, density (1.22 kg/m^3) and temperature (288K). Re_∞ and Pr_∞ are the Reynolds and Prandtl numbers, respectively, based on the above reference values.

The heat release profile in the combustor of length L with the gutter location x_g, is specified as

$$Q = q_{av} + q' \tag{4.3}$$

where q_{av} is the mean heat release specified as a linear function with respect to the distance from the gutter location (Shyy & Udaykumar 1990, Langhorne 1985, Bloxidge *et al.* 1985):

$$q_{av}(x) = \begin{cases} 0 & x < x_g \\ C_1(x - x_g) & x_g \leq x \leq L \end{cases} \tag{4.4}$$

and q' is the unsteady heat release specified as

$$q'(x,t) = q^*(x,t).q_{av}(x) \tag{4.5}$$

where $q^*(x,t)$ is the perturbation coefficient for the unsteady heat release and according to the empirical observations of Langhorne (1985), it is related to the fluctuating velocity at the gutter by a phase factor τ_c, corresponding to the combustion time delay, as follows:

$$q^*(x_g,t) = C_2.u'(x_g, t - \tau_c) \tag{4.6}$$

Downstream of the gutter, the unsteady heat release is assumed to be transported by local convection; thus we can write:

$$q_t^* + u(x,t)q_x^* = 0 \tag{4.7}$$

The inlet boundary condition is the pressure reflection condition:

$$(p_x)_1 = 0, \quad u_1 = 1, \quad \varrho_1 = 1 \tag{4.8}$$

where the subscript 1 represents the grid point on the inlet boundary; the exit pressure is taken to be the same as the ambient pressure and the other variables are calculated by a linear extrapolation of the interior values, as follows:

$$p_n = p_\infty \ , \qquad u_n = 2u_{n-1} - u_{n-2} \ , \qquad \varrho_n = 2\varrho_{n-1} - \varrho_{n-2} \tag{4.9}$$

Here the subscript n represents the grid point on the exit boundary.

4.3. Numerical Scheme and the Treatment of Source Terms

The TVD type sequential solver developed in Section 3.3.2 of Chapter III is employed to solve the governing equations. As discussed in Chapter III, when the source terms become too stiff they may cause numerical instabilities and lead to spurious oscillations in the numerical solution. This can be rectified by treating the source terms in a special manner, e.g., by employing MacCormack's predictor–corrector method or Strang's

time–splitting method which have been discussed in Section 3.3.2. In the present combustion instability problem, the source terms corresponding to the momentum equation are

$$\psi(m) = -\frac{\partial p}{\partial x} + \frac{1}{\mathrm{Re}_\infty}\frac{\partial \tau_{11}}{\partial x} \tag{4.10}$$

and those corresponding to the energy equation are

$$\psi(E) = -\frac{\partial(pu)}{\partial x} + \frac{1}{\mathrm{Re}_\infty}\left[\frac{1}{\mathrm{Pr}_\infty}\frac{\partial}{\partial x}\left(\frac{\partial h}{\partial x}\right) + \frac{\partial}{\partial x}(u\tau_{11})\right] + Q(x,t) \tag{4.11}$$

For the present case, we employ Strang's time–splitting method, described by Eqs. (3.58a–c) in Chapter III, to treat the source terms which include the heat release terms. ψ' denotes the first derivative of the source terms ψ, in equations (4.10) and (4.11), with respect to the independent variable w. For the momentum equation, we have

$$\psi'(m) = \frac{\partial \psi}{\partial m}(m) = (\gamma - 1)\frac{\partial u}{\partial x} + \frac{4}{3}\frac{\mu}{\mathrm{Re}_\infty}\left[\frac{\partial^2}{\partial x^2}(1/\varrho)\right] \tag{4.12}$$

and for the energy equation, we have

$$\psi'(E) = \frac{\partial \psi}{\partial E}(E) = -(\gamma - 1)\frac{\partial u}{\partial x} + \frac{\gamma}{\mathrm{Re}_\infty \,.\, \mathrm{Pr}_\infty}\left[\frac{\partial^2}{\partial x^2}(1/\varrho)\right] \tag{4.13}$$

The last two source terms in the energy equation (4.1c) do not contribute to ψ' since they are independent of E.

4.4. Application of Active Control

As mentioned earlier, the form of feedback type of active control being investigated here seeks to affect the oscillations associated with the combustion instability by adjusting the fuel injection, i.e., the inlet mass flux. The numerical implementation of this strategy involves the adjustment of the inlet velocity as shown below:

$$u_{inlet}(t) = 1 + u'(t) \tag{4.14}$$

where the magnitude of the initially specified constant inlet velocity is 1. Here u' is the

additional velocity needed to affect active control and is computed from a phase–shifted, amplified pressure signal sensed at the gutter, as follows

$$u'(t) = G\left[\frac{P_s(t-\tau_f) - P_r}{P_r}\right] \tag{4.15}$$

where

G = gain of feedback

P_s = sensed pressure signal at the gutter

P_r = reference pressure

τ_f = time–lag in feedback.

In the above, the reference pressure, P_r, is taken to be the time–averaged pressure at the gutter location and is continually updated after each cycle. The range of variation of τ_f is 0 to t_p where t_p is the time period of the dominant frequency of the oscillations before the application of active control, and accordingly a phase lag in the feedback can be defined as

$$\phi_f = 2\pi\left(\frac{\tau_f}{t_p}\right) \tag{4.16}$$

4.5. Results

The values of the various parameters used in the system are: L=1.0, x_g=0.5, M_∞=0.38, Re_∞=10^4, Pr_∞=0.7, C_1=350, and C_2=1. A total of 401 grid points are used with λ=0.03.

4.5.1. Simulation of Combustion Instability

The simulation is initiated by specifying uniform conditions along the entire length of the combustor and a linear average heat release profile. When the system has reached a steady state, the linear heat release profile is perturbed for a few timesteps. At the same instant the gutter velocity–heat release coupling is also initiated. The computations are then carried on for 2x10^6 timesteps. For the last 10^4 timesteps of the computation, mode shapes of

pressure with respect to the steady state pressure, temperature and total heat release are plotted after every 300 timesteps, for a total of ten mode shapes. Also plotted are the pressure fluctuations at the gutter for the last 5×10^4 timesteps as well as the Fourier spectra of the pressure oscillations showing the fundamental frequency and its harmonics. The various plots in Figs. 4.1–4.4 compare and contrast the performance of the first–order upwind scheme used in the studies by Shyy & Udaykumar (1990), Shyy *et al.* (1992a) and Mittal (1991) and the TVD type sequential solver described in Chapter III, with and without source term treatment and using different values of δ. Fig. 4.1 shows the plots obtained by the first–order upwind scheme and Fig. 4.2 shows those obtained using the TVD type sequential solver with no special source term treatment and using δ=0, which corresponds to the least amount of dissipation in the scheme. The pressure mode shapes and the temperature mode shapes at ten different time instants, shown in plots (a) and (b), respectively, of Figs. 4.1 and 4.2, clearly show the travelling wave pattern of the flow variables; the entropy waves are propagated at speeds of the range of local convection speeds, which are much less than the acoustic speeds of propagation of the pressure waves. The time series of the pressure oscillations at the gutter and the Fourier spectra of the pressure oscillations clearly indicate the presence of the dominant frequency and its harmonics. The first–order upwind scheme, being very diffusive, smears out the solution profiles as seen by a comparison of the magnitudes of the mode shapes, the pressure oscillations and the fundamental frequency and its harmonics, shown in Figs. 4.1 and 4.2. However, the various frequencies of the harmonics predicted by both the schemes are very close, confirming the viewpoint taken in the previous studies (Shyy & Udaykumar 1990, Shyy *et al.* 1992a) that while a diffusive scheme has a substantial impact on the magnitudes of the oscillations, its effect on the predicted frequencies is small. Furthermore, although the present TVD type sequential solver yields solution profiles with much better resolution, it exhibits some high frequency oscillations as can be observed along the last quarter length of the combustor, in some of the mode shapes, namely mode shapes numbered 5, 6 and 7 for both pressure and temperature. It is noted that

in Fig. 4.2(c), the heat release at the time instants corresponding to the curves 5, 6 and 7 are of the highest levels. Based on this observation and the results to be presented in the following, it is concluded that these oscillations are spurious (nonphysical or numerical) in nature and are due to a lack of dissipation in the numerical scheme accompanied by stiffness of the source terms in the governing equations.

Results presented in Fig. 4.3 using no source term treatment in the TVD type scheme and δ=0.8, which corresponds to a higher level of dissipation in the scheme, do not exhibit oscillations in any of the mode shapes of pressure and temperature, indicating that the high frequency oscillations seen in Fig. 4.2 are indeed spurious in nature and are a manifestation of the low level of numerical dissipation in the scheme. However, the suppression of the spurious oscillations in Fig. 4.3 is at the cost of a slight smearing in the solution profiles which is reflected in the lower magnitudes of the solution profiles, e.g., the pressure and temperature mode shapes and the pressure fluctuations at the gutter (the solution profiles are qualitatively the same as in Fig. 4.2). Ideally, it is desirable to eliminate spurious oscillations in the solution while maintaining a high resolution of the profiles by employing a low level of dissipation. Special source term treatment is a means to do just that. As seen in Fig. 4.4, special source term treatment, with δ=0, which is the lowest amount of damping in the numerical scheme, eliminates the spurious oscillations while maintaining the same magnitude of the fluctuations as observed in Fig. 4.2.

It must be noted that, although the four cases shown in Figs. 4.1–4.4 yield qualitatively similar results, the phase of the fluctuations is not identical among them, as is evident from the time series of the pressure fluctuations and the sequencing of the mode shapes. But this difference in phase is not very substantial and it can be seen from the frequency spectra in plots (e) and tables (f) in Figs. 4.1–4.4 that the value of the fundamental frequency remains unchanged for all the three cases using the TVD scheme though it is slightly different from that obtained using the first–order upwind scheme. The harmonics of

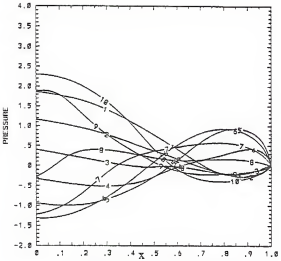

(a) Pressure Mode Shapes

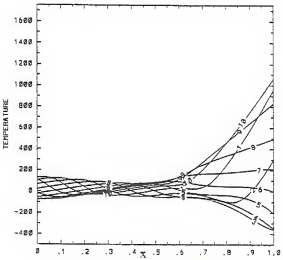

(b) Temperature Mode Shapes

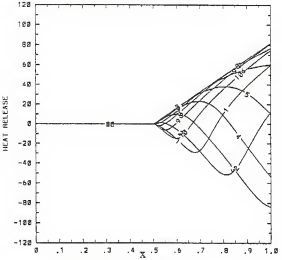

(c) Heat Release Mode Shapes

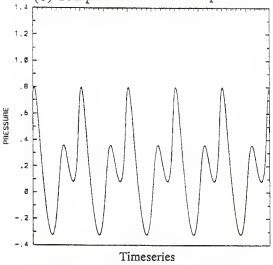

(d) Pressure Fluctuations at Gutter

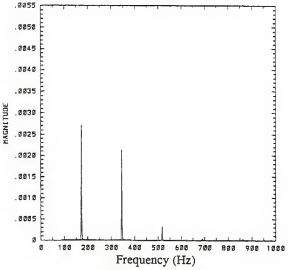

(e) Fourier Spectra

Harmonic	Frequency (Hz.)	Magnitude
Fundamental	172.934	2.702×10^{-3}
First	344.367	2.127×10^{-3}
Second	517.302	0.313×10^{-3}
Third	690.237	0.036×10^{-3}
Fourth	861.669	0.031×10^{-3}

(f) Frequencies in Fourier Spectra

Fig. 4.1. Longitudinal combustion instability: Results obtained using the first–order upwind scheme.

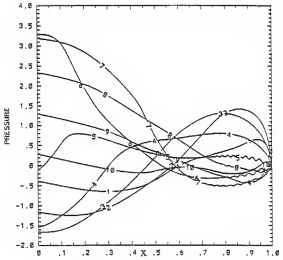

(a) Pressure Mode Shapes

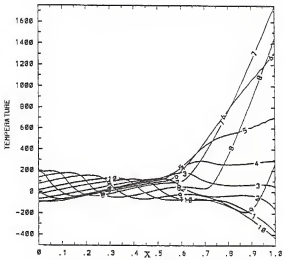

(b) Temperature Mode Shapes

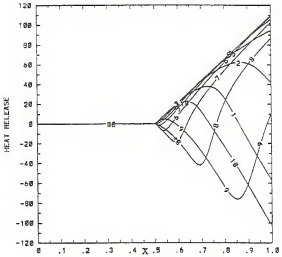

(c) Heat Release Mode Shapes

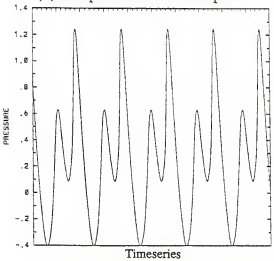

(d) Pressure Fluctuations at Gutter

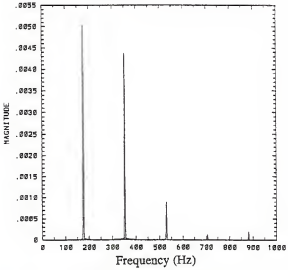

(e) Fourier Spectra

Harmonic	Frequency (Hz.)	Magnitude
Fundamental	175.943	5.025×10^{-3}
First	351.886	4.369×10^{-3}
Second	529.332	0.884×10^{-3}
Third	705.275	0.118×10^{-3}
Fourth	881.218	0.182×10^{-3}

(f) Frequencies in Fourier Spectra

Fig. 4.2. Longitudinal combustion instability: Results obtained using the TVD type sequential solver with no source term treatment and $\delta = 0$.

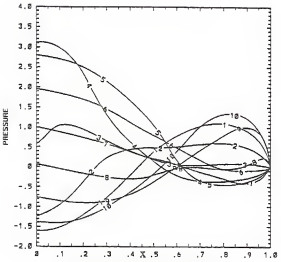

(a) Pressure Mode Shapes

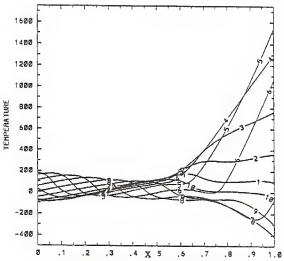

(b) Temperature Mode Shapes

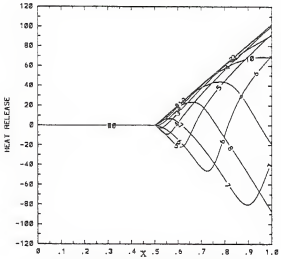

(c) Heat Release Mode Shapes

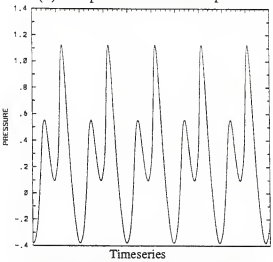

(d) Pressure Fluctuations at Gutter

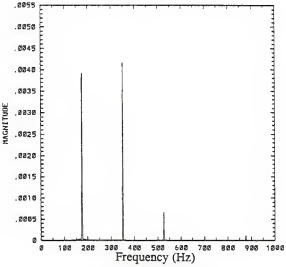

(e) Fourier Spectra

Harmonic	Frequency (Hz.)	Magnitude
Fundamental	175.943	3.908×10^{-3}
First	350.382	4.154×10^{-3}
Second	526.325	0.652×10^{-3}
Third	700.764	0.083×10^{-3}
Fourth	876.707	0.109×10^{-3}

(f) Frequencies in Fourier Spectra

Fig. 4.3. Longitudinal combustion instability: Results obtained using the TVD type sequential solver with no source term treatment and $\delta = 0.8$.

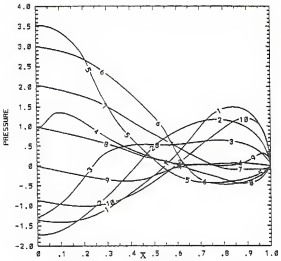

(a) Pressure Mode Shapes

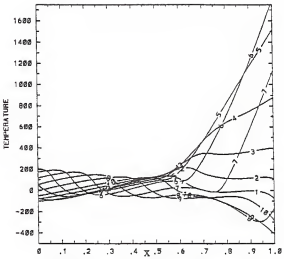

(b) Temperature Mode Shapes

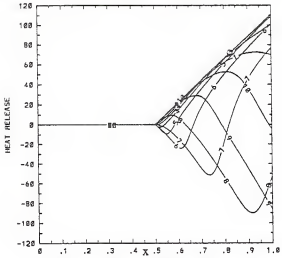

(c) Heat Release Mode Shapes

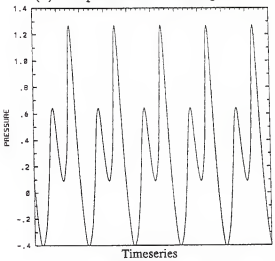

(d) Pressure Fluctuations at Gutter

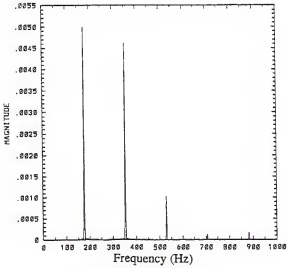

(e) Fourier Spectra

Harmonic	Frequency (Hz.)	Magnitude
Fundamental	175.943	4.983×10^{-3}
First	353.389	4.609×10^{-3}
Second	529.332	1.018×10^{-3}
Third	705.275	0.118×10^{-3}
Fourth	882.722	0.158×10^{-3}

(f) Frequencies in Fourier Spectra

Fig. 4.4. Longitudinal combustion instability: Results obtained using the TVD type sequential solver with special source term treatment (Strang's time–splitting method) and $\delta = 0$.

the fundamental frequency for all the cases are slightly different, though very close to each other.

According to the generalized Rayleigh criterion, the only modes of feeding energy to sustain the instability are the pressure–mass flux and pressure–heat release couplings (in the absence of body forces). As already pointed out, spurious oscillations observed in Fig. 4.2 occur primarily in modes numbered 5, 6 and 7 of the pressure and temperature mode shapes. These mode numbers correspond to the modes of maximum heat release, shown in Fig. 4.2(c). The heat release is the dominant driving source term in the system and it seems that for modes numbered 5, 6 and 7 in Fig. 4.2, the heat release source term assumes a magnitude large enough to cause spurious oscillations in the pressure and temperature mode shapes. Thus, special source term treatment which is effective only in the presence of sufficiently strong source terms seems to be necessary in order to suppress the spurious oscillations in these mode shapes, which are modes numbered 3, 4 and 5 in Fig. 4.4 in contrast to modes 5, 6 and 7 in Fig. 4.2 due to the slight phase difference among the various cases mentioned before. The above observation is reinforced from the plots of pressure and heat release fluctuations, shown in Fig. 4.5, at a location very near the exit, namely x=0.9375. This location is chosen due to the observation that in Fig. 4.2, the spurious oscillations in the mode shapes occur in a region near the right boundary of the combustor. Thus, a location near the exit is more likely to exhibit spurious oscillations in the pressure–time history plots, compared to the gutter location. For δ=0, a lack of special source term treatment leads to spurious oscillations in the pressure fluctuations, as seen in Fig. 4.5(a), the occurrences of which correspond to the occurrences of maxima in the heat release profile which are also shown in Fig. 4.5(a). The application of special source term treatment for δ=0 leads to an elimination of these spurious oscillations, as seen from Fig. 4.5(b). It should be noted that the phase relationships between the pressure fluctuations and the heat release fluctuations are virtually the same for the two cases– –with and without source term treatment– –shown in Fig. 4.5 and hence the

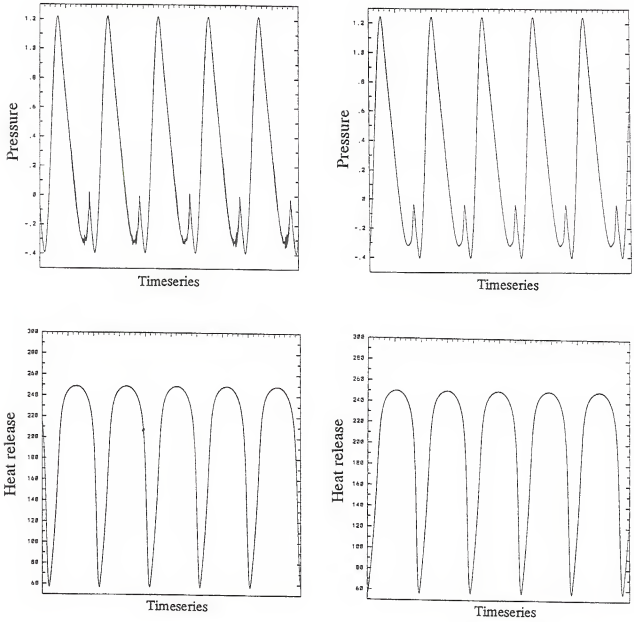

(a) Without source term treatment.

(b) With source term treatment.

Fig. 4.5. Pressure and heat release oscillations at x=0.9375, for the last 5×10^4 time steps, using the TVD type sequential solver; $\delta = 0$.

suppression of the spurious oscillations is due entirely to the special numerical source term treatment, and not due to a physical phase shift between the pressure and heat fluctuations.

4.5.2. Active Control of Combustion Instability

As mentioned earlier, active control is turned on after the oscillations associated with the combustion instability have attained a limiting state, i.e., after $2x10^6$ timesteps. The dominant frequency of the system is calculated which, for the case of source term treatment with δ=0, shown in Fig. 4.4, is 175.9 Hz. Active control is put into effect by employing Eqs. (4.14) and (4.15) where τ_f, the time–lag in feedback varies from 0 to t_p, the time period associated with the above mentioned dominant frequency. The phase–lag ϕ_f, defined in Eq. (4.16) accordingly varies from 0 to 2π. The computation is carried on for an additional $5x10^4$ timesteps beyond the limiting state achieved before the application of active control, for ten values of ϕ_f, which are equally spaced between 0 to 2π. For each of the ten values of ϕ_f, the mean pressure and the peak–to–peak pressure amplitude are calculated and compared with the values obtained before the control is applied, as a means to assess the effectiveness of active control. These results are presented in Table 4.1. Also, Fig. 4.6 shows the variation of the normalized peak–to–peak pressure variation with the ten phase values used. The amplitudes have been normalized with respect to the peak–to–peak pressure amplitude observed without the application of control. It can be observed that there are preferred values of ϕ_f, for which the oscillations are attenuated, namely, values of ϕ_f between 0.8π and 1.4π. The maximum attenuation occurs for ϕ_f=1.2π, namely, 44% reduction in the peak–to–peak pressure variation compared to the original pressure variation. In order to qualitatively compare the effect of active control, Fig. 4.7 presents the time history of pressure variation as well as selected mode shapes for the cases of (a) no active control, (b) active control with ϕ_f=π and (c) active control with ϕ_f=1.6π. For all the cases shown in Figs. 4.6 and 4.7, the value of G, the gain of the feedback, is 1. It is observed that the oscillations are attenuated for ϕ_f=π and enhanced for ϕ_f=1.6π. Moreover, the relative magnitudes of the originally

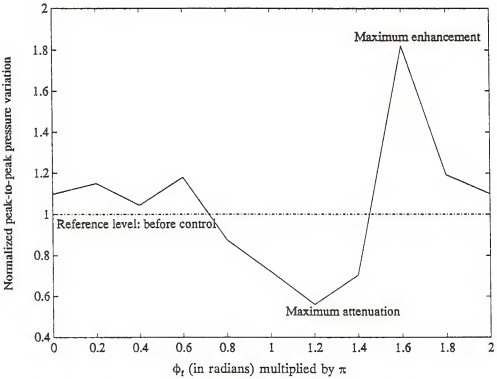

Fig. 4.6. Normalized peak–to–peak pressure variation with phase lag ϕ_f.

Number	Phase lag	Mean Pressure	Peak to Peak	% Reduction
Before Control		7.9378	0.21102	
1	0	8.0748	0.23185	- 9.86
2	0.2π	7.9958	0.24278	-15.05
3	0.4π	7.9533	0.22038	- 4.33
4	0.6π	7.9654	0.24896	-17.97
5	0.8π	7.9066	0.18492	12.36
6	1.0π	7.8440	0.15225	27.85
7	1.2π	7.7916	0.11814	44.01
8	1.4π	7.7837	0.14872	29.52
9	1.6π	7.8951	0.38406	-81.9
10	1.8π	8.0395	0.25166	-19.25

Table 4.1. Values of mean pressure, peak–to–peak pressure amplitude and the percentage reduction in the peak–to–peak amplitudes with respect to that before application of active control, for ten values of phase lag ϕ_f.

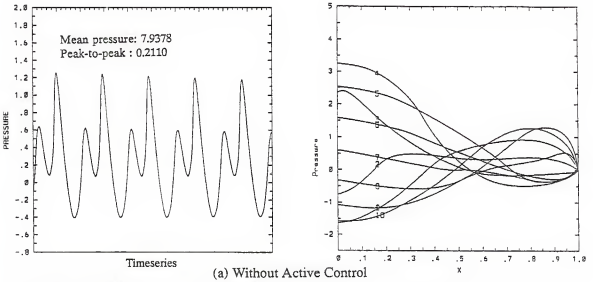

(a) Without Active Control

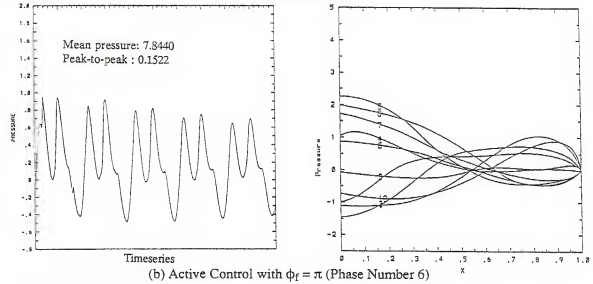

(b) Active Control with $\phi_f = \pi$ (Phase Number 6)

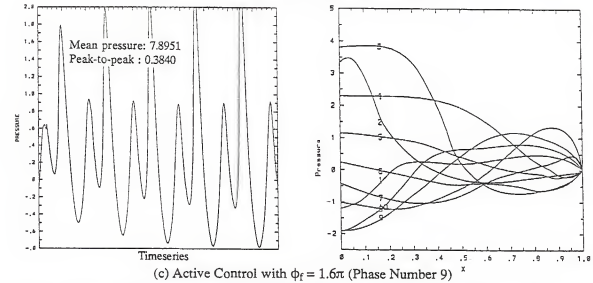

(c) Active Control with $\phi_f = 1.6\pi$ (Phase Number 9)

Fig. 4.7. Pressure fluctuations and mode shapes for three selected cases of active control.

dominant frequency and its first harmonic are different for the two cases. For the other values of ϕ_f, not plotted here, similar observations can be made, with higher harmonics appearing in some cases. Thus, the application of active control changes not only the mean pressure level and the peak–to–peak pressure amplitude but also the qualitative nature of the oscillations.

The case of active control with ϕ_f=1.2π, which shows the maximum attenuation for G=1, is further computed for 5×10^4 timesteps, in order to approach a limiting state of the oscillations, and the results are plotted in Fig. 4.8(b). It can be seen that the oscillations are further attenuated as time elapses, beyond the attenuation achieved for the 5×10^4 timesteps employed initially. The peak to peak pressure amplitude is now 0.0935, which shows that using active control with this particular value of ϕ_f, one can achieve a 55% reduction in the peak–to–peak variation of pressure, compared to the original peak–to–peak pressure variation associated with the combustion instability without any active control.

Next, we investigate the effect of variation of G, the gain of the feedback pressure signal employed to achieve active control. Fig. 4.8(a) shows the results obtained for ϕ_f=1.2π but with G=0.5. The peak–to–peak pressure variation achieved for this case is 0.1371 which amounts to only a 35% reduction compared to the 55% reduction obtained for G=1 case for the same value of ϕ_f. For all values of G between 0 and 1, the maximum attenuation is achieved for G=1. For G=2, however, we achieve further attenuation of the peak to peak pressure amplitude for ϕ_f=1.2π (phase number 7), as shown in Fig. 4.9(a). But, even with special source term treatment along with δ=0, we observe numerical oscillations in the solution profiles; a higher value of δ, namely δ=1, is required to suppress these oscillations, as seen in Fig. 4.9(b). The peak–to–peak pressure magnitude observed in this case is 0.0766 which amounts to a 63% reduction in the original magnitude of the pressure oscillations. However, the variation of pressure is qualitatively very different from the case of G=1, as evident from a comparison of Figs. 4.8(b) and 4.9(b). For the G=2 case, we observe more subharmonics in the oscillations, compared to the G=1 case, resembling chaotic behavior in the system.

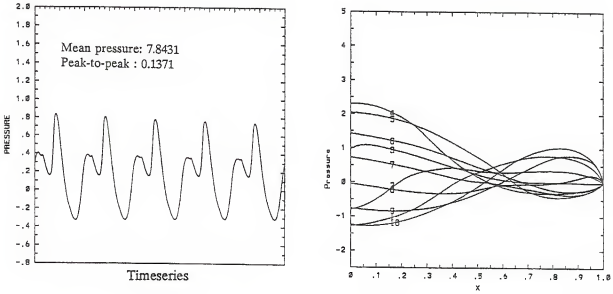

(a) G = 0.5

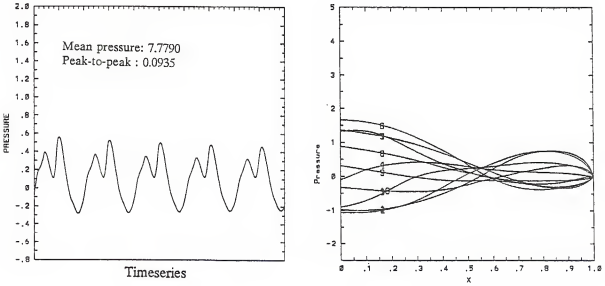

(b) G = 1.0

Fig. 4.8. Pressure fluctuations and mode shapes for active control with $\phi_f = 1.2\ \pi$ (phase number 7), for G=1 and 0.5; $\delta = 0$.

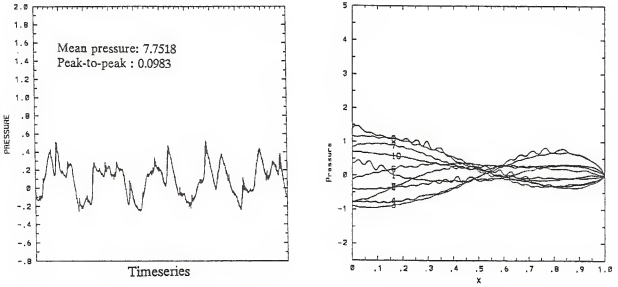

(a) $\delta = 0.0$

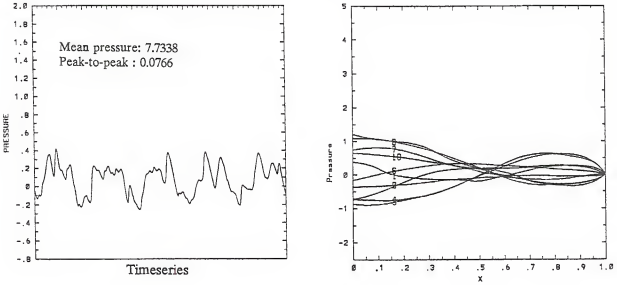

(b) $\delta = 1.0$

Fig. 4.9. Pressure fluctuations and mode shapes for active control with $\phi_f = 1.2\,\pi$ (phase number 7), for G=2 and two values of δ.

4.6. Concluding Remarks

The sequential solver employed here, which uses a scheme in the spirit of the total variation diminishing concept to approximate the governing equations for the combustion instability phenomenon, with characteristic speeds that are coordinated by assigning them as the local convection speeds, yields a substantial improvement in the accuracy of the solution profiles compared with the first–order upwind scheme used by Mittal (1991) and Shyy *et al.* (1992a) in earlier studies. When no special treatment is imparted to the source terms in the governing equations and a low level of dissipation is employed (in the form of δ=0 here), spurious oscillations appear in the solution profiles when the source term, which is predominantly the heat release term in the present study, becomes too stiff. These oscillations can be suppressed by using a higher level of dissipation in the scheme (δ=0.8 in the present case). But this also leads to an overall degradation of the solution in the form of dampened magnitudes of the oscillations associated with the combustion instability. A more desirable way to suppress the oscillations is to treat the source terms in a special manner, for example, by employing Strang's operator splitting method; this allows the use of a low level of dissipation (δ=0) in the scheme, thus avoiding a smearing of the solution profiles, while eliminating the nonphysical oscillations. Overall, it is concluded that a high accuracy TVD–based sequential solver along with a special source term treatment can yield satisfactory results for complex physical problems that possess stiff source terms.

CHAPTER V
A CONTROLLED VARIATION SCHEME FOR MULTI–DIMENSIONAL RECIRCULATING FLOWS

5.1 Background

So far, we have addressed the issues of convection and source term treatments in quite a bit of detail. Two approaches for numerically approximating convection terms have been described in previous chapters, namely,

(a) utilizing various geometric shape functions to estimate the fluxes at control volume interfaces leading to the first–order upwind, central difference, second–order upwind and QUICK schemes, as discussed in Chapter II, and

(b) introducing an appropriate amount of nonlinear dissipation into the central difference scheme, which is the essence of the sequential algorithm based on Harten's TVD scheme, discussed in Chapter III.

The former approach was investigated (in Chapter II) within the framework of the multidimensional pressure–based sequential algorithm. The latter approach, however, has so far been developed (in Chapters III and IV) only for one–dimensional Euler and Navier–Stokes equations. In this chapter, we attempt to explore this approach for application to multi–dimensional Navier–Stokes equations, within the context of the sequential pressure–based algorithm, already introduced in Chapter II. First, some issues, related to the extension of schemes based on the TVD concept into pressure–based algorithms, are outlined.

It has been shown in Chapter III that one can formally implement the original TVD schemes in sequential solvers in an effective manner by devising an appropriate framework.

From the insight gained from the one–dimensional cases, it has been established that in order to coordinate the speed of signal propagation for the system of equations treated sequentially, the local convection speed must be assigned as the local characteristic speed and the pressure gradient terms must be treated as source terms. The extensions of a TVD type scheme in a sequential algorithm can perform well for several flow problems with or without strong source effects; however, the role of some key parameters previously defined in the density–based simultaneous solvers needs to be re–evaluated.

The present chapter aims to extend the framework developed in Chapter III to a multi–dimensional pressure–based sequential algorithm, namely the well–known SIMPLE algorithm (Patankar 1980). Compared to the design philosophy for convection schemes employed in Chapter II, a different viewpoint for the convection schemes is now adopted, namely, that of a nonlinear artificial dissipation incorporated into a central differencing based flux estimation. In this manner a scheme based on the notion of controlled variation and termed as the *controlled variation scheme* (CVS) has been devised and implemented in the context of a sequential solution technique. Though the TVD property itself cannot be expected to hold in the framework of a sequential solver, one can nevertheless use the concept of nonlinear dissipation embodied in the TVD schemes to regulate the amount of numerical diffusion in a basic scheme such as the central difference scheme, which though being second–order accurate, yields spurious oscillations in convection dominated flows and near sharp gradients. One can interpret the CVS as a scheme that uses the central difference scheme for the convection terms as a base and augments the physical diffusion with an appropriate nonlinear numerical dissipation in order to suppress the dispersive effect of the central difference scheme.

The goal here is to develop and assess the performance of the concept of CVS for recirculating flows. In this chapter, we extend the formalism of the TVD schemes to two–dimensional cases by applying the scheme along the two spatial directions independent of each other. Thus, the multi–dimensional case is treated as a collection of multiple

one–dimensional cases, while maintaining the same formal order of accuracy of the scheme as in the simultaneous solution method. The local characteristic speeds along each direction are the local convection speeds along that particular direction. The CVS chosen for this study is based on Harten's second–order TVD scheme which uses the so–called *minmod* flux limiter, and is described in Chapter III.

The present chapter focuses on several issues. One is the understanding of the role of the nonlinear numerical dissipation employed by the controlled variation scheme and how it modifies the effective cell Peclet number– –which indicates the relative significance of convection and diffusion (physical plus numerical)– –in regions of high solution gradients. Two model problems have been studied, namely, the linear, steady Burgers' (convection–diffusion) equation, with and without a source term. Another issue of interest is the convergence property of the CVS for practical computations. Consistent with the original SIMPLE algorithm, the fully implicit TVD scheme is used as the basis for the CVS. The implicit TVD schemes are highly nonlinear and the iterative process required to solve the resulting nonlinear equation at every timestep negates the advantage of a large timestep allowed by implicit schemes. To overcome this, linearized versions of these implicit schemes devised by Yee (1986, 1987a) are implemented in the sequential algorithm and their convergence properties investigated. We focus on steady state solutions in the present study. Issues regarding the iterative implementation of the CVS to solve the steady state model problems are addressed by investigating several versions of the CVS, each with a different formulation of coefficients and source terms. The implementation of the controlled variation scheme (CVS), identified as the most efficient of the versions mentioned above, is described in the framework of the two–dimensional sequential SIMPLE algorithm and used to compute incompressible flows in a lid–driven cavity and over a backward–facing step.

5.2 Harten's Implicit Second–order TVD Scheme

The basic features of Harten's second–order TVD scheme were covered in Chapter III; however, an explicit time discretization was used there. For the purposes of the present chapter, an implicit time discretization is required. Consequently, a brief outline of Harten's *implicit* second–order TVD scheme is presented next.

A scalar conservation law can be written as follows

$$\frac{\partial w}{\partial t} + \frac{\partial f(w)}{\partial x} = 0 \tag{5.1}$$

where w is the dependent variable and f is the flux of w. For the second–order implicit Harten's TVD scheme, the numerical approximation for w_i^{n+1}, where the subscript i represents the spatial node and the superscript $n+1$ and n represent the time levels, is given by

$$w_i^{n+1} + \lambda\theta\left(\tilde{f}_{i+1/2}^{n+1} - \tilde{f}_{i-1/2}^{n+1}\right) = w_i^n - \lambda(1-\theta)\left(\tilde{f}_{i+1/2}^{n} - \tilde{f}_{i-1/2}^{n}\right) \tag{5.2}$$

where $\lambda = \Delta t/\Delta x$ and θ is a measure of implicitness of the scheme. We obtain explicit, fully implicit and Crank–Nicolson schemes for $\theta = 0$, 1 and 1/2, respectively. The numerical fluxes in the above are given by

$$\tilde{f}_{i+1/2} = \frac{1}{2}\left[f_i + f_{i+1} + g_i + g_{i+1} - Q(a_{i+1/2} + \gamma_{i+1/2})\Delta_{i+1/2}w\right] \tag{5.3a}$$

$$\tilde{f}_{i-1/2} = \frac{1}{2}\left[f_i + f_{i-1} + g_i + g_{i-1} - Q(a_{i-1/2} + \gamma_{i-1/2})\Delta_{i-1/2}w\right] \tag{5.3b}$$

For later use, we express the above numerical fluxes as follows:

$$\tilde{f}_{i+1/2} = \overline{F}_{i+1/2} - \left(\overline{Q}_{i+1/2} - \overline{G}_{i+1/2}\right) \tag{5.4a}$$

$$\tilde{f}_{i-1/2} = \overline{F}_{i-1/2} - \left(\overline{Q}_{i-1/2} - \overline{G}_{i-1/2}\right) \tag{5.4b}$$

and also write

$$\overline{F} = \overline{F}_{i+1/2} - \overline{F}_{i-1/2}, \quad \overline{Q} = \overline{Q}_{i+1/2} - \overline{Q}_{i-1/2}, \quad \overline{G} = \overline{G}_{i+1/2} - \overline{G}_{i-1/2} \tag{5.5}$$

The $\overline{F}$, $\overline{Q}$ and $\overline{G}$ terms in Eqs. (5.4)–(5.5) consist of the f, g and Q terms of Eq. (5.3), respectively. For later reference, we present here the complete forms of $\overline{Q}_{i+1/2}$ and $\overline{G}_{i+1/2}$:

$$\overline{Q}_{i+1/2} = \frac{1}{2}Q\left(a_{i+1/2} + \gamma_{i+1/2}\right)\Delta_{i+1/2}w \tag{5.6a}$$

$$\overline{G}_{i+1/2} = \frac{1}{2}\left(g_i + g_{i+1}\right) \tag{5.6b}$$

The various quantities used in the above definitions are given as follows:

$$g_i = s_{i+1/2} \cdot \max\left[0\ ,\ \min\left(\sigma(a_{i+1/2}).\left|\Delta_{i+1/2}w\right|\ ,\ s_{i+1/2}.\sigma(a_{i-1/2})\Delta_{i-1/2}w\right)\right] \tag{5.7}$$

$$= \begin{cases} s_{i+1/2}.\min\left(\sigma(a_{i+1/2}).\left|\Delta_{i+1/2}w\right|,\ \sigma(a_{i-1/2}).\left|\Delta_{i-1/2}w\right|\right), & \text{if } \Delta_{i+1/2}w\Delta_{i-1/2}w > 0 \\ 0 & \text{if } \Delta_{i+1/2}w\Delta_{i-1/2}w \leq 0 \end{cases}$$

with

$$\sigma(a_{i+1/2}) = \begin{cases} \frac{1}{2}Q(a_{i+1/2}) + \left(\theta - \frac{1}{2}\right)\lambda(a_{i+1/2})^2 & \text{for } \textit{unsteady cases} \\ \frac{1}{2}Q(a_{i+1/2}) & \text{for } \textit{steady cases} \end{cases} \tag{5.8a}$$

$$s_{i+1/2} = sign\left(\Delta_{i+1/2}w\right) \tag{5.8b}$$

$$a_{i+1/2} = \begin{cases} \dfrac{f_{i+1} - f_i}{\Delta_{i+1/2}w} & \text{if } \Delta_{i+1/2}w \neq 0 \\ \dfrac{\partial f}{\partial u} & \text{if } \Delta_{i+1/2}w = 0 \end{cases} \tag{5.8c}$$

$$\gamma_{i+1/2} = \begin{cases} \dfrac{g_{i+1} - g_i}{\Delta_{i+1/2}w} & \text{if } \Delta_{i+1/2}w \neq 0 \\ 0 & \text{if } \Delta_{i+1/2}w = 0 \end{cases} \tag{5.8d}$$

and $\Delta_{i+1/2}w = w_{i+1} - w_i$. (5.8e)

It should be noted that $a_{i+1/2}$ is the physical characteristic speed whereas $(a_{i+1/2} + \gamma_{i+1/2})$ is the modified numerical characteristic speed. Q, called the dissipation function, is a non–negative quantity, given by

$$Q(x) = |x| \tag{5.9}$$

It should be pointed out here that a modification to the above expression of $Q(x)$ is often made

for the solution of Euler equations in simultaneous solvers by selectively increasing the magnitude of $Q(x)$ for vanishingly small characteristic speeds (Harten 1983, 1984, Yee *et al.* 1985), as given by Eq. (3.21) in Chapter III. However, there it is necessary to introduce this additional numerical dissipation to prevent the violation of the so–called entropy condition. A similar approach has been employed for sequential solvers for solving one–dimensional gas dynamics problems in Chapter III. For computing incompressible, recirculating flows using the multi–dimensional pressure–based sequential solver employed in the present study, no such modification of Q(x) is required.

5.3 Linearized Versions of the Implicit TVD Scheme

The sequential solution algorithm employed for steady state solutions of the Navier–Stokes equations in the present study is the well known SIMPLE algorithm (Patankar 1980). The specific details of the particular algorithm, already discussed in Chapter II, are not important; it is the generic elements of pressure–based algorithms in the context of a sequential solution procedure that are the focus of the present chapter. We employ the fully implicit TVD scheme (i.e., $\theta = 1$) as the basis for development of the controlled variation scheme (CVS) for computing steady state flows. The implicit and highly nonlinear equations resulting from this would require iterations at every timestep if a time–stepping approach to steady state is employed. If an infinite timestep is chosen to solve for steady state, as in the present study, the number of iterations required to achieve convergence will be very large. Consequently, some linearized versions of implicit TVD schemes have been devised (Yee *et al.* 1985, Yee 1986, 1987a). We describe two of these versions next. Both versions will be adopted to solve the one–dimensional model problems. Additional implementational details, in the context of the pressure–based algorithm, will be presented later in Section 5.5.

5.3.1 Linearized Non–Conservative Implicit (LNI) Form

Using definitions (5.3a) and (5.3b), Eq. (5.2) can be written as

$$w_i^{n+1} + \frac{\lambda\theta}{2}\begin{bmatrix} f_{i+1} + f_i + g_{i+1} + g_i - Q\left(a_{i+1/2} + \gamma_{i+1/2}\right)\Delta_{i+1/2}w \\ -f_i - f_{i-1} - g_i - g_{i-1} + Q\left(a_{i-1/2} + \gamma_{i-1/2}\right)\Delta_{i-1/2}w \end{bmatrix}^{n+1} \tag{5.10}$$
$$= w_i^n - \lambda(1-\theta)\left(\tilde{f}_{i-1/2}^n - \tilde{f}_{i-1/2}^n\right) \equiv \mathcal{S}^n$$

Now using definitions (5.8c) and (5.8d), we can write the above as

$$w_i^{n+1} + \frac{\lambda\theta}{2}\Big[\left(a_{i+1/2} + \gamma_{i+1/2}\right) - Q\left(a_{i+1/2} + \gamma_{i+1/2}\right)\Big]^{n+1}\Delta_{i+1/2}w^{n+1}$$
$$- \frac{\lambda\theta}{2}\Big[-\left(a_{i-1/2} + \gamma_{i-1/2}\right) - Q\left(a_{i-1/2} + \gamma_{i-1/2}\right)\Big]^{n+1}\Delta_{i-1/2}w^{n+1} \tag{5.11}$$
$$= w_i^n - \lambda(1-\theta)\left(\tilde{f}_{i-1/2}^n - \tilde{f}_{i-1/2}^n\right) \equiv \mathcal{S}^n$$

This form can be shown to be TVD (Harten 1984, Yee 1986). However, this form of the implicit scheme cannot be expressed in conservation form and thus it is non–conservative except at steady state where it has been shown that it does reduce to a conservative form (Harten 1984). Thus, this linearized version is suitable only for steady state calculations.

For our purpose in the present study, we choose the fully implicit scheme, i.e., $\theta = 1$, and we employ the approach of taking an infinitely large timestep to make the numerical fluxes completely independent of the timestep. Thus we get the following:

$$\left(w_i^{n+1} - w_i^n\right)\frac{\Delta x}{\Delta t}$$
$$+ \frac{1}{2}\Big[\left(a_{i+1/2} + \gamma_{i+1/2}\right) - Q\left(a_{i+1/2} + \gamma_{i+1/2}\right)\Big]^{n+1}\Delta_{i+1/2}w^{n+1} \tag{5.12}$$
$$- \frac{1}{2}\Big[-\left(a_{i-1/2} + \gamma_{i-1/2}\right) - Q\left(a_{i-1/2} + \gamma_{i-1/2}\right)\Big]^{n+1}\Delta_{i-1/2}w^{n+1} = 0$$

where the first term vanishes due to the infinitely large timestep Δt. The superscripts n and $n+1$ signify the previous and current iteration levels at steady state, respectively. If we linearize the above nonlinear equation by dropping the superscripts of the coefficients of

$\Delta_{i\pm 1/2}w^{n+1}$ from $n+1$ to n, we get the following:

$$E_1 u_{i-1}^{n+1} + E_2 u_i^{n+1} + E_3 u_{i+1}^{n+1} = 0 \tag{5.13}$$

where

$$E_1 = \frac{1}{2}\left[-\left(a_{i-1/2} + \gamma_{i-1/2}\right) - Q\left(a_{i-1/2} + \gamma_{i-1/2}\right)\right]^n \tag{5.14a}$$

$$E_3 = \frac{1}{2}\left[\left(a_{i+1/2} + \gamma_{i+1/2}\right) - Q\left(a_{i+1/2} + \gamma_{i+1/2}\right)\right]^n \tag{5.14b}$$

$$E_2 = -\left(E_1 + E_2\right) \tag{5.14c}$$

It can be observed that the above form is spatially a five–point scheme with a tridiagonal system of linear equations and has a dominant diagonal.

5.3.2 Linearized Conservative Implicit (LCI) Form

A linearized conservative version of the implicit TVD scheme can also be obtained. First, we write Eq. (5.3a) as

$$\tilde{f}_{i+1/2} = \frac{1}{2}\left[f_i^{n+1} + f_{i+1}^{n+1}\right] + \left[\left[\frac{g_i + g_{i+1}}{\Delta_{i+1/2}w}\right] - Q(a_{i+1/2} + \gamma_{i+1/2})\right]^{n+1} \Delta_{i+1/2}w^{n+1} \tag{5.15}$$

Then using a local Taylor series expansion about w^n given by

$$f^{n+1} - f^n = a^n\left(w^{n+1} - w^n\right) + \mathcal{O}\left(\Delta t^2\right) \tag{5.16}$$

where $a = \partial f/\partial u$ and adding and subtracting f_{i+1}^n to f_{i+1}^{n+1} we get

$$\left(f_{i+1}^{n+1} - f_{i+1}^n\right) + f_{i+1}^n = a_{i+1}^n\left(w_{i+1}^{n+1} - w_{i+1}^n\right) + f_{i+1}^n \equiv a_{i+1}^n w_{i+1}^{n+1} \tag{5.17}$$

Performing a similar manipulation in the expression for $\tilde{f}_{i-1/2}$, we obtain a linearized conservative implicit (LCI) form which preserves the conservative property of the differencing scheme and is thus applicable for both steady and unsteady problems.

For our present applications, we choose the fully implicit scheme with an infinitely large timestep and linearize by dropping the superscripts of the coefficients of $\Delta_{i\pm 1/2}w^{n+1}$ from $n+1$ to n; we get the following form:

$$E_1 u_{i-1}^{n+1} + E_2 u_i^{n+1} + E_3 u_{i+1}^{n+1} = 0 \tag{5.18}$$

where

$$E_1 = \frac{1}{2}\left[- a_{i-1} + \tau_{i-1/2} - Q\left(a_{i-1/2} + \gamma_{i-1/2}\right)\right]^n \tag{5.19a}$$

$$E_3 = \frac{1}{2}\left[\quad a_{i+1} + \tau_{i+1/2} - Q\left(a_{i+1/2} + \gamma_{i+1/2}\right)\right]^n \tag{5.19b}$$

$$E_2 = \frac{1}{2}\left[- \tau_{i+1/2} + Q\left(a_{i+1/2} + \gamma_{i+1/2}\right) - \tau_{i-1/2} + Q\left(a_{i-1/2} + \gamma_{i-1/2}\right)\right]^n \tag{5.19c}$$

with

$$\tau_{i+1/2}^n = \left[\frac{g_i + g_{i+1}}{\Delta_{i+1/2} w}\right]^n \qquad \tau_{i-1/2}^n = \left[\frac{g_i + g_{i-1}}{\Delta_{i-1/2} w}\right]^n \tag{5.19d}$$

Like the LNI form, this too is a five–point scheme with a tridiagonal system of linear equations but it does not maintain diagonal dominance because in general $a_{i+1} - a_{i-1} \neq 0$. A drawback of the LCI form is that it may not be unconditionally TVD for $\theta = 1$; no proof exists yet (Yee 1986, 1987a). However, in practice, the LCI form has been found to be stable and yields high accuracy for fairly large CFL numbers (Yee 1986).

5.4 Model Problem I: Linear Convection–Diffusion Equation

The first model problem studied here is the one–dimensional, steady state linear Burgers' equation

$$\alpha\phi_x = \beta\phi_{xx} \ , \qquad \alpha, \beta = constants > 0 \tag{5.20}$$

with the boundary conditions

$$\phi(0) = 0 \ , \qquad \phi(1) = 1$$

The exact solution to this problem is given by

$$\phi(x) = \frac{1 - e^{Rx}}{1 - e^R} \tag{5.21}$$

where $R = \alpha/\beta$. For small values of R, the solution varies smoothly throughout the domain. But for large values of R, $\phi(x)$ is virtually zero except in a region near x=1 which has the thickness of the order of $1/R$. Thus, the solution is of boundary layer type since it is dominated

by convection in the majority of the domain and the entire variation in the solution is contained in the thin region next to the right boundary. This problem has been used as a model case by many investigators, e.g., Roache (1972), Leonard (1979) and Shyy (1985a).

Numerically, the diffusion term is conveniently and effectively approximated by second–order central differencing. If we use central differencing for the convection term, then the numerical approximation to Eq. (5.20) takes the form

$$(2 - P)\phi_{i+1} + (-4)\phi_i + (2 + P)\phi_{i-1} = 0 \tag{5.22}$$

where $P = \alpha h/\beta$ and is called the cell Peclet number. Here h is the grid spacing, assumed to be uniform. Eq. (5.22) indicates that if $|P| > 2$, then oscillations in the solution profile may result due to a lack of necessary damping.

If the CVS is employed for the convection term, Eq. (5.20) is approximated by

$$\left(\tilde{f}_{i+1/2} - \tilde{f}_{i-1/2}\right) = \frac{1}{P}\left(\phi_{i+1} - 2\phi_i + \phi_{i-1}\right) \tag{5.23}$$

where $\tilde{f}_{i\pm 1/2}$ are defined in Eq. (5.3) with $f \equiv \phi$ and $a_{i+1/2} = a_{i-1/2} = 1$. Using these definitions, we can write the numerical scheme in the form

$$\left(\phi_{i+1} - \phi_{i-1}\right) = \frac{2}{P}\left[\left(\phi_{i+1} - 2\phi_i + \phi_{i-1}\right) + SP\right] \tag{5.24}$$

where S consists of the net flux over and above the central difference flux, i.e.,

$$\begin{aligned} S = -\frac{1}{2}\Big[& g_{i+1} - g_{i-1} - Q(a_{i+1/2} + \gamma_{i+1/2})\Delta_{i+1/2}w \\ & + Q(a_{i-1/2} + \gamma_{i-1/2})\Delta_{i-1/2}w\Big] \end{aligned} \tag{5.25}$$

From this viewpoint, the controlled variation scheme can be interpreted as nothing but the basic central difference scheme accompanied by a nonlinear numerical dissipation term which suppresses the dispersive characteristic of the central difference scheme at high cell Peclet numbers. In the next section, we discuss the issue of incorporation of this nonlinear term into the numerical scheme which can lead to different versions of the CVS.

5.4.1 Implementation of the CVS for the Model Problem

In Section 5.2, two linearized versions of the implicit TVD scheme have been described. We use these two versions to construct the CVS to solve the model problem. We also employ two other versions with different degrees of implicitness in their numerical fluxes. Since all four versions of the CVS to be discussed in this section are identical at steady state, they must yield an identical solution if and when convergence is achieved. Thus, one might wonder at the utility of implementing these different versions. To illustrate the motivation behind investigating these different formulations of the CVS, note that all of these versions lead to a system of equations that can be expressed as

$$A\,\vec{x} = \vec{b} \tag{5.26}$$

where A is the tridiagonal coefficient matrix, $\vec{x}$ is the vector consisting of the unknown ϕ's and $\vec{b}$ consists of the boundary values and source terms (physical or numerical), if any. The CVS involves a highly nonlinear dissipation term, given by Eq. (5.25), which can be implemented in various ways, each way leading to a different form for the matrix A and the vector $\vec{b}$.The different versions, as will be shown later, have very different convergence properties both in terms of the allowable magnitude of relaxation factors for stability of the computation and the number of iterations required to achieve a desired level of convergence.

In this section, we outline four versions of the CVS, which will be implemented to solve model problem I in order to determine which formulation is the most robust in terms of stability and convergence. These versions are based on the fully implicit scheme, i.e., Eq. (5.2) with $\theta = 1$, for steady state cases. The convection term is approximated by using one of the four versions to be discussed next and the diffusion term is approximated by second–order central differencing.

Version A

As described earlier, the CVS treats the convection term via the central difference flux $\overline{F}$ with a net numerical dissipation flux $(\overline{Q} - \overline{G})$. For steady cases, instead of linearizing

all the coefficients (as done in Section 5.2), this version treats the physical diffusive flux and the central difference flux $\overline{F}$ as part of the matrix A and the net dissipation flux $(\overline{Q} - \overline{G})$ as a source term included in the vector $\vec{b}$. Thus, the basic formulation of the central difference scheme is retained and the entire dissipation term of the CVS is placed into the source term. This serves to make the scheme "explicit" in the sense that at steady state the nonlinear dissipation term is explicitly treated as part of the source term and not implicitly as part of the coefficient matrix A. The numerical approximation to Eq. (5.20) can now be expressed as

$$\begin{aligned} &\frac{\alpha}{2}\left(\phi_{i+1} + \phi_i\right) - \frac{\alpha}{2}\left(\phi_i + \phi_{i-1}\right) - \alpha\left(\overline{Q}_{i+1/2} - \overline{G}_{i+1/2}\right) + \alpha\left(\overline{Q}_{i-1/2} - \overline{G}_{i-1/2}\right) \\ &\quad = \frac{\beta}{h}\left(\phi_{i+1} - \phi_i\right) - \frac{\beta}{h}\left(\phi_i - \phi_{i-1}\right) \end{aligned} \tag{5.27}$$

This can be expressed in the form

$$E_1\phi_{i-1}^{n+1} + E_2\phi_i^{n+1} + E_3\phi_{i+1}^{n+1} = \mathcal{S} \tag{5.28}$$

where we have

$$\begin{aligned} E_1 &= \frac{\beta}{h} + \frac{\alpha}{2} \\ E_3 &= \frac{\beta}{h} - \frac{\alpha}{2} \\ E_2 &= -\left(E_1 + E_3\right) \\ \mathcal{S} &= -\alpha\left(\overline{Q} - \overline{G}\right) \end{aligned} \tag{5.29}$$

<u>Version B</u>

This version is also based on the fully implicit scheme at steady state. The difference between this version and the previous one is that along with the diffusive and central difference convective fluxes, the $\overline{Q}$ flux is also included in the coefficient matrix A by factoring out $\Delta_{i+1/2}\phi$ and $\Delta_{i-1/2}\phi$; only the $\overline{G}$ flux is placed in the source term vector $\vec{b}$. Thus, only one part of the nonlinear dissipation term is treated explicitly as part of the source term whereas the other part is retained implicitly in the coefficient matrix A. In this regard,

version B is less "explicit" or more "implicit" compared to version A. For version B, the scheme again takes the form of Eq. (5.28) with

$$
\begin{aligned}
E_1 &= \left(\frac{\beta}{h} + \frac{\alpha}{2} Q_{i+1/2}\right) + \frac{\alpha}{2} \\
E_3 &= \left(\frac{\beta}{h} + \frac{\alpha}{2} Q_{i-1/2}\right) - \frac{\alpha}{2} \\
E_2 &= -\left(E_1 + E_3\right) \\
\mathcal{S} &= \alpha\, \overline{G}
\end{aligned}
\tag{5.30}
$$

Version C

Version C of the CVS is a linearized fully implicit version based on the LNI form of the TVD scheme described in Section 5.2. Using Eq. (5.12) with an infinitely large timestep Δt, the numerical approximation to the model problem can be expressed as

$$
\begin{aligned}
\frac{\alpha}{2}\Big[\quad \left(a_{i+1/2} + \gamma_{i+1/2}\right) - Q\left(a_{i+1/2} + \gamma_{i+1/2}\right)\Big]^n \left(\phi_{i+1} - \phi_i\right)^{n+1} \\
- \frac{\alpha}{2}\Big[- \left(a_{i-1/2} + \gamma_{i-1/2}\right) - Q\left(a_{i-1/2} + \gamma_{i-1/2}\right)\Big]^n \left(\phi_i - \phi_{i-1}\right)^{n+1} \\
= \frac{\beta}{h}\left(\phi_{i+1} - \phi_i\right) - \frac{\beta}{h}\left(\phi_i - \phi_{i-1}\right)
\end{aligned}
\tag{5.31}
$$

where $a_{i+1/2} = a_{i-1/2} = 1$ for the present case and the superscript n designates the iterative step. The above can be expressed in the form of Eq. (5.28) where we have

$$
\begin{aligned}
E_1 &= \frac{\beta}{h} - \frac{\alpha}{2}\Big[- \left(a_{i-1/2} + \gamma_{i-1/2}\right) - Q\left(a_{i-1/2} + \gamma_{i-1/2}\right)\Big]^n \\
E_3 &= \frac{\beta}{h} - \frac{\alpha}{2}\Big[\quad \left(a_{i+1/2} + \gamma_{i+1/2}\right) - Q\left(a_{i+1/2} + \gamma_{i+1/2}\right)\Big]^n \\
E_2 &= -\left(E_1 + E_3\right) \\
\mathcal{S} &= 0
\end{aligned}
\tag{5.32}
$$

Version D

This version is based on the LCI form of the TVD scheme described in Section 5.2 and again leads to the form given by Eq. (5.28). The coefficients E_1, etc., are obtained from

the LCI form in a manner similar to version C above along with $\mathcal{S} = 0$, and will not be presented here. Versions C and D treat all the terms in an implicit manner and thus there are no source terms associated with these versions.

In summary, versions C and D of the CVS for the model problem place the net numerical flux in the coefficient matrix A with nothing in the source vector $\vec{b}$ whereas versions A and B include the $(\overline{Q} - \overline{G})$ and $\overline{G}$ fluxes, respectively, in the source vector. All four versions must yield identical solutions if and when convergence is achieved; these different versions are formulated essentially to investigate the convergence characteristics of the CVS, and to unequivocally determine the version which is the most robust in terms of convergence and stability, as discussed earlier.

5.4.2 Results for Model Problem I

For the linear convection–diffusion equation studied here, we choose $\alpha = 1000$ and $\beta = 1$. The length of the domain is 1 with the grid spacing $h = 0.02$. Thus, the cell Peclet number for the flow is 20. The central difference scheme, as expected, yields oscillations as seen in Fig. 5.1(a). The CVS operates by injecting a nonlinear numerical dissipation into the central difference scheme to suppress its dispersive effect. This is evident from Fig. 5.1(a) where it can be seen that the CVS yields an oscillation–free solution profile.

To compare the performance of the CVS with other convection schemes, the solution profile obtained with the QUICK scheme is also plotted in Fig. 5.1(a) and those obtained with first–order upwind and second–order upwind schemes are plotted in Fig. 5.1(b) along with that obtained with the CVS, in the vicinity of the right boundary. The critical value of cell Peclet number for the model problem, beyond which oscillations occur, is ∞ for the first– and second–order upwind schemes, 2 for the central difference scheme and 8/3 for the QUICK scheme (Shyy 1985a). As can be seen from Fig. 5.1(a), the QUICK scheme indeed yields oscillations, albeit smaller in magnitude and extent than those obtained with the central difference scheme. First– and second–order upwind schemes yield oscillation–free

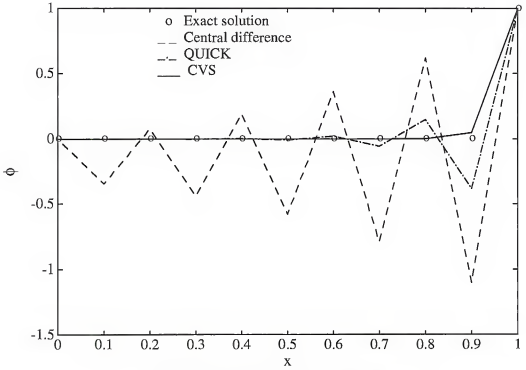

(a) Solution profile over the whole domain.

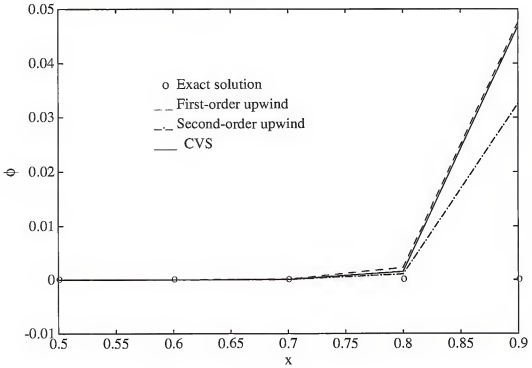

(b) Solution profile near the right boundary.

Fig. 5.1. Solution profiles for model problem I (without source) using various schemes.

solution profiles similar to the profile obtained by the CVS. First–order upwinding, which has a high level of numerical dissipation, smears out the solution profile the most. The profile obtained with the CVS turns out to be more smeared than that with the second–order upwind scheme, and is comparable to that with the first–order upwind scheme. Nevertheless, suffice it to say here that all three numerical solutions shown in Fig. 5.1(b) are very acceptable, and the basic goal of the CVS, namely, to help improve the solution accuracy based on the central difference scheme for a case with high cell Peclet number, is realized. It should be pointed out that the linear Burgers' equation without source terms is a more straightforward problem to solve. The relative performance of all these schemes is more distinguishable for a very high cell Peclet number flow with a source term, which is presented in the next section. But before doing that, we shall address the effect of different implementations of the CVS on convergence rate.

The standard tridiagonal solver with line SOR is used to solve the system of equations. All four versions of the CVS for the present model problem yield converged solutions which are identical within the tolerance of machine accuracy. However, their convergence characteristics are quite different, as shown in Fig. 5.2. Version A, which treats the $(\overline{Q} - \overline{G})$ flux as a source term, is the least stable and does not converge for relaxation factors, ω, higher than 0.1. Though this version has the most straightforward formulation and implementation, it has poor convergence characteristics by virtue of the "explicit" treatment of the dissipation term, as discussed earlier. The other three versions converge with higher values of relaxation factors. Versions B and D show similar convergence characteristics, even though they have different coefficient matrix A and the source vector $\vec{b}$. It is observed that version C, which is a linearized form of the fully implicit scheme, exhibits the lowest levels of residuals with a relaxation factor equal to 0.5 and a smooth convergence history. It is the most robust in terms of sensitivity to the variation in the magnitude of relaxation factors as well as the number of iterations required to achieve a desired level of convergence. It should be pointed out here that this is true for all the problems

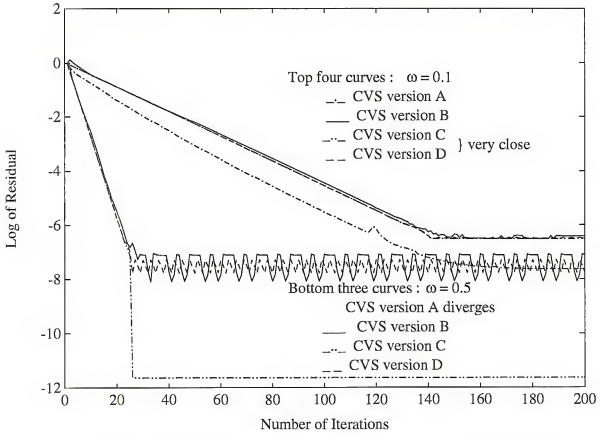

Fig. 5.2. Convergence paths for four versions of CVS for model problem I.

investigated in this study including the two–dimensional recirculating flows to be discussed later.

Next we demonstrate the mechanism by which the CVS operates. For the present model problem, if we use the central difference scheme for the convection term, wiggles are produced as seen in Fig. 5.1(a). Here, it can be easily shown that the wiggles are produced due to the right boundary condition. For example, for a high cell Peclet number such as the one used in the present case, the exact solution profile consists of zeros (virtually) everywhere except at the right boundary point. With the central difference scheme, at the grid point adjacent to the boundary, i.e., i=10, in order that Eq. (5.22) holds for initially given values of ϕ_{11} (=1) and ϕ_9 (=0) with $P > 2$, ϕ_{10} must assume a negative value to increase the magnitude of the diffusion term. Thus, the absence of any numerical dissipation in central

differencing to augment the physical diffusion causes the solution profile to exhibit wiggles in order to supply an "artificial diffusion" to balance the convection term in the region where the important length scale can not be resolved appropriately, as quite lucidly illustrated by Roache (1972). From a different point of view, one of the roots of the characteristic equation corresponding to the finite difference equation resulting from the central difference scheme becomes negative when $|P| > 2$ and according to the standard theory of finite difference equations, oscillations in the solution might result. This, of course, is a necessary condition; for instance, if, instead of the Dirichlet condition specified presently for the right boundary, we specify a Neumann boundary condition of the type $\partial\phi/\partial x=0$, the central difference scheme will yield the oscillation–free exact solution which is zero everywhere, for any value of cell Peclet number. This is due to the fact that with such a Neumann boundary condition, the governing equation itself reduces to a first–order equation, thus eliminating the root of the finite difference equation whose sign is dependent on the magnitude of the cell Peclet number.

5.4.3 Effective Cell Peclet Number

For the model problem under investigation, the CVS, which is based on the central difference scheme, eliminates the wiggles discussed above by injecting numerical dissipation where necessary. In order to illustrate the relation between the balancing terms in the CVS, we rewrite the fully nonlinear form, Eq. (5.27), as follows

$$\frac{\alpha}{2}\left(\phi_{i+1}+\phi_i\right)-\frac{\alpha}{2}\left(\phi_i+\phi_{i-1}\right) \tag{5.33}$$
$$=\left[\frac{\beta}{h}+\frac{\alpha\left(\overline{Q}_{i+1/2}-\overline{G}_{i+1/2}\right)}{\Delta_{i+1/2}\phi}\right]\left(\phi_{i+1}-\phi_i\right)-\left[\frac{\beta}{h}+\frac{\alpha\left(\overline{Q}_{i-1/2}-\overline{G}_{i-1/2}\right)}{\Delta_{i-1/2}\phi}\right]\left(\phi_i-\phi_{i-1}\right)$$

In the above, α is the coefficient of effective convection; the first term within the square brackets on the right hand side of the equation, namely β/h, is the coefficient of physical diffusion and the second term in the square brackets is the nonlinear dissipation of the CVS.

The effective cell Peclet number of the CVS for the model problem can thus be defined as the ratio of the convective coefficient and the coefficient of net dissipation:

$$P_{cvs} = \frac{\alpha}{\left[\frac{\beta}{h} + \alpha\left(\frac{\overline{Q}_{i+1/2} - \overline{G}_{i+1/2}}{\Delta_{i+1/2}\phi}\right)\right]} \tag{5.34}$$

While computing the coefficient of the nonlinear dissipation (second term in the denominator of the above expression), one can avoid the singularity that occurs when $\Delta_{i+1/2}\phi = 0$ by prescribing this coefficient to be zero when $\left|\Delta_{i+1/2}\phi\right| \leq \varepsilon$ where ε is a small positive number. For the present case we use $\varepsilon=10^{-4}$. This is equivalent to saying that when $\left|\Delta_{i+1/2}\phi\right|$ is negligibly small, no extra numerical dissipation is required. It must be pointed out that this artificial cutoff is enforced only for the estimation of the effective cell Peclet numbers and not during the computation of the numerical fluxes used by the CVS. Note that the original cell Peclet number (i.e., with respect to the central difference scheme) is given by

$$P \equiv P_{central} = \frac{\alpha}{\beta/h} \tag{5.35}$$

A comparison of P_{cvs} and $P_{central}$ shows that the CVS reduces the effective cell Peclet number of the flow, where necessary, by augmenting the physical diffusion with numerical dissipation.

Table 5.1 shows the values of the relevant quantities associated with the model problem. As presented in Eqs. (5.4)–(5.6), the $\overline{F}$ flux represents the central difference operator, $\overline{Q}$ the numerical dissipation and $\overline{G}$ the numerical anti–dissipation. The $\overline{Q}$ flux is responsible for the TVD property of the original scheme developed by Harten, whereby spurious oscillations near discontinuities are suppressed. The $\overline{G}$ flux serves to improve the accuracy by sharpening the resolution of the scheme via anti–diffusion in regions away from the discontinuities in the flow field. Thus ($\overline{Q}$–$\overline{G}$) represents the net numerical dissipation present in the scheme and this combination provides the higher–order accuracy in the smooth

regions of the flow field along with the capability to suppress spurious oscillations near sharp gradients in the solution profiles. Using an artificial cutoff for the computation of effective cell Peclet numbers by assigning $\varepsilon=10^{-4}$, it can be observed that the CVS injects the dissipation $(\overline{Q} - \overline{G})$ near the right boundary where the wiggles originate for the central difference scheme. In the vicinity of the right boundary, the amount of numerical dissipation augmenting the physical diffusion is high enough to reduce the effective cell Peclet number to a value less than two. However, in the region away from the right boundary, the cell Peclet numbers remain high, resulting in a varying distribution of P_{cvs}. This result has clearly established that the cell Peclet number does not need to be uniformly lower than 2 for a central difference based scheme in order to yield a solution free from spurious oscillations. It should be noted that adjacent to the right boundary, i.e., at the grid point i=10, the first–order version of the CVS has to be employed for which $\overline{G}=0$.

Table 5.1. Values of some variables for model problem I with $\alpha=200$, $\beta=1$, $P=20$ and $\mu=10^{-4}$.

i	ϕ	$\Delta_{i+1/2}\phi$	Q	G	Q–G	P_{cvs}
1	0.0	–	–	–	–	–
2	8.50×10^{-14}	1.78×10^{-12}	0.0	0.0	0.0	20.0
3	1.87×10^{-12}	5.44×10^{-11}	0.0	0.0	0.0	20.0
4	5.63×10^{-11}	1.67×10^{-9}	0.0	0.0	0.0	20.0
5	1.72×10^{-9}	5.12×10^{-8}	0.0	0.0	0.0	20.0
6	5.29×10^{-8}	1.57×10^{-6}	0.0	0.0	0.0	20.0
7	1.62×10^{-6}	4.82×10^{-5}	0.0	0.0	0.0	20.0
8	4.98×10^{-5}	1.47×10^{-3}	0.7418	0.2581	0.4836	1.8737
9	1.52×10^{-3}	4.53×10^{-2}	0.7418	0.2581	0.4836	1.8737
10	4.69×10^{-2}	9.53×10^{-1}	0.5	0.0	0.5	1.8182
11	1.0	–	–	–	–	–

5.5 Model Problem II: Linear Burgers' Equation with Source

As the next test case, we choose the model problem

$$\alpha\phi_x = \beta\phi_{xx} + \alpha\,\psi(x)\ , \qquad \alpha,\beta = constants > 0 \qquad (5.36a)$$
$$\phi(0) = 0$$

with two different choices of conditions at the right boundary, namely,

$$\text{(i) Neumann boundary condition:}\quad (\phi_x)_{x=L} = 0 \qquad (5.36b)$$
$$\text{(ii) Dirichlet boundary condition:}\quad \phi(L) = 0$$

to study the performance of the CVS for convection dominated flows in the presence of source terms. This model problem has been studied by Shyy (1985a) and Leonard (1979). The form of the source term used here is the following:

$$\psi(x) = \begin{cases} ax + b\ , & 0 \le x \le x_1 \\ -\dfrac{(ax_1 + b)}{x_2}x + \dfrac{(x_1 + x_2)}{x_2}(ax_1 + b)\ , & x_1 \le x \le (x_1 + x_2) \end{cases} \qquad (5.37)$$

By varying the parameters in the source term, one can investigate the performance of the various schemes under different distributions of the source. Of the various cases suggested by Shyy (1985a), we choose a source spanning through several mesh lengths. The parameters used are: $P=10^8$ or 10^2, $L=15$, $N=35$, $a=-0.5$, $b=1.76$, $x_1=12h$ and $x_2=8h$. As shown in Eq. (5.36b), two different boundary conditions for the right boundary are investigated. It is of interest to compare the performance of the CVS with the other convection schemes mentioned earlier with the prescribed source distribution and two sets of boundary conditions.

In model problem I studied in Section 5.4, the mechanism that generated the spurious oscillations with central differencing was the boundary condition (as discussed earlier). The oscillations there could also be explained from the viewpoint of the roots of the characteristic equation associated with the central difference scheme. In the presence of a source term in the linear Burgers' equation, the solution of the characteristic equation consists of the

original general solution for the source–free equation and a particular solution due to the presence of the source term. The general solution here is the trivial one, namely, zero everywhere. Thus, the nature of the solution profile, i.e., the presence and the extent of wiggles for high cell Peclet number, using central differencing now depends on the nature of the source term. When the Neumann boundary condition on the right boundary is used in the presence of the source term with the central difference scheme, the solution exhibits very slight oscillations about the exact solution, as shown in Fig. 5.3(a). If the Dirichlet boundary condition is used instead of the zero gradient Neumann condition, oscillations, resulting from an interaction with the Dirichlet boundary condition similar to model problem I, appear even for much lower values of P. To demonstrate this, the solution profile using the central difference scheme for cell Peclet number 10^2 is shown in Fig. 5.3(b).

Next we present the results for model problem II obtained using the CVS. All four versions of the CVS, as discussed in Section 5.4, have been employed to solve model problem II; their convergence characteristics have been found to be consistent with those for model problem I. Again, version C is found to be the most robust in terms of convergence history as well as sensitivity to the size of the relaxation factor. For both sets of boundary conditions, CVS yields oscillation–free profiles, as shown in Fig. 5.4. Thus, it is able to suppress the wiggles in the central difference scheme resulting from the interaction with both source terms and boundary conditions. Moreover, profiles obtained by the CVS are quite comparable to those by the second–order upwind scheme; it is noted that for the Dirichlet boundary condition used here, the QUICK scheme yields oscillations near the right boundary as discussed by Leonard (1979). The first–order upwind, as expected, exhibits an excessive amount of dissipation for both types of boundary conditions as shown in Fig. 5.4.

It is also illustrative to look at the distribution of the effective cell Peclet numbers, defined in Eq. (5.34) and discussed in Section 5.4. Table 5.2 lists the effective cell Peclet numbers obtained using the CVS for model problem II with $P=10^2$ and using the Dirichlet boundary condition, i.e., $\phi_{(x=L)}=0$. Fig. 5.5 shows the distribution of the effective cell Peclet

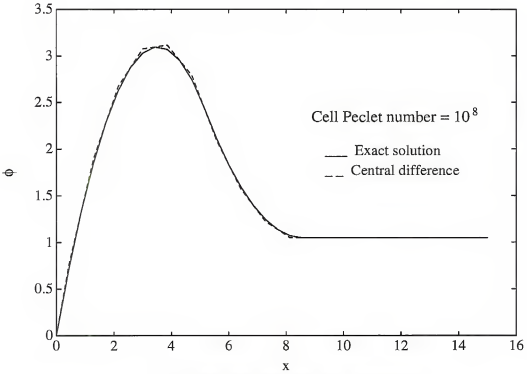

(a) Right boundary condition: Neumann

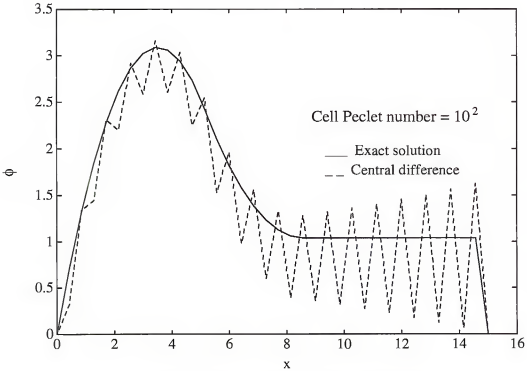

(b) Right boundary condition: Dirichlet

Fig. 5.3. Solution profiles for model problem II (with source) using central difference scheme.

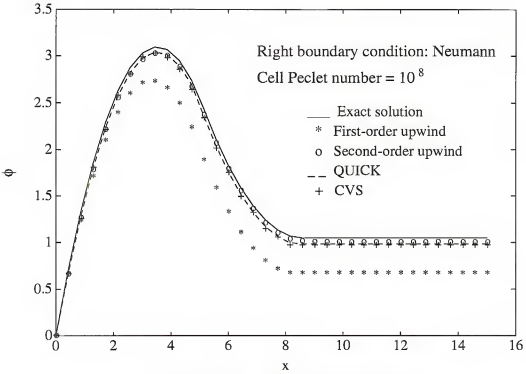

(a) Right boundary condition: Neumann

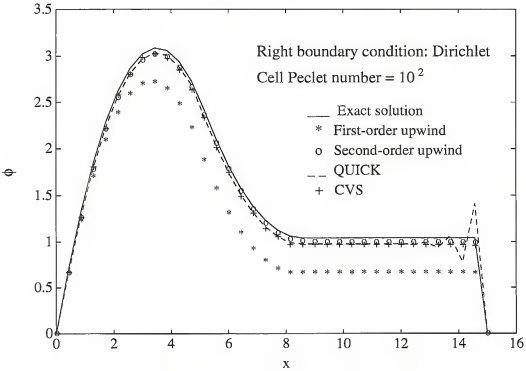

(b) Right boundary condition: Dirichlet

Fig. 5.4. Solution profiles for model problem II using various schemes.

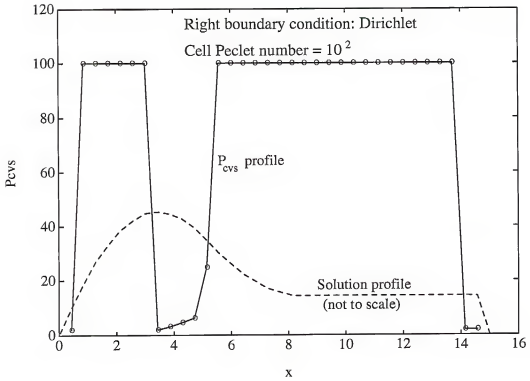

Fig. 5.5. Effective cell Peclet numbers for the CVS with Dirichlet boundary condition and P=100.

Table 5.2. Effective Cell Peclet Numbers for the CVS for Model Problem II; $P=10^2$
Right Boundary Condition: Dirichlet

i	x	P_{cvs}
2	0.42	1.96
9	3.42	1.96
10	3.85	3.15
11	4.28	4.66
12	4.71	6.32
13	5.14	24.85
34	14.14	1.97
35	14.57	1.96
Remaining i	Remaining x	100.00

number, P_{CVS}, over the whole domain. The solution profile is also plotted in the same figure (not to scale) to correlate the cell Peclet numbers with the regions of variation in the solution profile. Again, an artificial cutoff, similar to that for model problem I, is used for the estimation of effective cell Peclet numbers by prescribing $\varepsilon=10^{-4}$. Similar to model problem I, the CVS operates by introducing an appropriate amount of numerical dissipation, where necessary, to effectively reduce the cell Peclet numbers, thus balancing the convection and diffusion terms so as not to produce any spurious oscillations in the solution profile. For instance, it can be seen from Table 5.2 that, near the left and right boundaries (i=2 and 35), and in the "downhill" part of the solution profile (i=9–13), the effective cell Peclet numbers are much smaller than in the rest of the domain. In fact, adjacent to the left boundary (i=2) and at the extremum (i=9) of the solution profile where the profile undergoes a change of sign in slope, the effective cell Peclet number is less than 2. Thus, the CVS effectively reduces the cell Peclet numbers in regions where spurious oscillations might occur with central differencing. In the other regions of the domain, the effective cell Peclet numbers can be quite high, without generating any wiggles.

5.6 Incompressible, Laminar Navier–Stokes Equations

As discussed in Chapter II, we employ the SIMPLE algorithm (Patankar 1980). Typical control volumes employed in this algorithm for the u–velocity component are shown in Fig. 2.1. To recapitulate, the algorithm solves the governing equations in a sequential manner. The velocity components are computed from the respective momentum equations. The velocity and the pressure fields are corrected using a pressure correction equation which is derived by manipulating the continuity and the momentum equations. The correction procedure leads to a continuity–satisfying velocity field. The whole process is repeated until the desired convergence is reached.

For a two–dimensional fluid flow problem, the momentum equations can be written as follows:

$$\frac{\partial(\varrho\phi)}{\partial t} + \frac{\partial J_x}{\partial x} + \frac{\partial J_y}{\partial y} = S^* \tag{5.38}$$

where the J's are the net fluxes along the two directions and are composed of convective and diffusive fluxes, as follows:

$$J_x = (\varrho u\phi) - \mu\frac{\partial\phi}{\partial x} \tag{5.39a}$$

$$J_y = (\varrho v\phi) - \mu\frac{\partial\phi}{\partial y} \tag{5.39b}$$

where $\phi \equiv u \text{ or } v$, μ is the physical viscosity of the fluid, and S^* is the source term consisting of pressure gradient and any other external source terms. Integrating the above over the control volume, we get

$$\begin{aligned}\left[(\varrho\phi)_P - (\varrho\phi)_P^0\right]\frac{\Delta x\Delta y}{\Delta t} + [(\varrho u\phi)_e - (\varrho u\phi)_w]\Delta y + [(\varrho v\phi)_n - (\varrho v\phi)_s]\Delta x \\ - \left[\left(\mu\frac{\partial\phi}{\partial x}\right)_e - \left(\mu\frac{\partial\phi}{\partial x}\right)_w\right]\Delta y - \left[\left(\mu\frac{\partial\phi}{\partial y}\right)_n - \left(\mu\frac{\partial\phi}{\partial y}\right)_s\right]\Delta x = S^{**}\end{aligned} \tag{5.40}$$

where the superscript 0 represents the previous time level and S^{**} is the source term integrated over the control volume.

We now formulate the controlled variation scheme (CVS) by formally extending the TVD scheme from one dimension to the present two–dimensional case. Similar to the model problems described in the previous sections, we use the fully implicit scheme. Steady state analogs of the four versions discussed for model problem I have been investigated for the two–dimensional SIMPLE algorithm and conclusions similar to those for the two model problems have been reached. Consequently, we focus on just the analog of version C of the CVS for model problem I, namely, the linearized version (LNI) of the fully implicit TVD scheme. We next present an outline of the formulation of the CVS in the format of the SIMPLE algorithm for the case of the linearized form (LNI) of the TVD scheme described in Section 5.3.

5.6.1 Linearized Form of the CVS for the SIMPLE Algorithm

Using the LNI form of the fluxes given in Section 5.3 independently along the x– and y–directions, Eq. (5.40) can be expressed as

$$\begin{aligned} & \varrho\, \Delta y\; C^n_{i+1/2}\left(\phi_E - \phi_P\right)^{n+1} - \varrho\, \Delta y\; C^n_{i-1/2}\left(\phi_P - \phi_W\right)^{n+1} \\ + \; & \varrho\, \Delta x\; C^n_{j+1/2}\left(\phi_N - \phi_P\right)^{n+1} - \varrho\, \Delta x\; C^n_{j-1/2}\left(\phi_P - \phi_S\right)^{n+1} \\ = \; & D^n_{i+1/2}\left(\phi_E - \phi_P\right)^{n+1} - D^n_{i-1/2}\left(\phi_P - \phi_W\right)^{n+1} \\ & + D^n_{j+1/2}\left(\phi_N - \phi_P\right)^{n+1} - D^n_{j-1/2}\left(\phi_P - \phi_S\right)^{n+1} + S^{**} \end{aligned} \tag{5.41}$$

where the various coefficients are given by

$$C^n_{i\pm 1/2} = \frac{1}{2}\left[- Q\left(a_{i-1/2} + \gamma_{i-1/2}\right) \pm \left(a_{i-1/2} + \gamma_{i-1/2}\right)\right]^n \tag{5.42a}$$

$$D^n_{i+1/2} = \mu_e \frac{\Delta y}{\delta x_e} = \left(\frac{\mu_P + \mu_E}{2}\right)\frac{\Delta y}{\delta x_e}\,, \quad etc. \tag{5.42b}$$

Note that the subscript i is used to denote the x–direction and j to denote the y–direction.

It has been demonstrated in Chapter III that the signal propagation for the entire sequential system of equations has to be coordinated, which is achieved by assigning the local convection speeds as the local characteristic speeds for the whole system. Thus, in the above equations, we use the following:

$$a_{i+1/2} \equiv a_{i+1/2,j} = \frac{1}{2}\left(u_{i,j} + u_{i+1,j}\right) \tag{5.43a}$$

$$a_{j+1/2} \equiv a_{i,j+1/2} = \frac{1}{2}\left(v_{i,j} + v_{i,j+1}\right) \tag{5.43b}$$

It should be noted that the above interpolations required for the local characteristic speeds result from the staggered nature of the grids employed for the velocity components (Fig. 2.1).

Employing the conventional notation for the SIMPLE algorithm, Eq. (5.41) can be written as

$$A_P\phi_P = A_E\phi_E + A_W\phi_W + A_N\phi_N + A_S\phi_S + b \tag{5.44}$$

The coefficients used in Eq. (5.44) can be expressed as follows:

$$
\begin{aligned}
A_W &= D^n_{i-1/2} - C^n_{i-1/2}\,\varrho\,\Delta y \\
A_E &= D^n_{i+1/2} - C^n_{i+1/2}\,\varrho\,\Delta y \\
A_S &= D^n_{j-1/2} - C^n_{j-1/2}\,\varrho\,\Delta x \\
A_N &= D^n_{j+1/2} - C^n_{j+1/2}\,\varrho\,\Delta x \\
A_P &= A_W + A_E + A_S + A_N
\end{aligned}
\tag{5.45}
$$

5.6.2 Effective Cell Peclet Number

For the present two–dimensional steady state case, the fully nonlinear version of the CVS, similar to Eq. (5.33) for the one–dimensional model problem I (Section 5.4), can be written as

$$
\begin{aligned}
&\frac{F_e}{2}(\phi_E + \phi_P) - \frac{F_w}{2}(\phi_P + \phi_W) + \frac{F_n}{2}(\phi_N + \phi_P) - \frac{F_s}{2}(\phi_P + \phi_S) \\
&= \left[D_e + \varrho\Delta y \frac{\left(\overline{Q}_{i+\frac{1}{2}} - \overline{G}_{i+\frac{1}{2}}\right)}{\Delta_{i+\frac{1}{2}}\phi} \right](\phi_E - \phi_P) - \left[D_w + \varrho\Delta y \frac{\left(\overline{Q}_{i-\frac{1}{2}} - \overline{G}_{i-\frac{1}{2}}\right)}{\Delta_{i-\frac{1}{2}}\phi} \right](\phi_P - \phi_W) \\
&+ \left[D_n + \varrho\Delta x \frac{\left(\overline{Q}_{j+\frac{1}{2}} - \overline{G}_{j+\frac{1}{2}}\right)}{\Delta_{j+\frac{1}{2}}\phi} \right](\phi_N - \phi_P) - \left[D_s + \varrho\Delta x \frac{\left(\overline{Q}_{j-\frac{1}{2}} - \overline{G}_{j-\frac{1}{2}}\right)}{\Delta_{j-\frac{1}{2}}\phi} \right](\phi_P - \phi_S)
\end{aligned}
\tag{5.46}
$$

where the subscripts e, w, n and s (conventionally used in the nomenclature for the SIMPLE algorithm) are used interchangeably with the subscripts $i+1/2$, $i-1/2$, $j+1/2$ and $j-1/2$ to denote the east, west, north and the south face, respectively, of the control volume. In the above equation, F_e, for example, represents the mass flux (or the strength of convective effect) across the east face of the control volume and is commonly called the convective coefficient; it is defined as

$$F_e = (\varrho u)_e \, \Delta y \tag{5.47}$$

The coefficient D_e ($\equiv D_{i+1/2}$ given by Eq. 5.42(b)), called the diffusion coefficient, is an indicator of the magnitude of the physical diffusive effect across the east face. Likewise, the terms involving $(\overline{Q} - \overline{G})$ represent the numerical dissipation of the CVS at the four faces of a control volume and can be termed as nonlinear dissipation coefficients. We can define an effective cell Peclet number of the CVS on the east face (i.e., along the x–direction), as

$$(P_e)_{cvs} = \frac{F_e}{\left[D_e + \varrho \Delta y \left(\frac{\overline{Q}_{i+1/2} - \overline{G}_{i+1/2}}{\Delta_{i+1/2}\phi} \right) \right]} \tag{5.48}$$

Likewise, one can define an effective cell Peclet number for the north face, i.e., along the y–direction. The above definition is very similar to the definition given in Eq. (5.34) for the one–dimensional convection–diffusion equation and indicates the relative strength of local convection and the net local diffusion (physical plus numerical). Similar to model problem I (Section 5.4), while computing the coefficient of the nonlinear dissipation (second term in the denominator of the above expression), one can avoid the singularity that occurs when $\Delta_{i+1/2}\phi = 0$ by prescribing this coefficient to be zero when

$$\frac{\left| \Delta_{i+1/2}\phi \right|}{\phi_{characteristic}} \leq \varepsilon$$

where ε is a small positive number. For the present case we use $\varepsilon = 10^{-4}$. Note that the cell Peclet number for the central difference scheme is defined as

$$(P_e)_{central} = \frac{F_e}{D_e} \tag{5.49}$$

5.6.3 Boundary Treatment

At the control volumes adjacent to the boundary, we must use a scheme that utilizes only one neighbor on either side of the control point, since we do not have two neighbors available for the interface nearest to the boundary. For the scalar conservation law given by Eq. (5.1), the one–dimensional first–order TVD scheme, which forms the basis of the

second–order TVD scheme described in Section 5.2, has the following numerical flux on the right interface:

$$\tilde{f}_{i+1/2}^{n+1} = \frac{1}{2}\left[f_i + f_{i+1} - Q(a_{i+1/2})\Delta_{i+1/2}w\right]^{n+1} \tag{5.50}$$

and likewise for the left interface. Thus, for the two–dimensional case, the control volumes adjacent to the boundaries of the domain use different coefficients compared to the internal control volumes. Due to the staggered nature of the grid, the situation is different for the left and right border control volumes and the top and bottom border control volumes (shown in Fig. 2.1). For the u–component of velocity, the left and right border control volumes use the following coefficients:

$$\begin{aligned} A_W &= D_w + \frac{1}{2}F_w + \frac{1}{2}Q(a_{i-1/2})\varrho_w\Delta y \\ A_E &= D_e - \frac{1}{2}F_e + \frac{1}{2}Q(a_{i+1/2})\varrho_e\Delta y \\ A_S &= D_s + \frac{1}{2}F_s + \frac{1}{2}Q(a_{j-1/2})\varrho_s\Delta x \\ A_N &= D_n - \frac{1}{2}F_n + \frac{1}{2}Q(a_{j+1/2})\varrho_n\Delta x \end{aligned} \tag{5.51}$$

with $b=0$ and A_P equal to the sum of the above coefficients.

The situation is slightly different for the bottom and top border since the interface nearest to the boundary lies on the boundary itself. Thus, in the bottom border control volumes, for example, the diffusion coefficient is changed due to the fact that

$$(\delta y_s)_{south\ border\ C.V.} = 0.5(\delta y_s)_{internal\ C.V.} \tag{5.52}$$

which leads to a modification of the diffusion coefficient as follows:

$$D_{south\ border\ C.V.} \equiv D_s^* = 2D_s \equiv 2D_{internal\ C.V.} \tag{5.53}$$

The coefficient A_S for the bottom border control volumes is thus given by

$$A_S = D_s^* + \frac{1}{2}F_s + Q(a_{j-1/2})\varrho_s\,\Delta x \tag{5.54}$$

whereas the remaining coefficients are the same as before, namely, those given by Eq. (5.51). A similar treatment is required for the top border u–control volumes.

The above description is applicable to the border u–control volumes shown in Fig. 2.1. For the v–control volumes along the borders of the flow domain, the treatment for the left and right borders is analogous to the u–control volumes along the top and bottom borders. Similarly, the boundary treatment for the top and bottom v–control volumes is analogous to the left and right border u–control volumes.

5.7 Results of Two–Dimensional Incompressible Flows

In order to assess the performance of the controlled variation scheme (CVS) for recirculating flows, flows in a lid–driven cavity and over a backward facing step are chosen as test cases. As discussed earlier, the controlled variation scheme presented here can be viewed as the central difference scheme with an appropriate amount of nonlinear numerical dissipation. The $\overline{Q}$ flux illustrates the physical mechanism by which the CVS operates. It is repeated here to illustrate this mechanism:

$$\overline{Q}_{i+1/2} = \frac{1}{2} Q\left(a_{i+1/2} + \gamma_{i+1/2}\right) \Delta_{i+1/2}\phi$$

Here Q, given by Eq. (5.9), is the numerical dissipation and is a function of the local numerical characteristic speed. Since the local characteristic speed is nothing but the local convection speed, a high local convection speed, which implies a high local cell Peclet number, automatically selects a higher amount of numerical dissipation. However, if the local gradient ($\Delta_{i+1/2}\phi$) is negligible, this damping term is also negligible. A high value of $\Delta_{i+1/2}\phi$ which represents the local gradient of velocity and thus the local cell Peclet number, also prompts the use of a high (though controlled) amount of dissipation by the CVS. The $\overline{G}$ flux balances the $\overline{Q}$ flux in regions where numerical dissipation is not necessary and assumes a zero value in regions where $\Delta_{i+1/2}\phi$ and $\Delta_{i-1/2}\phi$ have an opposite sign. Thus high cell Peclet number situations are handled by the CVS by automatically triggering a variation control in the regions where required.

5.7.1 Driven Cavity Flow

The results for the driven cavity flow presented here correspond to a Reynolds number 1000 based on the length of the cavity and the velocity of the moving lid. Since the controlled variation scheme developed here regulates the numerical dissipation in the central difference scheme, it is illustrative to compare the results obtained using these two schemes. For this purpose, the streamfunction plots for the driven cavity flow using a 21x21 grid with Reynolds number 1000, using the central difference scheme and the controlled variation scheme (CVS), are shown in Fig. 5.6. Since this test problem involves large regions of flow domain with low cell Reynolds numbers, based on local velocity gradients and discussed in Chapter II (Section 2.4.1.1), the central difference scheme is expected to give satisfactory results. Also, since the CVS is more dissipative compared to the central difference scheme, it is expected to smear the solution profiles somewhat, compared to the central difference scheme. This is evident from Fig. 5.6 where it is observed that the maximum streamfunction value obtained by the CVS is less than that by the central difference scheme. However, in regions where the cell Peclet numbers are high, namely, the edges of the primary eddy in the cavity, especially the top corners of the cavity, the streamfunction contours obtained with the central difference scheme show some nonphysical wiggles. With the CVS, these wiggles are suppressed, as seen in Fig. 5.6(b). Thus, the CVS does indeed serve its purpose of suppressing spurious oscillations but its effect is not so apparent in the present test problem since the central difference scheme itself is quite satisfactory for the majority of the flow field. Also, the CVS contains numerical dissipation (compared to the central difference scheme) throughout the flow field, even where it is not strictly required for the present problem, thus causing overall smearing.

Next, we examine some of the velocity profiles obtained using the CVS. Fig. 5.7 shows the u–velocity profiles across the cavity along two vertical lines, namely, x=0.25 and 0.5. The u–velocity profiles at x=0.5 for successively refined grids show a monotonic convergence to the benchmark results of Ghia *et al.* (1982). The velocity profiles for x=0.25

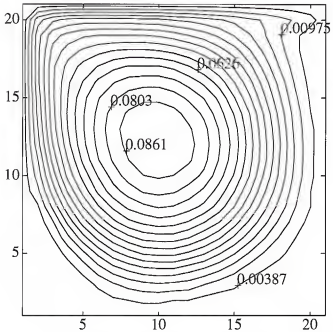

(a) Central difference scheme

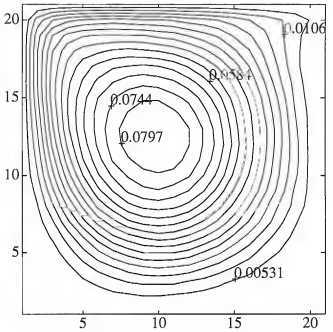

(b) Controlled variation scheme

Fig. 5.6. Streamfunction contours for cavity flow on 21x21 grid using different schemes; Re=1000.

have been plotted in Fig. 5.7(b) to confirm that the solution converges monotonically towards a grid independent solution throughout the flowfield, as the grid is refined; no benchmark solution profiles are available for this x–location. The above results demonstrate that physically, the CVS operates by injecting an extra amount of numerical dissipation into the central difference operator. In the original TVD scheme applied to the Euler equations, this dissipation is maximum in regions of discontinuities due to large amounts of $\overline{Q}$ introduced or at local extrema due to a zero value of $\overline{G}$. In the present case, no discontinuities are present in the flow field; here, the CVS regulates the amount of dissipation based on the detection of local extrema in the velocity profiles. Since the CVS is applied to the momentum equations, it is the gradients of u– and v–velocity components that are used to monitor the nonlinear dissipation injected into the respective momentum fluxes. The relative significance of the net numerical dissipation and the physical diffusion can be estimated by defining the following ratio:

$$Q^* - G^* = \frac{\left[\varrho \Delta y \frac{\left(\overline{Q}_{i+1/2} - \overline{G}_{i+1/2}\right)}{\Delta_{i+1/2}\phi}\right]}{D_{i+1/2}} \equiv \textit{Normalized viscosity} \tag{5.55}$$

Fig. 5.8 shows the contours of the net (Q*–G*) flux on the 21x21 grid for both the velocity components along both the directions. The values of (Q*–G*) flux are positive throughout the whole domain demonstrating that (Q*–G*) indeed represents the net dissipation, as discussed earlier. The larger values of (Q*–G*) exist in the regions of higher gradients. For example, the u–velocity profiles shown in Fig. 5.7 exhibit large gradients for the region confined between y=0.75 (j=15) and y=1.0 (j=21), approximately. Also, sharp gradients exist along the edges of the primary eddy, as seen from the streamfunction contours in Fig. 5.6. It is in these regions that the larger values of (Q*–G*) can be observed in Fig. 5.8.

As the grid is refined, the magnitude of (Q*–G*) will diminish since the local cell Peclet numbers, based on the velocity differences across the computational cells, decrease with grid refinement. This means that the effective dissipation injected by the CVS should

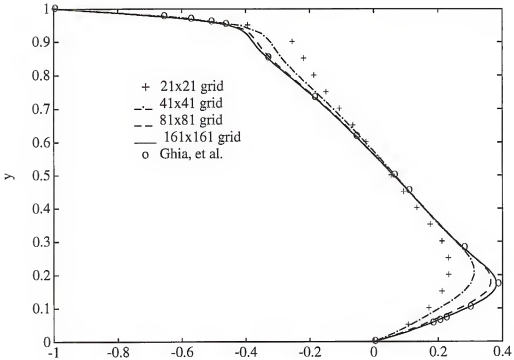

(a) u-velocity profiles along x=0.5 on various grids

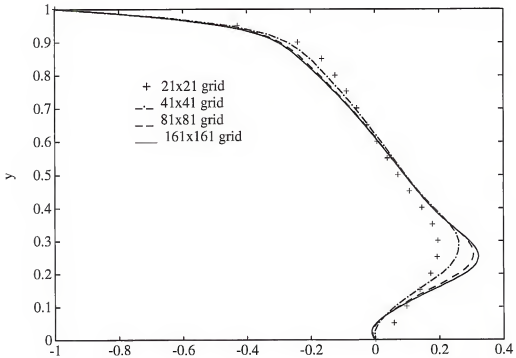

b) u-velocity profiles along x=0.25 on various grids

Fig. 5.7. Velocity profiles at selected locations for cavity flow using the CVS; Re=1000.

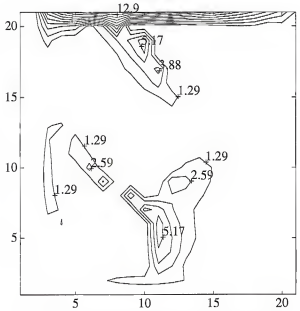

(a) u-control volumes along x-direction

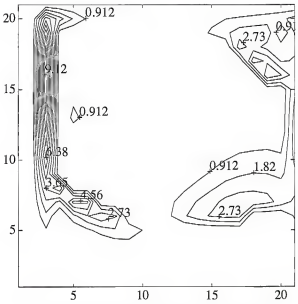

(b) u-control volumes along y-direction

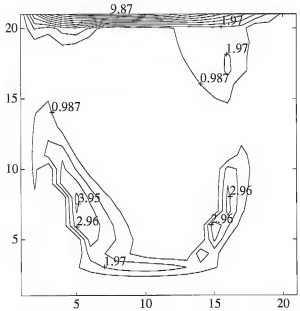

(c) v-control volumes along x-direction

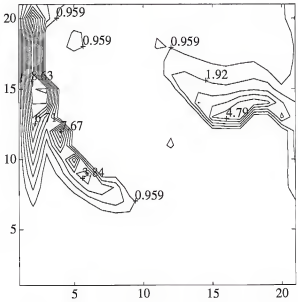

(d) v-control volumes along y-direction

Fig. 5.8. Normalized viscosity (Q*–G*) contours on 21x21 grid for cavity flow using the CVS; Re=1000.

decrease monotonically as the grid is refined. This is clearly evident from Fig. 5.9 where the (Q*–G*) flux distribution is plotted on four grids with nodes varying from 21x21 to 161x161. It is observed that the (Q*–G*) flux decreases monotonically in magnitude as the grid is refined. This serves as an illustration of the mechanism of the CVS. From the viewpoint of the central difference scheme, for a high Reynolds number flow, the local cell Peclet numbers will monotonically decrease with the refinement of the grid; so will the wiggles in the solution and the amount of diffusion selected by the controlled variation scheme is regulated accordingly.

It is illustrative to compare the cell Peclet number distributions for the central difference scheme and the CVS. In Chapter II (Section 2.4.1.1), we have chosen to use a cell Reynolds number based on the local gradient of velocity as an indicator of the relative magnitude of local convection and diffusion. However, such a definition will not serve our purpose of comparing the central difference scheme and the CVS since the local velocity gradients obtained using both these schemes are very close to each other. In order to understand the mechanism of the CVS whereby it introduces a net numerical dissipation into the central difference scheme, the definition of the effective cell Peclet number as given by Eq. (5.48) is more illustrative. The distribution of effective cell Peclet numbers is shown in Fig. 5.10 along both x– and y–directions. These contours are consistent with the general flow features; for example, the maximum cell Peclet number value (using either of the schemes) along the x–direction occurs in regions where u–velocity is the maximum. Likewise, the maximum cell Peclet numbers along the y–direction occur where the v–velocity is the maximum. A comparison of the contours obtained using the central difference scheme with those obtained using the CVS shows that the CVS reduces the effective cell Peclet number relative to the central difference scheme in regions where sharp gradients exist, notably along the edges of the primary eddy. For example, along the x–direction, we observe a reduction in the magnitude of the cell Peclet number (Fig. 5.10(a)) from –30 to –15 near the top center.

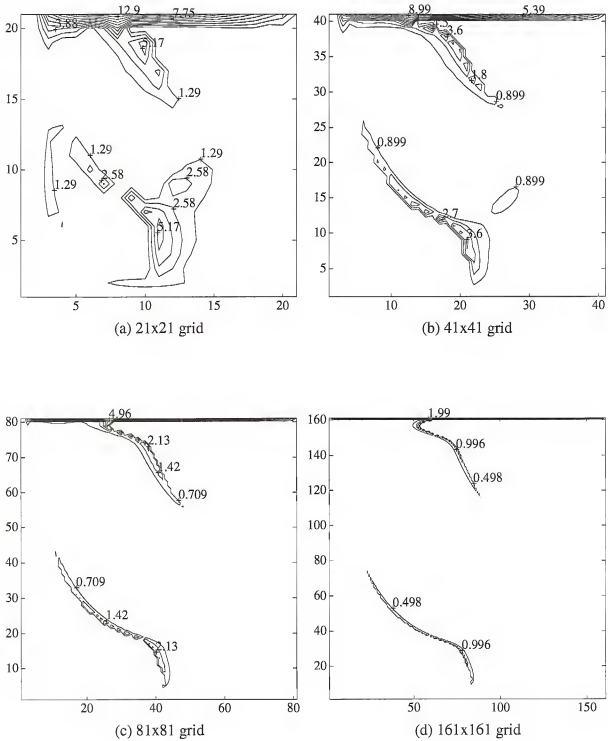

(a) 21x21 grid (b) 41x41 grid

(c) 81x81 grid (d) 161x161 grid

Fig. 5.9. Normalized viscosity (Q*–G*) along x–direction on various grids using the CVS; Re=1000.

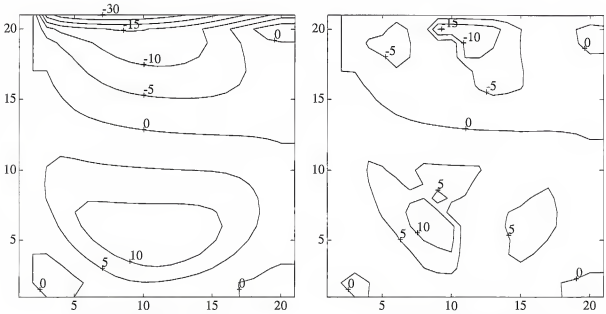

(i) Central difference scheme (ii) Controlled variation scheme

(a) Along x–direction

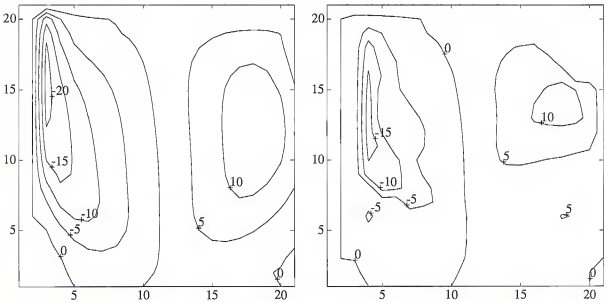

(i) Central difference scheme (ii) Controlled variation scheme

(b) Along y–direction

Fig. 5.10. Contours of effective cell Peclet number, defined in Eq. (5.48) and representing the ratio of local convection to diffusion (physical plus numerical) for cavity flow using the central difference scheme and the CVS; Re=1000.

Similarly, along the y–direction, the magnitude is reduced from –20 to –15 along the left center of the cavity (Fig. 5.10(b)).

5.7.2 Flow Over a Backward–Facing Step

The flow over a backward–facing step has been used in literature as a test problem for outflow boundary conditions (Gartling 1990). Moreover, it is a good test case for assessing numerical schemes for recirculating flows by virtue of the presence of multiple recirculation cells in the flow. The case studied here is the same as that investigated by Gartling (1990), namely, a flow with a Reynolds number *Re* of 800 based on the step height and the average inlet velocity. A parabolic velocity profile, corresponding to a fully developed channel flow, is specified at the inlet. The computational domain is terminated downstream at a distance equal to sixteen times the step height; this distance happens to be in the middle of the second recirculation zone (the first one being immediately downstream of the step). This serves as a good testing case for the numerical algorithm with an outflow boundary condition in terms of its interaction with a recirculation region right at the outflow boundary.

Once again, we perform a direct comparison between the CVS and the central difference scheme by plotting streamfunction contours and profiles of selected variables at a selected location. Streamfunction contours obtained with the CVS and the central difference scheme, shown in Fig. 5.11, are very similar to each other. Fig. 5.12 shows the profiles of u–velocity and vorticity at a location fourteen step heights downstream of the inlet, i.e., x=7. For comparison among various schemes, profiles obtained with the second–order upwind scheme (formulated in Chapter II, Section 2.2.3) and the FEM solution of Gartling (1990) are also plotted alongside those obtained with the CVS and the central difference scheme. Compared to the central difference scheme, while the CVS appears to be slightly more dissipative in regions of local extrema, it yields a sharper vorticity profile in

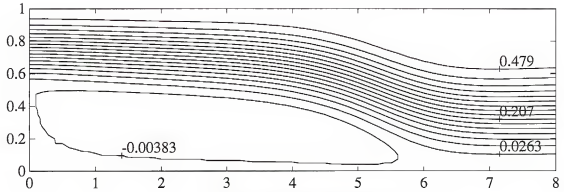

(a) Central difference scheme

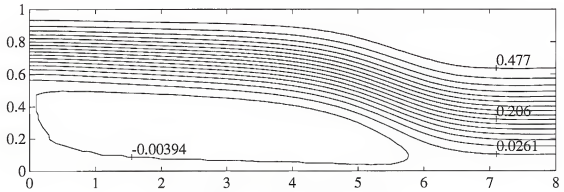

(b) Controlled variation scheme

Fig. 5.11. Streamfunction contours for backward–step flow using the central difference scheme and the CVS; Re=800.

the wall region. Overall, for this problem, the CVS is quite comparable to the central difference scheme as far as general solution features and accuracy are concerned.

Similar to the case of the driven cavity flow, it is illustrative to compare the cell Peclet number distributions for the central difference scheme and the CVS, shown in Fig. 5.13. Cell Peclet number contours are plotted along both x– and y–directions. These contours are consistent with the general flow features; for example, the maximum cell Peclet number value (using either of the schemes) along the x–direction occurs in the region next to the maximum inlet velocity. Likewise, the maximum cell Peclet numbers along the y–direction occur where the v–velocity is the maximum, namely, where the streamfunction contours (Fig. 5.11) bend down due to the presence of the second recirculation zone near the outflow

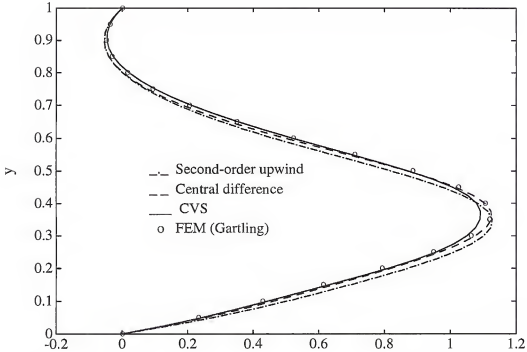

(a) u-velocity at x=7.0

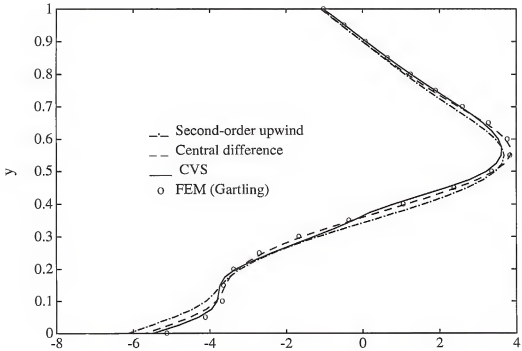

(b) Vorticity at x=7.0

Fig. 5.12. u–velocity and vorticity profiles at x=7.0 for backward–step flow using various schemes; Re=800.

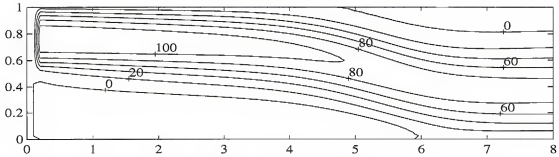

(i) Central difference scheme

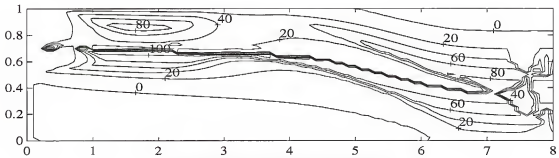

(ii) Controlled variation scheme

(a) Along x-direction

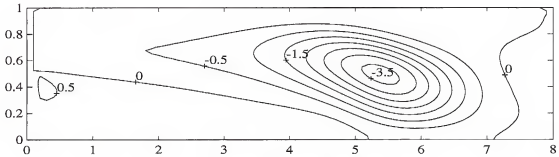

(i) Central difference scheme

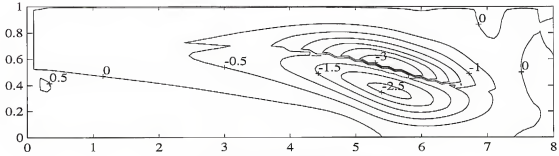

(ii) Controlled variation scheme

(b) Along y-direction

Fig. 5.13. Contours of effective cell Peclet number, defined in Eq. (5.48), for backward–step flow using the central difference scheme and the CVS; Re=800.

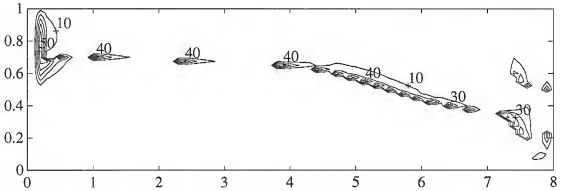

(a) Along x-direction

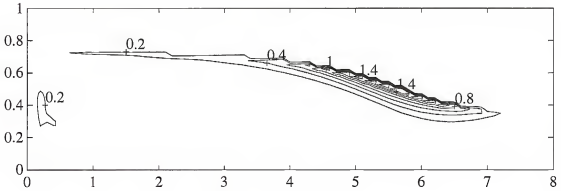

(b) Along y-direction

Fig. 5.14. Normalized viscosity (Q*–G*) contours along x– and y–directions using the CVS for backward–step flow; Re=800.

boundary. The smallest values of cell Peclet numbers occur in the two recirculation cells where both the components of velocity are the smallest. Similar to the case of driven cavity flow, the CVS introduces dissipation in regions where the flow gradients are high, thus reducing the effective cell Peclet numbers in these regions.

The contours of (Q*–G*), defined in Eq. (5.54), for the flow over the backward–facing step are shown in Fig. 5.14. It can be seen that the maximum amount of numerical dissipation is applied by the CVS in regions where the solution gradients are high. Along both x– and y–directions, the largest magnitude of numerical dissipation is introduced along the shear layer that separates the two recirculation cells, as seen in Fig. 5.14.

5.8 Concluding Remarks

In the present chapter, it has been shown that the modern TVD schemes, which were originally designed for suppressing spurious oscillations near discontinuities in solutions of hyperbolic systems of equations solved in a simultaneous manner, can indeed be extended in the form of a controlled variation scheme (CVS) within the framework of multidimensional pressure–based sequential solvers to compute incompressible, high cell Peclet number flows involving recirculation. Although the TVD property itself will no longer hold, the CVS can be used as an effective means for suppressing wiggles associated with the central difference scheme for high cell Peclet number flows. The controlled variation scheme employed in the present study is slightly more diffusive than the central difference scheme due to its very basic design philosophy which is based on an introduction of numerical damping, based on local first– and second–derivatives, in the central difference scheme in regions where the solution has steep variations. While collectively these fluxes introduce a net numerical diffusion into the solution, their effect decreases monotonically as the grid is refined. Compared to the central difference scheme, the use of the present controlled variation scheme leads to more smearing via the modification of cell Peclet numbers in a controlled manner. Based on this notion, the use of the controlled variation scheme is very effective in situations where the central difference scheme fails. An efficient implementation of the CVS for practical steady state computations, based on a linearized form of Harten's TVD scheme, has been identified in the present study. Overall, the idea of a controlled variation scheme, within the framework of an iterative pressure–based sequential solver, holds promise for complex flows with strong convective effects.

In the present chapter, the deficiencies of the central difference scheme are mainly observed in one–dimensional model problems; for multi–dimensional, laminar, recirculating flows, it has worked well. Thus, the true usefulness of the CVS, which is developed as a substitute for the central difference scheme, is not so apparent for laminar flows. Rather, it is for problems such as turbulent flows that are usually solved with

additional closure equations (such as the k–ε equations) that the CVS is truly useful. For such flows, the equations contain strong source terms besides possessing high convection strength, and the central difference scheme frequently breaks down because it offers poor accuracy, lacks the necessary numerical stability, and produces solutions that violate physical realizability. Attempts have been made to assess the performance of the CVS for turbulent flow problems, as will be discussed next.

CHAPTER VI
TURBULENT FLOW COMPUTATIONS

6.1 Background

The two–dimensional test cases investigated thus far have been limited to laminar flows in order to unequivocally assess the various convection schemes without the uncertainties introduced by additional physical and numerical complexities due to turbulence. Having addressed some key issues concerning convection schemes, especially the controlled variation scheme (CVS) developed in Chapter V, we now attempt to compute turbulent flows. The CVS, which employs nonlinear dissipation to augment the central difference flux, is expected to be more effective than the central difference scheme for turbulent flows. This is so because the strong convective effects inherent to turbulent flows (since turbulence occurs generally at high Reynolds numbers) can cause the central difference scheme to yield physically unrealizable solutions (most often in the form of wiggles). This is further compounded by unrealistic (e.g., negative) values of quantities such as the turbulent kinetic energy and the rate of dissipation of turbulent kinetic energy, which are used in closure models for turbulent flow computations. Additionally, the numerical stability of the overall algorithm is likely to be adversely affected. All these reasons make the CVS a more reasonable candidate by virtue of the physically reasonable solutions that it is expected to provide due to the nonlinear dissipation inherent to it. While attempting to solve some turbulent flows in this chapter, it must be emphasized that the focus is on the investigation of the utility of the CVS over the more conventional schemes (such as the

central difference and the first–order upwind schemes) while computing turbulent flows. No attempt is made here to assess the various closure models that have been developed to date.

The phenomenon of turbulence is still one of the most elusive areas in the physical sciences. Though the Navier–Stokes equations are generally considered to describe turbulent flows completely in the continuum regime, numerical simulations of general turbulent flows at high Reynolds numbers using the Navier–Stokes equations are not possible yet. This is because the time and length scales associated with turbulent flows are so small that in order to resolve them, a prohibitively large number of grid points and hence an enormous amount of computer storage (not yet available) is required. Hence, for practical computations, the flows are computed using the Navier–Stokes equations in an averaged form (e.g., Reynolds averaging) rather than the instantaneous form (Hinze 1959). The averaging process gives rise to new unknown terms representing the transport of mean momentum and heat flux by fluctuating quantities. These undetermined terms are called the Reynolds stresses or heat fluxes and they lead to the well known closure problem for turbulent flow computations. In order to determine these terms, turbulence models are required; they consist of a set of algebraic or differential equations.

Several one–point turbulence models have been developed over the past years; they can be broadly classified into two categories, namely,

(a) eddy viscosity models which are based on the assumption that the Reynolds stresses are a local property of the mean flow and are related to the mean flow gradients via a turbulent viscosity (e.g., Launder & Spalding 1974), and

(b) Reynolds stress models which assume that the Reynolds stresses are dependent variable quantities and can be solved directly from their own transport equations (which are derived from the Navier–Stokes equations), along with some modelling equations (e.g., Launder *et al.* 1973).

The derivation of these models has been largely based on intuition, empirical correlation, and to some extent, constraints set forth by physical realizability (Lumley 1978). More recently,

turbulence models have been developed with more rigor and mathematical formalism based on the Renormalization Group (RNG) theory (Yakhot & Orszag 1986, Speziale & Thangam 1992).

Among the eddy viscosity models, a further classification can be made based on the number of differential equations utilized. Thus, zero–, one–half–, one– and two–equation eddy viscosity models have been developed. Of these eddy viscosity models, the two–equation k–ε model (Jones & Launder 1972, Launder & Spalding 1974) has been the most successful and is used the most, especially for engineering applications. It is this model that has been chosen for use in the present study. It must be reiterated that the focus is on the investigation of the effectiveness of convection schemes previously developed, especially the CVS, for computation of turbulent recirculating flows and not on the development or a comparative assessment of turbulence models.

The k–ε model uses transport equations to solve for two turbulent quantities, namely, the turbulent kinetic energy (k) and the rate of its dissipation (ε). The transport equations for these quantities have strong source terms representing the production and destruction of these quantities. Due to the presence of these source terms as well as the high convective effects inherent to turbulent flows, the use of central differencing may not be satisfactory, as discussed earlier. In the present chapter, we investigate the performance of the CVS along with the first–order upwind, hybrid and second–order upwind schemes, using a high Reynolds number flow over a backward–facing step as a test case. First, we describe the relevant equations for the mean flow and the k–ε model.

6.2 Basic Equations

6.2.1 Equations of Mean Flow

Replacing the various dependent variables with their mean and fluctuating components (e.g., $u_{instantaneous} = u + u'$) in the Navier–Stokes equations and time averaging the equations yields the so–called Reynolds averaged equations:

Continuity:
$$\frac{\partial \varrho}{\partial t} + \frac{\partial}{\partial x_j}\left(\varrho u_j\right) = 0 \tag{6.1a}$$

Momentum:
$$\frac{\partial}{\partial t}\left(\varrho u_i\right) + \frac{\partial}{\partial x_j}\left(\varrho u_i u_j\right) = -\frac{\partial p}{\partial x_i} + \frac{\partial}{\partial x_j}\left(\tau_{ij} - \varrho\overline{u_i' u_j'}\right) \tag{6.1b}$$

Note that the conventional indicial notation has been employed in the above equations. The equations do not form a closed set in the sense that they contain the unknown second–order moments $\overline{u_i' u_j'}$, which are the well known Reynolds stress terms arising from the nonlinearity of the convection terms.

As mentioned earlier, we have chosen the k–ε model, which is an eddy viscosity model, for the present study. Eddy viscosity models are based on the assumption that the Reynolds stresses are a local property of the mean flow and are related to the mean flow gradients via a turbulent viscosity as shown below

$$-\varrho\overline{u_i' u_j'} = \mu_t\left(\frac{\partial u_i}{\partial x_j} + \frac{\partial u_j}{\partial x_i}\right) \tag{6.2}$$

where μ_t is some turbulent viscosity which still needs to be modeled.

The turbulent viscosity μ_t is the vehicle through which the time and length scale effects of turbulent flows are introduced into the equations of mean flow. Thus, modeling μ_t requires specification of local length and time scales (or equivalently local velocity and length scales). The k–ε model provides the velocity scale via the modeled turbulent kinetic energy (k) and the length scale via a combination of k and the rate of viscous dissipation of turbulent kinetic energy (ε). Dimensional analysis yields the turbulent viscosity as

$$\mu_t = \frac{C_\mu \varrho\ k^2}{\varepsilon} \tag{6.3}$$

where C_μ is a proportionality constant to be defined later.

With the above assumptions, the momentum equations can now be written as

$$\frac{\partial}{\partial t}\left(\varrho\phi\right) + \frac{\partial}{\partial x}\left(\varrho u\phi\right) + \frac{\partial}{\partial y}\left(\varrho v\phi\right) = \frac{\partial}{\partial x}\left(\mu_{eff}\frac{\partial \phi}{\partial x}\right) + \frac{\partial}{\partial y}\left(\mu_{eff}\frac{\partial \phi}{\partial y}\right) - \left(\frac{\partial p}{\partial x}\ or\ \frac{\partial p}{\partial y}\right) \tag{6.4}$$

where $\phi = u$ *or* v, with $\mu_{eff} = \mu + \mu_t$. Here μ represents the laminar viscosity and μ_t the turbulent viscosity.

6.2.2 k–ε Equations

The transport equations for k and ε, which are derived from the Navier–Stokes equations, have the same basic form, after the modelling assumptions are incorporated. They can be expressed in the following form:

$$\frac{\partial}{\partial t}(\varrho\phi) + \frac{\partial}{\partial x}(\varrho u\phi) + \frac{\partial}{\partial y}(\varrho v\phi) = \frac{\partial}{\partial x}\left(\Gamma\frac{\partial\phi}{\partial x}\right) + \frac{\partial}{\partial y}\left(\Gamma\frac{\partial\phi}{\partial y}\right) + R_1 + R_2 \qquad (6.5)$$

where

$$\Gamma = \begin{cases} \mu + \dfrac{\mu_t}{\sigma_k} & \text{for } \textit{the } k-\textit{eqn.} \quad (6.6a) \\ \mu + \dfrac{\mu_t}{\sigma_\varepsilon} & \text{for } \textit{the } \varepsilon-\textit{eqn.} \quad (6.6b) \end{cases}$$

$$R_1 = \begin{cases} \mu_t\, R & \text{for } \textit{the } k-\textit{eqn.} \quad (6.7a) \\ \dfrac{C_1\, \mu_t\, \varepsilon\, R}{k} & \text{for } \textit{the } \varepsilon-\textit{eqn.} \quad (6.7b) \end{cases}$$

with

$$R = 2\left[\left(\frac{\partial u}{\partial x}\right)^2 + \left(\frac{\partial v}{\partial y}\right)^2\right] + \left[\frac{\partial u}{\partial y} + \frac{\partial v}{\partial x}\right]^2 \qquad (6.8)$$

and

$$R_2 = \begin{cases} -\varrho\,\varepsilon \equiv -\left(\dfrac{C_\mu\,\varrho\,{}^2 k^*}{\mu_t}\right) k & \text{for } \textit{the } k-\textit{eqn.} \quad (6.9a) \\ -C_2\varrho\,\dfrac{\varepsilon^2}{k} \equiv -\left(C_2\,\varrho\,\dfrac{\varepsilon^*}{k^*}\right)\varepsilon & \text{for } \textit{the } \varepsilon-\textit{eqn.} \quad (6.9b) \end{cases}$$

In the k–ε equations, R represents the generation of k from the mean flow by turbulent shear stress and ε represents the rate of viscous dissipation of k to heat by the smallest turbulent eddies. σ_k and $\sigma\varepsilon$ are the Prandtl numbers; their values are given later. The above

equations are integrated over the control volume and then discretized in a manner similar to the momentum equations, described in Chapter II.

6.2.3 Boundary Conditions and Wall Treatment

The treatment of inflow and outflow boundaries of the computational domain is done in the usual manner. All the variables at the inlet are specified or estimated. For example, the inflow velocities are specified and k is estimated as a fraction of the square of the inlet velocity whereas ε is estimated from k and a suitable length scale representing the size of turbulent eddies (usually specified as a fraction of the inlet dimension). The variables at the outflow boundaries are estimated by a zero gradient condition which is based on the assumption that the flow is convection–dominated.

Near wall boundaries, the local Reynolds numbers are low and viscous effects are important; thus the k–ε model cannot be utilized since it is valid only for high Reynolds numbers. Moreover, steep variations in properties close to the wall need a large number of grid points for proper resolution. To handle this, two approaches are commonly employed which involve low Reynolds number versions of the k–ε model (Jones & Launder 1972, 1973, Patel *et al.* 1985) and the use of wall functions (Launder & Spalding 1972). The former requires a relatively fine grid resolution in the wall region. The latter is easier to implement, but lacks a fundamental justification of the formulas adopted. In practise, however, the wall function approach has often produced results of accuracy comparable to the low Reynolds number approach (Viegas *et al.* 1985), especially for recirculating flows. In the present study, the wall function approach has been employed and is described next.

Close to the walls, a one–dimensional Couette flow analysis is generally made. The wall layer is assumed to have a constant shear stress across it. The momentum equation reduces to a simple non–dimensional form given by

$$\tau = (\mu + \mu_t)\frac{\partial u}{\partial y} \tag{6.10a}$$

where $u \equiv u_P$ is the velocity (parallel to the wall) at the point P (shown in Fig. 6.1), which is at

a distance $y \equiv y_P$ from the wall. The above equation can be rewritten, using the wall shear stress and friction velocity, as

$$\frac{\tau}{\tau_w} = \left(1 + \frac{\mu_t}{\mu}\right)\frac{\partial u^+}{\partial y^+} \tag{6.10b}$$

where τ_w is the shear stress at the wall. The local Reynolds number (or the non–dimensional distance of point P from the wall), y^+, is defined as

$$y^+ = \frac{\varrho u_\tau y}{\mu} \tag{6.11a}$$

and the non–dimensional velocity u^+ is given by

$$u^+ = \frac{u}{u_\tau} \tag{6.11b}$$

where u_τ is the friction velocity at the wall given by

$$u_\tau = \sqrt{\frac{\tau_w}{\varrho}} \tag{6.12}$$

For a turbulent boundary layer over a solid flat plate, experimental evidence indicates that the wall region is composed of three zones (Hinze 1959), namely:

(a) the viscous sublayer ($0 < y^+ < 5$) which is dominated by viscous effects,

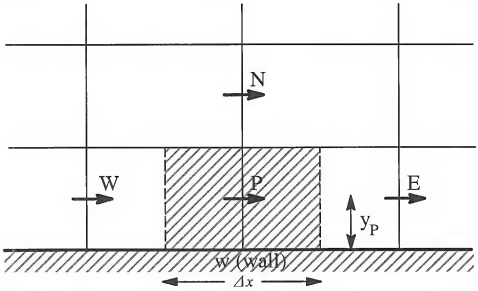

Fig. 6.1 Wall treatment for velocity component parallel to a wall boundary.

(b) the inertial sublayer ($30 < y^+ < 400$) where flow is fully turbulent but $\tau = \tau_w$, and (c) the transition or buffer zone ($5 < y^+ < 30$) where neither the viscous effects nor turbulent effects dominate.

A convenient engineering practise, as in the present study, is to discard the buffer zone by defining $y^+ = 11.63$ as the point above which the flow is assumed fully turbulent and below which is dominated by viscous effects. At this location the linear velocity profile of the viscous sublayer meets the logarithmic velocity profile in the inertial sublayer.

Viscous sublayer ($y^+ < 11.63$)

In the viscous sublayer , $\mu_t/\mu \ll 1$, and the assumption $\tau = \tau_w$ leads to

$$u^+ = y^+ \quad \Rightarrow \quad \tau = \tau_w = \frac{\mu u_P}{y_P} \tag{6.13}$$

Inertial sublayer ($y^+ > 11.63$)

In the inertial sublayer , $\mu_t/\mu \gg 1$ and again the assumption $\tau = \tau_w$ along with

$$\mu_t = \varrho \varkappa \, y \, u_\tau \tag{6.14}$$

leads, after integrating Eq. (6.10b), to

$$u^+ = \frac{1}{\varkappa} \log_e y^+ \equiv \frac{1}{\varkappa} \log_e \left(E y^+\right) \tag{6.15}$$

In the above, $\varkappa$ is the von Karman constant. The transport equation for the turbulent kinetic energy (k), which is defined by Eqs. (6.5–6.9), reduces, after performing a one–dimensional analysis, assuming a constant shear stress in the inertial sublayer, to the following:

$$-\overline{u'v'} \frac{du}{dy} = \varepsilon \tag{6.16}$$

Using the definition of Reynolds stress given by Eq. (6.2) and that of ε from Eq. (6.3), and the definition of τ from Eq. (6.10a) with $\mu_t/\mu \gg 1$, we get the following:

$$\tau \equiv \tau_I = \varrho \, k \, C_\mu^{1/2} \tag{6.17}$$

Using Eq. (6.11b), Eq. (6.12) and the fact that $\tau_I \cong \tau_w$, we get

$$u^+ \cong \frac{u\sqrt{\varrho\tau_I}}{\tau_W} \quad \Rightarrow \quad \tau_W = \frac{u}{u^+}\ \varrho\ c_\mu^{1/4}\ k^{1/2} \tag{6.18}$$

Then using the definitions (6.17) and (6.15), we finally get for the shear stress at the wall:

$$\tau_W = \frac{\varrho\ c_\mu^{1/4}\ k^{1/2}\ \varkappa\ u}{\log_e(Ey^+)} \tag{6.19}$$

where y^+ is evaluated from

$$y^+ = \frac{y\sqrt{\tau_W/\varrho}}{\nu} \cong \frac{y\ \varrho\ C_\mu^{1/4}\ k^{1/2}}{\mu} \tag{6.20}$$

Also, from Eq. (6.17) and (6.14) and the definition of ε from Eq. (6.3), we obtain the following form for ε in the inertial sublayer:

$$\varepsilon_I = \frac{C_\mu^{3/4}\ k^{3/2}}{\varkappa\ y_P} \tag{6.21}$$

Implementation of the momentum equations near wall boundaries

The discretized equation for the momentum equations for u– and v–control volumes has already been presented in Chapter II, in the form of Eq. (2.6). Near a wall boundary, such as the one shown in Fig. 6.1, the usual shear stress expression given in Eq. (6.4), i.e.,

$$\tau = \mu_{eff}\frac{\partial u}{\partial y}$$

is replaced by $\tau = \tau_w$ where τ_w is given by Eq. (6.13) or (6.19) depending on whether the point P lies in the viscous sublayer ($y^+ < 11.63$) or the inertial sublayer ($y^+ > 11.63$). The usual shear force expression in the discretized equations is suppressed by setting $A_S=0$ in Eq. (2.6) and τ_w is incorporated through source terms, either as a part of the explicit source term b or implicitly as a part of the coefficient A_P.

The above treatment is imparted only to the velocity component parallel to a wall boundary; thus, the v–velocity component near a left or a right wall boundary is also treated in the above manner. The velocity component perpendicular to a wall boundary is treated in the usual manner as detailed in Chapter II.

Implementation of the k–ε equations near wall boundaries

The turbulent kinetic energy at the point P near a wall, k_P, is obtained from the usual k–balance, but the flux expression at the wall boundary is suppressed by setting $A_S=0$ (for the bottom boundary shown in Fig. 6.2). The evaluation of the source term for the k–equation is modified by noting that the second term in R given by Eq. (6.8) can be simplified near the wall as

$$\mu_t\left(\frac{\partial u}{\partial y}+\frac{\partial v}{\partial x}\right)^2 \cong \tau_S\left(\frac{u_P-u_S}{y_P}\right) \tag{6.22}$$

where $u_S=0$ at the wall boundary, τ_S is the average of neighboring values of τ_W and u_P is the average of neighboring value of u. Moreover, the dissipation term in the k–equation near the wall is extended to the viscous sublayer by modifying it as

$$\varepsilon \cong \frac{c_\mu^{3/4}\, k^{3/2}\, u^+}{y_P} \tag{6.23}$$

where u^+ is defined by either Eq. (6.13) for the viscous sublayer or Eq. (6.15) for the inertial sublayer. Also, for lack of better knowledge, the diffusion of k to the wall is set to zero.

The value of ε reaches its maximum value at the walls which is an unknown, unlike the value of k which falls to zero at the wall. The ε–equation itself reduces to a simple form

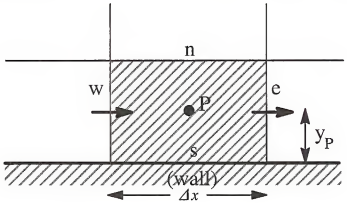

Fig. 6.2 Wall treatment for k and ε .

but in the computation, the value of ε near the wall boundaries is estimated from the equilibrium expression given by Eq. (6.21), and not from the usual ε–balance since we are at a loss to modify the coefficient A_S out of shear ignorance.

Values of the constants used in the $k-\varepsilon$ model

According to the recommendations of Launder and Spalding (1974), the various constants used in the $k-\varepsilon$–model assume the following values:

$$C_\mu = 0.09 \qquad C_1 = 1.44 \qquad C_2 = 1.92 \qquad \sigma_k = 1.0 \qquad \sigma_\varepsilon = 1.3 \tag{6.23}$$

The von Karman constant $\varkappa$ has the value 0.4187. The quantity E is a function of wall roughness, streamwise pressure gradient, etc. For a smooth impermeable wall with negligible streamwise pressure gradient, it is assigned the value 9.793.

6.3 Computation of Turbulent Flow Over a Backward–Facing Step

In this section, we present results of the computation of a turbulent flow over a backward–facing step, which is quite often used a test case for assessing various schemes and turbulent models for turbulent recirculating flows. The length of the rectangular computational domain studied here is 8 units and the height 1 unit. The ratio of the step height to the outflow height is 1:3.33. A uniform inlet velocity profile is prescribed and the inlet Reynolds number is $1.32\text{x}10^5$ based on the inlet velocity and the outflow height. The inlet values of turbulent kinetic energy (k) are prescribed as $0.03u_{inlet}^2$ and the rate of viscous dissipation (ε) is estimated from the inlet value of k and a length scale, which is taken to be three–hundreths of the inlet height. Speziale and Thangam (1992) have used a similar geometry and Reynolds number for computing turbulent flow over a backward–facing step; however, they prescribe the inlet velocity profile based on an experimental study by Eaton and Johnston (1980).

For the k–ε equations, the conventional hybrid scheme is used. The hybrid scheme is equivalent to the central difference scheme when the magnitude of the local cell Peclet

number is less than or equal to 2. For other values of the local cell Peclet number, it is equivalent to the first–order upwind scheme with the physical diffusion set to zero. Thus it aims to avoid the wiggles associated with the central difference scheme for convection dominated flows while reducing the excessive diffusion associated with the first–order upwind scheme. It is important to note that the central difference scheme is not a viable scheme for the k–ε equations because of the strong convective effects associated with turbulent flows as well as the presence of strong source terms (generation and dissipation of k, for example) in these equations, which can cause this scheme to yield physically unrealizable results and/or numerical instability.

Four different convection schemes are employed for the momentum equations, namely, first–order upwind scheme, hybrid scheme, second–order upwind scheme and controlled variation scheme (CVS). Three different grids are used, namely, those consisting of 41x21, 81x41 and 121x61 nodes, respectively. The central difference scheme is found to be unstable on all three grids, as expected. The streamfunction plots obtained with the various schemes on the 81x41 grid are shown in Fig. 6.3. It can be observed that a region of recirculating flow exists immediately downstream of the backward–facing step, the size of which is substantially smaller than the one obtained for laminar flow in Chapter V. Moreover, there is no other recirculation cell near the top boundary, as in the laminar flow case. All four convection schemes yield very similar flow patterns with a slight variation in the computed reattachment length, x_R, of the recirculating flow region. The CVS and the hybrid scheme yield very similar values of x_R/H (namely, 4.92 and 4.94, respectively) where H is the step height. The second–order upwind yields x_R/H=4.83 and the first–order upwind yields x_R/H=4.63.

Plots of instantaneous u–velocity profiles at three different streamwise locations for the three successively refined grids are shown in Figs. 6.4, 6.5 and 6.6, respectively. The first two locations are within the recirculation cell, the first (x/H=1.33) being close to the inlet and the second (x/H=3.33) close to the reattachment point. The third streamwise location is near

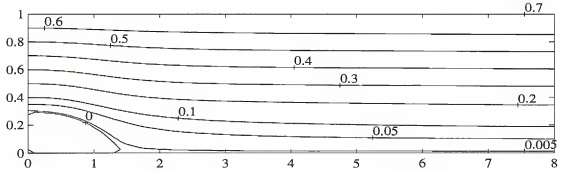

(a) First-order upwind scheme; $x_R/H=4.63$

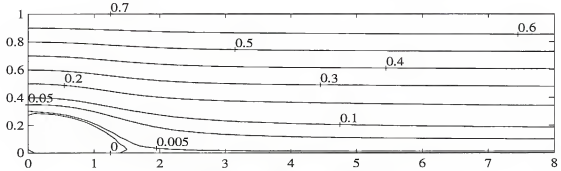

(b) Hybrid scheme; $x_R/H=4.94$

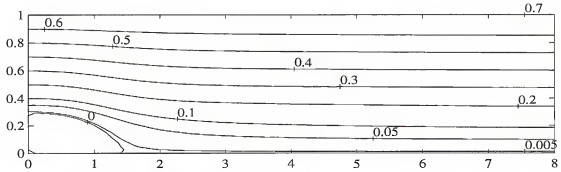

(c) Second-order upwind scheme; $x_R/H=4.83$

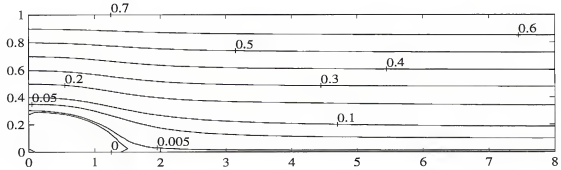

(d) Controlled variation scheme; $x_R/H=4.92$

Fig. 6.3. Streamfunction contours of turbulent flow over a backward–facing step on the 81x41 grid using various convection schemes for the momentum equations.

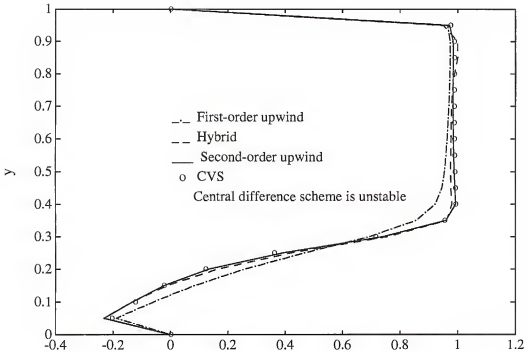

(a) u-velocity profiles at x=0.4, i.e., x/H=1.33.

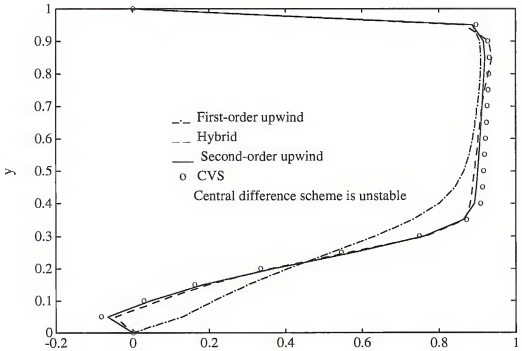

(b) u-velocity profiles at x=1.0, i.e., x/H=3.33.

Fig. 6.4. Instantaneous u–velocity profiles for turbulent flow over a backward–facing step at various streamwise locations using four convection schemes on the 41x21 grid.

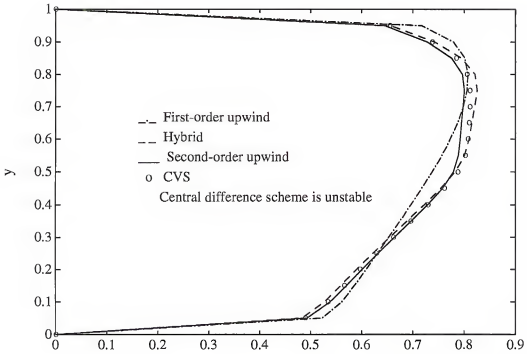

(c) u-velocity profiles at x=7.0, i.e., x/H=23.33.

Fig. 6.4. Continued

the outlet. It is observed that all four convection schemes yield qualitatively similar solution profiles, especially on the finer grids. The first–order upwind scheme yields comparatively more smeared profiles, as especially evident from the profiles obtained on the 41x21 grid, shown in Fig. 6.4. The hybrid scheme, though quite satisfactory for the present flow computation, exhibits slight overshoots near sharp gradients in the profiles for the 41x21 and the 81x41 grid, as seen in Figs. 6.4 and 6.5. In these regards, the second–order upwind and the CVS are the most satisfactory, and yield nearly identical profiles at all three streamwise locations on the finer grids, namely the 81x41 and 121x61 grids; on the coarsest grid, they exhibit slightly different solution profiles. As the grid is refined to 121x61 nodes (Fig. 6.6), the hybrid, second–order upwind and controlled variation schemes all yield almost identical results; the first–order scheme, however, still exhibits slight smearing of the profiles. It

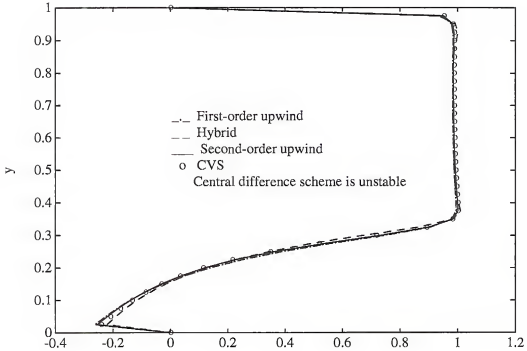

(a) u-velocity profiles at x=0.4, i.e., x/H=1.33.

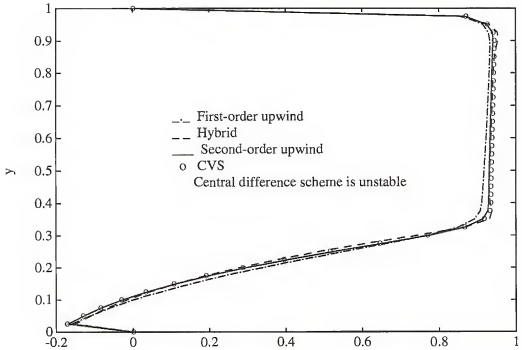

(b) u-velocity profiles at x=1.0, i.e., x/H=3.33.

Fig. 6.5. Instantaneous u–velocity profiles for turbulent flow over a backward–facing step at various streamwise locations using four convection schemes on the 81x41 grid.

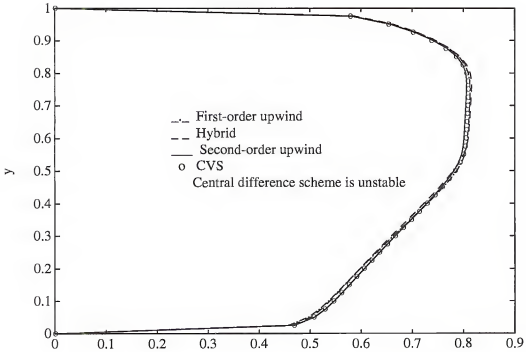

(c) u-velocity profiles at x=7.0, i.e., x/H=23.33.

Fig. 6.5. continued.

should be pointed out again that the central difference scheme is unstable for these turbulent flow computations.

Similar to the case of laminar flow over a backward–facing step presented in Chapter V, it is illustrative to plot contours of normalized viscosity employed by the CVS for the computation of turbulent flow over the step. It can be observed from Fig. 6.7 that large amounts of numerical dissipation are employed by the CVS in regions of large gradients, especially the region near the inlet and the recirculation region. Also, the magnitude of normalized viscosity reduces monotonically as the grid is successively refined. On the finest grid (121x61 nodes), the CVS employs virtually no numerical dissipation in the majority of the flowfield; only the region near the inlet and the wall regions which have high shear stresses require high values of numerical dissipation.

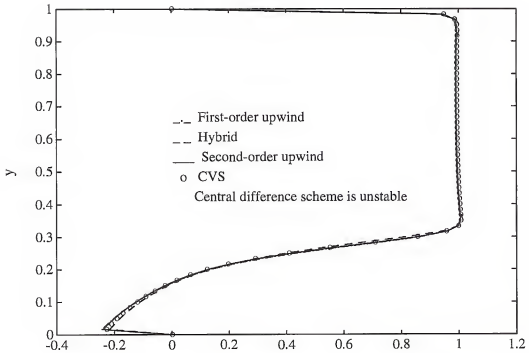

(a) u-velocity profiles at x=0.4, i.e., x/H=1.33.

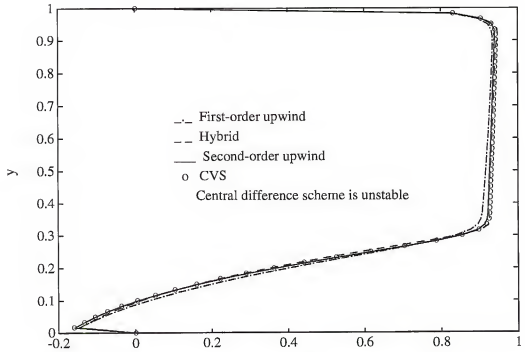

(b) u-velocity profiles at x=1.0, i.e., x/H=3.33.

Fig. 6.6. Instantaneous u–velocity profiles for turbulent flow over a backward–facing step at various streamwise locations using four convection schemes on the 121x61 grid.

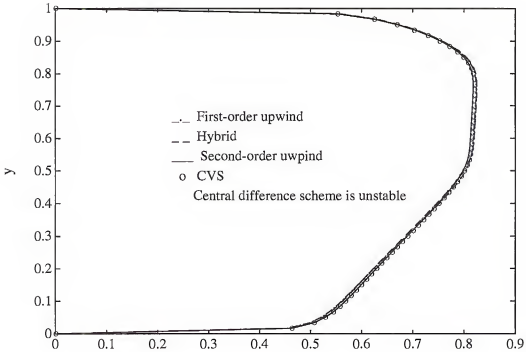

(c) u-velocity profiles at x=7.0, i.e., x/H=23.33.

Fig. 6.6. continued.

It is evident from the above results that the CVS is an accurate and stable scheme for computing turbulent flows. The central difference scheme is unstable for these flows, and the extra nonlinear dissipation that is inherent to the CVS is responsible for the stability of the computation as well as the physical realizability of the solution.

6.4 Concluding Remarks

It has been shown in this chapter that the controlled variation scheme (CVS) developed in Chapter V, is indeed an effective scheme for the computation of turbulent recirculating flows. The central difference scheme breaks down for these kinds of flows and thus one has to resort to different convection schemes. The first–order upwind has quite often been used to resolve this problem due to the numerical diffusion inherent to it. It is demonstrated that the CVS, which also possesses numerical dissipation, but is of a

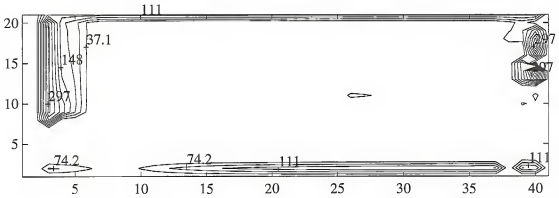

(a) 41x21 Grid

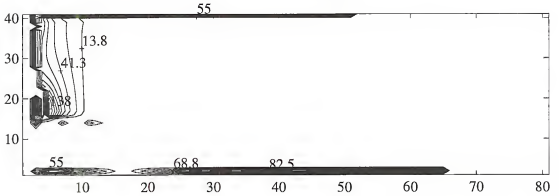

(b) 81x41 Grid

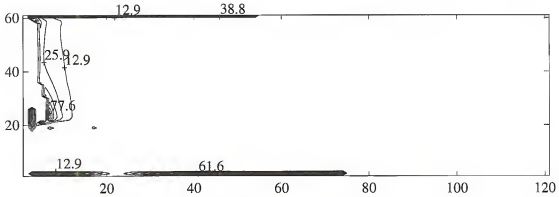

(c) 121x61 Grid

Fig. 6.7. Normalized viscosity (Q*–G*) contours for turbulent flow over the backward–facing step on various grids.

higher–order accuracy compared to the first–order upwind scheme, is an effective alternative. The second–order upwind scheme is also shown to yield satisfactory results for turbulent flow computations.

CHAPTER VII
SUMMARY AND SUGGESTIONS FOR FUTURE WORK

Several issues related to the treatment of convection and source terms in the Navier–Stokes equations are addressed. The control volume formulation is adopted within the framework of a pressure–based sequential algorithm. Two approaches for effectively treating convection terms are investigated. The first approach entails the use of different shape functions to estimate the convective fluxes at the control volume interfaces, leading to the first–order upwind, central difference, second–order upwind and QUICK schemes. It is shown that conservative and consistent formulations of these schemes, especially the higher–order upwind schemes (second–order upwind and QUICK), along with consistent boundary treatments are essential to achieve accuracy in the solution. It is further shown that a unified formulation of these higher–order upwind schemes, with the first–order upwind scheme as the basis and the balance of the flux treated as part of the source term, is more robust in terms of stability and convergence properties of the overall algorithm.

The second approach for treating convection terms adopts the viewpoint of an appropriate amount of dissipation injected into a basic higher–order scheme. To this end, the formalism of the sophisticated TVD schemes, which have been heretofore used as shock capturing schemes in simultaneous solvers, is extended to sequential solvers. This leads to two new issues, namely, an appropriate definition of local characteristic speeds on which the nonlinear dissipation employed by the TVD schemes is based, and the handling of the pressure gradient terms which appear as source terms in sequential formulations. It is shown that the local characteristic speeds can be coordinated by assigning them the values of the local convection speeds and the pressure gradient terms can be handled by an appropriate

source term treatment such as MacCormack's predictor–corrector method or Strang's operator–splitting method. Moreover, some key parameters used by the TVD schemes implemented in simultaneous solvers, are interpreted differently when these schemes are extended to sequential solvers. Overall, it is demonstrated that one can effectively implement TVD schemes in sequential solvers to achieve accuracy comparable to simultaneous solvers.

Based on the above, a controlled variation scheme (CVS) is developed and implemented in the two–dimensional pressure–based algorithm to compute laminar and turbulent recirculating flows. It is shown that the CVS operates by injecting nonlinear dissipation in regions of sharp gradients in the flowfield, thus reducing the effective local cell Peclet numbers. It is demonstrated to be an effective substitute for the central difference scheme, more so for turbulent flows for which the central difference scheme offers unacceptable accuracy and stability.

The issue of source terms in Navier–Stokes equations is also addressed. Utilizing a longitudinal combustion instability problem, which possesses a strong heat release source term, it is demonstrated that source terms can be stiff enough to cause spurious oscillations in the solution profiles as well as numerical instability. Special source term treatments such as MacCormack's predictor–corrector and Strang's operator–splitting techniques are shown to be effective alternatives for extra dissipation commonly employed to resolve these problems.

As mentioned at the beginning of this work, pressure–based algorithms are very attractive due to their capability of handling a wide range of flows– –from subsonic to hypersonic– –as well as a varying number of governing equations, without the need to restructure the entire algorithm. The present work has further strengthened this viewpoint by illustrating that advanced methodologies, such as higher–order upwind and modern shock capturing schemes as well as source term treatments, can indeed, with some modifications, be effectively employed in these pressure–based solvers.

The present study has laid the foundation for further work involving pressure–based solvers for computing flows with more complex fluid physics. Future work should involve an extension of the convection schemes developed here to compressible flows. Also the source term treatments employed in the present work need to be extended to multi–dimensional incompressible and compressible flows involving complex physical processes like combustion and chemical reactions.

REFERENCES

Atias, M., Wolfshtein, M. & Israeli, M. 1977 Efficiency of Navier–Stokes Solver, *AIAA J.* 15, 263–266.

Baum, J.D. & Levine, J.N. 1982 Numerical Techniques for Solving Nonlinear Instability Problems in Solid Rocket Motors, *AIAA J.* 20, No. 7, 955–961.

Baum, J.D. & Levine, J.N. 1985 A Critical Study of Numerical Methods for the Solution of Nonlinear Hyperbolic Equatiojns for Resonance Systems, *J. Comp. Phy.* 58, 1–28.

Bloxidge, G.J., Dowling, A.P., & Langhorne, P.J. 1985 Reheat Buzz: An Acoustically Coupled Combustion Instability. Part 2. Theory, *J. Fluid Mech.* 193, 445–473.

Book, D.L., Boris, J.P. & Hain, K. 1975 Flux–Corrected Transport II: Generalizations of the Method, *J. Comp. Phy.* 18, 248–283.

Boris, J.P. & Book, D.L. 1973 Flux Corrected Transport, I SHASTA, A Fluid Transport Algorithm That Works, *J. Comp. Phy.* 11, 38–69.

Braaten, M.E. & Shyy W. 1987 A Study of Pressure Correction Methods with Multigrid for Viscous Flow Calculations in Non–Orthogonal Curvilinear Coordinates, *Numer. Heat Transf.* 11, 417–442.

Burgraff, O. R. 1966 Analytical and Numerical Studies of the Structure of Steady Separated Flows, *J. Fluid Mech.* 24, 113–151.

Chakravarthy, S.R. & Osher, S. 1983 A New Class of High Accuracy TVD Schemes for Hyperbolic Conservation Laws, *AIAA*–98–0363.

Chang, S.H. 1990 On the Application of ENO Scheme with Subcell Resolution to Conservation Laws with Stiff Source Terms, *Computational Fluid Dynamics Symposium on Aeropropulsion*, NASA Lewis Research Center, 215–225.

Chang, S. –H. & Liou, M.–S. 1988 A Numerical Study of ENO and TVD Schemes for Shock Capturing, *NASA TM* 101355.

Chen, M.–H., Hsu, C.–C. & Shyy, W. 1991 Assessment of TVD Schemes for Inviscid and Turbulent Flow Computation, *Inter. J. Numer. Meth. Fluids* 12, 161–177.

Chen, Y.S. 1989 Compressible and Incompressible Flow Computations with a Pressure Based Method, *AIAA Paper* 89–0286.

Cheng, S. I. & Shubin, G. 1978 Computational Accuracy and Mesh Reynolds Number, *J. Comp. Phy.* 28, 315–326.

Chu, B.T. 1964 On the Energy Transfer to Small Disturbances in Fluid Flow (Part 1), *Acta Mech.* I/3, 215–234.

Colella, P. 1985 A Direct Euler MUSCL Scheme for gas Dynamics, *SIAM J. Sci. Stat. Comp.* 6, 104–117.

Colella, P. 1990 Multidimensional Upwind Methods for Hyperbolic Conservation Laws, *J. Comp. Phy.* 87, 171–200.

Correa, S. M. & Shyy, W. 1987 Computational Models and Methods for Continuous Gaseous Turbulent Combustion, *Progress in Energy and Combustion Sciences* 13, 249–292.

Davis, S.F. 1984 TVD Finite Difference Schemes and Artificial Viscosity, *ICASE Report* No. 84–20.

Davis, S.F. 1988 Simplified Second–Order Godunov–Type Methods, *SIAM J. Sci. Stat. Comp.* 9, 445–472.

Davis, D.L. 1992 Numerical Analysis of Techniques for Efficient Generation of Vorticity in Supersonic Flows, *AIAA Paper* No. 92–0828.

Eaton, J.K. & Johnston, J.P. 1980 Turbulent Flow Reattachment: An Experimental Study of the Flow and Structure Behind a Backward–Facing Step, *Technical Report* MD–39, Stanford University.

Engquist, B., Lötstedt, P. & Sjögreen 1989 Nonlinear Filters for Efficient Shock Computation, *Math. Comp.* 52, 509–537.

Fletcher, C. A. J. 1988 *Computational Techniques for Fluid Dynamics,* Vols I and II, Springer, New York.

Gartling, D.K. 1990 A Test Problem for Outflow Boundary Conditions – Flow Over a Backward Facing Step, *Int. J. Num. Meth. Fluids* 11, 953–967.

Ghia, U., Ghia, K.N. & Shin, C.T. 1982 High Re–Solutions for Incompressible Flow Using the Navier–Stokes Equations and a Multigrid Method, *J. Comp. Phy.* 48, 387–411.

Godunov, S.K. 1959 Finite Difference Methods for Numerical Computation of Discontinuous Solutions of the Equations of Fluid Dynamics, *Mat. Sbornik.*, 47, 271 [in Russian].

Goodman, J.B. and LeVeque, R.J. 1988 A Geometric Approach to High Resolution TVD Schemes, *SIAM J. Num. Anal.* 25, 268–284.

Gresho, P.M. and Lee, R.L. 1981 Don't Suppress the Wiggles–They are Telling You Something, *Comp. Fluids* 9, 223–253.

Harten, A. 1978 The Artificial Compression Method for Computation of Shocks and Discontinuities: III. Self–Adjusting Hybrid Schemes, *Math. Comp.* 32, 363–389.

Harten, A. 1983 High Resolution Schemes for Hyperbolic Conservation Laws, *J. Comp. Physics* 49, 357–393.

Harten, A. 1984 On a Class of High Resolution Total–Variation–Stable Finite–Difference Schemes, *SIAM J. Num. Anal.* 21, 1–23.

Harten, A. 1989 ENO Schemes with Subcell Resolution, *J. Comp. Physics* 83, 148–184.

Harten, A. & Hyman, J.M. 1983 Self Adjusting Grid Methods for One–Dimensional Hyperbolic Conservation Laws, *J. Comp. Phy.* 50, 235–269.

Harten, A. & Osher, S. 1987 Uniformly High–Order Accurate Nonoscillatory Schemes. I., *SIAM J. Num. Anal.* 24, 279–309.

Harten, A., Engquist, B., Osher, S. & Chakravarthy, S.R. 1987 Uniformly High–Order Accurate Essentially Non–Oscillatory Schemes. III. , *J. Comp. Phy.* 72, 231–303.

Han, T., Humphrey, J.A.C. & Launder, B.E. 1981 A Comparison of Hybrid and Quadratic–Upstream Differencing in High Reynolds Number Elliptic Flows, *Comp. Meth. Appl. Mech. Engg.* 29, 81–95.

Hayase, T., Humphrey, J.A.C. & Greif, R. 1992 A Consistently Formulated QUICK Scheme for Fast and Stable Convergence Using Finite–Volume Iterative Calculation Procedures, *J. Comp. Phy.* 98, 108–118.

Hinze, O. 1959 *Turbulence*, McGraw Hill, New York.

Hirsch, C. 1990 *Numerical Computation of Internal and External Flows,* Two Volumes, Wiley, New York.

Huang, P.G., Launder, B.E. & Leschziner, M.A. 1985 Discretization of Nonlinear Convection Processes: A Broad–Range Comparison of Four Schemes, *Comp. Meth. Appl. Mech. Engg.* 48, 1–24.

Issa, R.I. 1986 Solution of the Implicitly Discretized Fluid Flow Equations by Operator Splitting, *J. Comp. Phy.* 62, 40–65.

Jameson, A., Schmidt, W. & Turkel, E. 1981 Numerical Simulation of the Euler Equations by Finite Volume Methods Using Runge–Kutta Time Stepping Schemes, *AIAA Paper* No. 81–1259.

Jiang, Y., Chen, C.P. & Tucker, P.K. 1990 Multigrid Solution of Unsteady Navier–Stokes Equations Using a Pressure Method, *AIAA Paper* 90–1522.

Jones, W.P. & Launder, B.E. 1972 The Prediction of Laminarization with a Two–Equation Model of Turbulence, *Int. J. Heat Mass Trans.* 15, 301–314.

Jones, W.P. & Launder, B.E. 1973 Prediction of Low–Reynolds–Number Phenomenoa with a Two–Equation Model of Turbulence, *Int. J. Heat Mass Trans.* 16, 119.

Kamath, H. 1989 Parabolized Navier–Stokes Algorithm for Chemically Reacting Flows, *AIAA Paper* No. 89–0386.

Langhorne, P.J. 1985 Reheat Buzz: An Acoustically Coupled Combustion Instability. Part 1. Experiment, *J. Fluid Mech.* 193, 417–443.

Langhorne, P.J., Dowling, A.P. & Hooper, N. 1990 Practical Active Control System for Combustion Oscillations, *J. Propul. Power* 6, 324–333.

Launder, B.E & Spalding, D.B. 1972 *Mathematical Models of Turbulence*, Academic Press, London and New York.

Launder, B.E & Spalding, D.B. 1974 The Numerical Computation of Turbulent Flows, *Comp. Meth. Appl. Mech*, Eng. 3, 269–289.

Launder, B.E., Reece, G. & Rodi, W. 1973 Progress in the Development of a Reynolds–Stress Turbulence Closure, *J. Fluid Mech.* 68, 537–566.

Leonard, B.P. 1979 A Stable and Accurate Convective Modelling Procedure Based on Quadratic Upstream Interpolation, *Comp. Meth. Appl. Mech. Engg.* 19, 59–98.

Leonard, B.P. 1988a Elliptic Systems: Finite Difference Methods IV, in W.J. Minkowycz, E.M. Sparrow, G.E. Schneider & R.H. Pletcher (eds.), *Handbook of Numerical Heat Transfer*, Wiley, New York, 347–378.

Leonard, B.P. 1988b Simple High–Accuracy Resolution Program for Convective Modelling of Discontinuities, *Int. J. Num. Meth. Fluids* 8, 1291–1318.

LeVeque, R.J. 1990 *Numerical Methods for Conservation Laws*, Birkhäuser Verlag, Basel, Germany.

LeVeque, R.J. & Yee, H.C. 1990 A Study of Numerical Methods for Hyperbolic Conservation Laws with Stiff Source Terms, *J. Comp. Phy.* 86, 187–210.

Liou, M.S. 1987 A Generalized Procedure for Constructing an Upwind–Based TVD Scheme, *AIAA*–87–0355.

Lumley, J.L. 1978 Computational Modeling of Turbulent Flows, in C.S. Yih (ed.), *Advances in Applied Mechanics* 18, Academic Press, New York, 123.

MacCormack, R.W. & Baldwin, B.S. 1975 A Numerical Method for Solving the Navier–Stokes Equations with Application to Shock–Boundary Layer Interactions, *AIAA Paper* No. 75–1.

Mansour, M.L. & Hamed, A. 1990 Implicit Solution of the Incompressible Navier–Stokes Equation on a Non–Staggered Grid, *J. Comp. Phy.* 86, 147–167.

Menon, S. 1991 Active Control of Combustion Instability in a Ramjet Using Large–Eddy Simulation, *AIAA*–91–0411.

Merkle, C.L. & Choi, Y.–H. 1987 Computation of Low Speed Flow with Heat Addition, *AIAA J.* 25, 831–838.

Mittal, R. 1991 Control of Longituidinal Oscillations in a Constant Area Combustor: Numerical Simulation, Masters Thesis, University of Florida.

Moffatt, H. K. 1964 Viscous and Resistive Eddies Near a Sharp Corner, *J. Fluid Mech.* 18, 1–18.

Moretti, G. 1987 Computation of Flows with Shocks, *Ann. Rev. Fluid Mech.* 19, pp 313–337.

Nessyahu, H. & Tadmor, E. 1990 Non–Oscillatory Central Differencing for Hyperbolic Conservation Laws, *J. Comp. Phy.* 87, 408–463.

Ni, R.H. 1982 A Multiple Grid Scheme for Solving Euler Equations, *AIAA J.* 20, 1565–1571.

Patankar, S.V. 1980 *Numerical Heat Transfer and Fluid Flow*, Hemisphere, Washington DC.

Patankar, S.V. 1988 Recent Developments in Computational Heat Transfer, *ASME J. Heat Transf.* 110, 1037–1045.

Patankar, S.V. & Spalding, D.B. 1972 A Calculation Procedure for Heat, Mass and Momentum Transfer in Three–Dimensional Parabolic Flows, *Int. J. Heat Mass Trans.* 15, 1787–1806.

Patel, V.C, Rodi, W. & Scheuerer, G. 1985 Turbulence Models for Near–Wall and Low Reynolds Number Flows, *AIAA J.* 23, 1308–1319.

Przekwas, A.J. & Yang, H.Q. 1989 Advanced CFD Methodology for Fast Transients Encountered in Nonlinear Combustion Instability Problems, *CFD Research Corporation Report* 4065/1, Huntsville, AL.

Priddin, C.H. & Coupland, J. 1986 Impact of Numerical Methods on Gas Turbine Combustor Design and Development, in *Calculations of Turbulent Reactive Flows*, R.M.C. So, J.H. Whitelaw & H.C. Mongia (eds.), ASME, New York, 335–348.

Rayleigh, J.W.S. 1945 *The Theory of Sound*, Vol. 2, Dover Publications, New York.

Rhie, C.M. 1986 A Pressure Based Navier Stokes Solver Using the Multigrid Method, *AIAA Paper* No. 86–0207.

Roache, P.J. 1972 *Computational Fluid Dynamics*, Hermosa Publishers, Albuquerque, NM.

Roe, P.L. 1981 Approximate Riemann Solvers, Parameter Vectors, and Difference Schemes, *J. Comp. Phy.* 43, 321–351.

Roe, P.L. 1985 Some Contribution to the Modelling of Discontinuous Flows, in E. Engquist et al. (eds.), *Large Scale Computations in Fluid Mechanics, Part 2 (Lectures in Applied Mathematics 22)*, American Mathematical Society, 183.

Roe, P.L. 1986 Characteristic–Based Schemes for the Euler Equations, *Ann. Rev. Fluid Mech.*, 337–356.

Schreiber, R., & Keller, H.B. 1983 Driven Cavity Flows by Efficient Numerical Techniques, *J. Comp. Phy.* 49, 310–333.

Shuen, J.–S., Chen, K.–H. & Choi, T. 1992 A Time–Accurate Algorithm for Chemical Non–Equilibrium Viscous Flows at All Speeds, *AIAA Paper* No. 92–3639.

Shyy, W. 1984 A Note on Assessing Finite Difference Procedures for Large Peclet/Reynolds Number Flow Calculation, in J.J.H. Mileer (ed.), *Boundary and Interior Layers: Computational and Asymptotic Methods* 3, Boole Press, Dublin, Ireland, 303–308.

Shyy, W. 1985a A Study of Finite Difference Approximations to Steady–State, Convection Dominated Flow Problems, *J. Comp. Phy.* 57, 415–437.

Shyy, W. 1985b A Numerical Study of Annular Dump Diffuser Flows, *Comp. Meth. Appl. Mech. Eng.* 53, 47–65.

Shyy, W. 1988 A Numerical Study of Two–Dimensional Compressible Navier–Stokes Flows, *Num. Heat Transfer* 14, 323–341.

Shyy, W. 1989 A Unified Pressure Correction Algorithm for Computing Complex Fluid Flows, *Recent Advances in Computational Fluid Mechanics* 43, C.C. Chao, S.A. Orzag & W. Shyy (eds.), Lecture Notes in Engineering, Springer–Verlag, New York, 135–147.

Shyy, W. 1993 Applications of Body–Fitted Coordinates in Transport Phenomena: Numerical Computation and Physical Interpretation, in *Advances in Transport Phenomena* 9, A.S. Mujumdar & R.A. Mashelkar (eds.), Elsevier, Amsterdam, The Netherlands, to appear.

Shyy, W. & Braaten, M.E. 1988 Adaptive Grid Computation for Inviscid Compressible Flows Using a Pressure Correction Method, *Proceedings of the AIAA/ASME/SIAM/APS First National Fluid Dynamics Congress*, AIAA–CP 888, 112–120.

Shyy, W., Braaten, M.E. & Burrus, D.L. 1989 Study of Three–Dimensional Gas–Turbine Combustor Flows, *Inter. J. Heat Mass Transf.* 32, 1155–1164.

Shyy, W., Chen. M.–H. & Sun, C.–S. 1992b Pressure–Based Multigrid Algorithm for Flow at All Speeds, *AIAA J.* 30, 2660–2669.

Shyy, W., Correa, S.M. & Braaten, M.E., 1986 Computational Models for Gas–Turbine Combustors, in *Calculations of Turbulent Reactive Flows*, R.M.C. So, J.H. Whitelaw & H.C. Mongia (eds.), ASME, New York, 141–184.

Shyy, W., Mittal, R. & Udaykumar, H.S. 1992a Control of Longitudinal Oscillations in a Constant Area Combustor: Numerical Simulation, *Combust. Flame* 89, 363–366.

Shyy, W. & Sun, C.–S. 1993 Development of a Pressure–Correction/Staggered Grid Based Multigrid Solver for Incompressible Recirculating Flows, *Comp. Fluids* 22, 51–76.

Shyy, W. & Udaykumar, H.S. 1990 Numerical Simulation of Thermo–Acoustic Effect of Longitudinal Combustion Instabilities, *AIAA Paper* No. 90–2065.

Shyy, W., Wright, J.A. & Liu, J. 1993 A Multilevel Composite Grid Method for Fluid Flow Computations, *AIAA Paper* No. 93–0768.

Sod, G.A. 1983 *Numerical Methods in Fluid Dynamics: Initial and Initial Boundary–Value Problems*, Cambridge University Press, Cambridge, United Kingdom.

Speziale, C.G & Thangam, S. 1992 Analysis of an RNG Based Turbulence Model for Separated Flows, *Int. J. Engng. Sci.* 30, 1379–1388.

Strang, G. 1968 On the Construction and Comparison of Difference Schemes, *SIAM J. Num. Anal.* 5, 506–517.

Sturgess, G.J. 1986 Calculation of Aerospace Propulsion Combustors: A View from Industry, in *Calculations of Turbulent Reactive Flows*, R.M.C. So, J.H. Whitelaw and H.C. Mongia (eds.), ASME, New York, 185–232.

Sweby, P.K. 1984 High Resolution Schemes Using Flux Limiters for Hyperbolic Conservation Laws, *SIAM J. Num. Anal.* 21, 994–1011.

Sweby, P.K. & Baines, M.J. 1984 On Convergence of Roe's Scheme for the General Non–Linear Scheme Scalar Wave Equation, *J. Comp. Phy.* 56, 135–148.

Thomas, J.L., Van Leer, B., & Walters, R.W. 1985 Implicit Flux–Split Schemes for the Euler Equations, *AIAA Paper* No. 85–1680.

Van Leer, B. 1974 Towards the Ultimate Conservative Difference Scheme. II. Monotonicity and Conservation Combined in a Second–Order Scheme, *J. Comp. Phy.* 14, 361–370.

Van Leer, B. 1979 Towards the Ultimate Conservative Difference Scheme. V. A Second–Order Sequel to Godunov's Method, *J. Comp. Phy.* 32, 101–136.

Vanka, S.P. 1985 Block Implicit Calculation of Steady Turbulent Recirculating Flows, *Intl. J. Heat Mass Transf.* 28, 2093–2103.

Vanka, S.P. 1986 Block–Implicit Multigrid Solution of Navier–Stokes Equations in Primitive Variables, *J. Comp. Phy.* 65, 138–158.

Vanka, S.P. 1987 Second–Order Upwind Differencing in a Recirculating Flow, *AIAA J.* 25, 1435–1441.

Viegas, J.R., Rubesin, M.W. & Horstman, C.C. 1985 On the Use of Wall Functions as Boundary Conditions for Two–Dimensional Separated Compressible Fows, *AIAA Paper* 85–0180.

Vu, T. C. & Shyy, W. 1990 Navier–Stokes Flow Analysis for Hydraulic Turbine Draft Tube, *J. Fluids Eng.* 12, 199–204.

Wang, J.C.T. & Widhopf, G.F. 1989 A High–Resolution TVD Finite Volume Scheme for the Euler Equations in Conservation Form, *J. Comp. Phy.* 84, 145–173.

Warming, R.F. & Beam, R.M. 1976 Upwind Second–Order Difference schemes and Applications in Aerodynamic Flows, *AIAA J.* 14, 1241–1249

Warming, R.F., Kutler, P. & Lomax, H. 1973 Second– and Third–Order Noncentral Difference Schemes for Nonlinear Hyperbolic Equations, *AIAA J.* 11, 189–196.

Wilson, K.J., Gutmark, E., Schadow K.C. & Smith, R.A. 1991 Active Control of a Dump Combustor with Fuel Modelation, *AIAA Paper* 91–0368.

Withington, J.P., Shuen, J.S. & Yang, V. 1991 A Time Accurate, Implicit Method for Chemically Reacting Flows at All Mach Numbers, *AIAA Paper* 91–0581.

Woodward, P. & Colella, P. 1984 The Numerical Simulation of Two–Dimensional Fluid Flow with Strong Shocks, *J. Comp. Phy.* 54, 115–173.

Wright, J. & Shyy, W. 1992 A Pressure–Based Composite Grid Method for the Incompressible Navier–Stokes Equations, *AIAA Paper* No. 92–3641, also to appear in J. Comput. Physics.

Yakhot, V. & Orszag, S.A. 1986 Renormalization Group Analysis of Turbulence. I. Basic Theory, *J. Sci. Comput.* 1, 3–51.

Yee, H.C. 1985 On Symmetric and Upwind TVD Schemes, *NASA TM* 86842.

Yee, H.C. 1986 Linearized Form of Implicit TVD Schemes for the Multidimensional Euler and Navier–Stokes Equations, *Comp. & Math. with Appls.* 12A, 413–432.

Yee, H.C. 1987a Construction of Explicit and Implicit Symmetric TVD Schemes and Their Applications, *J. Comp. Phy.* 68, 151–179.

Yee, H.C. 1987b Upwind and Symmetric Shock–Capturing Schemes, *NASA TM* 89464.

Yee, H.C. & Harten, A. 1987 Implicit TVD Schemes for Hyperbolic Conservation Laws in Curvilinear Coordinates, *AIAA J.* 25, 266–274.

Yee, H.C., Klopfer, G.H. & Montagne, J.–L. 1990 High–Resolution Shock–Capturing Schemes for Inviscid and Viscous Hypersonic Flows, *J. Comp. Phy.* 88, 31–61.

Yee, H.C., Warming, R.F. and Harten, A. 1985 Implicit Total Variation Diminishing (TVD) Schemes for Steady–State Calculations, *J. Comp. Phy.* 57, 327–360.

Zalesak, S.T. 1979 Fully Multidimensional Flux–Corrected Transport Algorithms for Fluids, *J. Comp. Phy.* 31, 335–362.

BIOGRAPHICAL SKETCH

Siddharth Singh Thakur was born in May, 1966, in India. He earned his bachelor's degree in aeronautical engineering from the Indian Institute of Technology, Bombay, India, in 1987 and his master's degree in aerospace engineering from the University of Florida in 1989. Since fall 1989, he has been pursuing a Ph.D degree in aerospace engineering with specialization in computational fluid dynamics.

I certify that I have read this study and that in my opinion it conforms to acceptable standards of scholarly presentation and is fully adequate, in scope and quality, as a dissertation for the degree of Doctor of Philosophy.

Wei Shyy, Chairperson
Professor of Aerospace Engineering,
Mechanics and Engineering Science

I certify that I have read this study and that in my opinion it conforms to acceptable standards of scholarly presentation and is fully adequate, in scope and quality, as a dissertation for the degree of Doctor of Philosophy.

Richard L. Fearn
Professor of Aerospace Engineering,
Mechanics and Engineering Science

I certify that I have read this study and that in my opinion it conforms to acceptable standards of scholarly presentation and is fully adequate, in scope and quality, as a dissertation for the degree of Doctor of Philosophy.

Chen–Chi Hsu
Professor of Aerospace Engineering,
Mechanics and Engineering Science

I certify that I have read this study and that in my opinion it conforms to acceptable standards of scholarly presentation and is fully adequate, in scope and quality, as a dissertation for the degree of Doctor of Philosophy.

David Mikolaitis
Associate Professor of Aerospace Engineering, Mechanics and Engineering Science

I certify that I have read this study and that in my opinion it conforms to acceptable standards of scholarly presentation and is fully adequate, in scope and quality, as a dissertation for the degree of Doctor of Philosophy.

William W. Hager
Professor of Mathematics

This dissertation was submitted to the Graduate Faculty of the College of Engineering and to the Graduate School and was accepted as partial fulfillment of the requirements for the degree of Doctor of Philosophy.

August 1993

for

Winfred M. Phillips
Dean, College of Engineering

Madelyn M. Lockhart
Dean, Graduate School